Model for the dynamics of liquid penetration into porous structures and its detection with the help of changes in ultrasonic attenuation

Dem Fachbereich für Maschinenbau
an der Technischen Universität Darmstadt
zur
Erlangung des Grades eines Doktor-Ingenieurs (Dr.-Ing.)
genehmigte

Dissertation

vorgelegt von

Dipl.-Ing. Matias Daun

aus Solingen

Berichterstatter	Prof. Dr.-Ing. Manfred J. Hampe
Mitberichterstatter	Prof. Dr.-Ing. Samuel Schabel
Tag der Einreichung	10.11.2005
Tag der mündlichen Prüfung	10.01.2006

Darmstadt 2006
D17

Acknowledgements

I want to thank
Professor Dr Manfred Hampe, Professor Dr Samuel Schabel, Dr Len Gate, Dr Graham O'Neill, Mikko Likitalo, Chris Nutbeem, Dr Graham Pring, Dr Marielle Lorusso, Dr Janet Preston, Dr Tony Hiorns, Dr John Husband, the Par Moor Laboratory Team, Giselher Grüner, Ellen Das, Karl Ofner, Dr Miklós Kanzamár Lidia Querling, Daniela Geisbüsch, Clemens Elliger, Oliver Heller, Jörn Buhn, Susanne Wolf, Dr Herbert Klan, Hildegard and Berthold Daun, and Dorothee Hofer
for discussions, support and criticism.

This thesis would not have been possible without the special support of IMERYS Minerals Ltd.

Eidesstattliche Erklärung

Hiermit erkläre ich, daß ich die vorliegende Arbeit selbständig verfaßt und keine fremden Hilfsmittel außer den genannten verwendet habe. Ich habe bisher noch keinen Promotionsversuch unternommen.

Solingen, im November 2005

Lebenslauf

Name:	Matias Daun
Geburtsdatum:	26.04.1971
Geburtsort:	Solingen
Familienstand:	verheiratet

1977-1981	Grundschule Stübchen, Solingen
1981-1987	Realschule Vogelsang, Solingen
1987-1990	August-Dicke-Gymnasium, Solingen Abschluß: Allgemeine Hochschulreife
1990-1991	Zivildienst
1990-1991	Fernstudium an der Fernuni Hagen, Deutschland
1991-1997	Studium an der Universität Dortmund, Deutschland, Fachbereich Chemietechnik Abschluß Diplom
1997-1998	Stora Kabel, Deutschland
1998-2004	ECCI / Imerys Minerals Ltd, England
seit 2004	Norske Skog Walsum

Contents

Symbols

Greek Symbols

Symbol	Unit	Description
α	Np/m	general attenuation coefficient
α_{Mutec}		pseudo-attenuation coefficient given by the *Mutec Penetration Dynamics Analyser*
α_s	Np/m	attenuation coefficient due to scattering for a regime of bubbles
α_v	Np/m	attenuation coefficient for viscous loss
β	1/s	constant containing losses
Δp	Pa	pressure change in a piezoelectric material
ΔSPL		drop in sound pressure level
Δx	m	thickness change of a piezoelectric material
ζ		substitution variable
η	Pa s	viscosity
γ	J/m^2	surface energy of a specimen
γ	N/m	surface tension of a liquid
θ	rad	angle
θ_i	rad	angle of incidence
θ_t	rad	transmitted angle
Θ	°	contact angle of a liquid at a liquid-solid-air interface
κ	−	adiabatic compressibility of a gas
λ	m	wave length
λ_1	m	wave length in medium 1
λ_2	m	wave length in medium 2
ρ	kg/m^3	density
ρ_l	kg/m^3	density of a liquid
ρ_m	kg/m^3	density of a medium
ρ_s	kg/m^3	density of a solid sphere
σ_e	m^2	extinction cross-section
σ_s	m^2	scattering cross-section
ξ_0	m	initial displacement of an interface

ξ	m	displacement of a particle or an interface i.e. of a bubble
Ξ_1		constant
Ξ_2		constant
$\dot{\xi}$	m/s	velocity of a particle or an interface i.e. of a bubble
$\ddot{\xi}$	m/s^2	acceleration of a particle or an interface i.e. of a bubble
ϕ	rad	angular component of a cylindrical coordinate system
ϕ_o	rad	angular component of a vector describing the position of an observer
ϕ_s	rad	angular component of a vector describing the position on the surface of the Sender
ϕ_s	rad	angular component of a cylindrical coordinate system
ω	rad/s	angular frequency of ultrasound

Latin Symbols

Symbol	Unit	Description
A		amplitude of a wave
A_0		initial amplitude of a wave
b	kg/s	dampening constant
c	m/s	speed of sound
c_∞	mol/m^3	concentration of component i at equilibrium
c_0	mol/m^3	concentration of component i at the interface at time zero
c_1	m/s	speed of sound in medium 1
c_2	m/s	speed of sound in medium 2
c_i	mol/m^3	concentration of component i
C_P	J/mol	heat capacity of a gas at constant volume
C_V	J/mol	heat capacity of a gas at constant pressure
d	m	distance
d_{33}	m/V	piezoelectric modulus
d_r	kg/s	radiation resistance
d_v	kg/s	resistance due to viscous friction
d_b	kg/s	resistance due to losses in the boundary layer
D	m	diameter of a transducer
D_i	m^2/s	diffusion coefficient for component i
D_s	W	scattered acoustic power
E	N/m^2	elasticity modulus
f	Hz	frequency of ultrasound

f_r	Hz	resonance frequency
$f_{\text{r, micro-bubble}}$	Hz	resonance frequency of a micro-bubble
g_{33}	Vm/Pa	piezoelectric pressure constant
G	N/m^2	shear modulus
h	m	capillary rise or liquid penetration into a capillary
h'	m	liquid penetration depth into a capillary in the prime coordinate system
h''	m	liquid penetration depth into a capillary in the double prime coordinate system
h_{33}	V/m	piezoelectric deformation constant
h_0	m	depth of the gas volume in a capillary
h_ξ	m	substitution variable
h_{Receiver}	m	thickness of a piezoelectric Receiver
h_{Sender}	m	thickness of a piezoelectric Sender
H	m	capillary length
He_i	Pa	Henry constant for component i
$\imath$		imaginary number
i		index
I	W/m^2	intensity
I_0	W/m^2	intensity of incident beam
I_s	W/m^2	scattered intensity
j_i	mol/m^2/s	mole flux of component i
J_1		first order Bessel function
k	1/m	wave number of ultrasound
k	N/m	spring constant
k_{33}		piezoelectric coupling constant
K_m		Compressibility of a medium
K_s		Compressibility of a solid sphere
l	m	boundary layer thickness
m	kg	mass
M	kg/mol	specific molar mass
n	mol	number of molecules
$\dot{n}$	mol/s	mole flux through a certain cross-sectional area
n_{bubbles}		number of bubbles
N	m	near-field distance
$\hat{p}$	Pa	maximum acoustic pressure of a sound wave
p	Pa	acoustic pressure

p_i	Pa	partial pressure of component i
P	Pa	ambient pressure
P_h	Pa	hydrostatic pressure
P_{ho}	Pa	pressure in a sealed capillary
P_o	Pa	ambient pressure
P_L	Pa	pressure due to a curved interface
r_o	m	radial component of a vector describing the position of an observer
r_s	m	radial component of a vector describing a position on the surface of the Sender
$\vec{r}$		vector describing the distance between a circular source and an observer
R	m	radius of a capillary, pore or particle
$R_{\xi,\,1/2}$	–	reflection coefficient for acoustic pressure at the phase boundary between medium 1 and 2
R_g	J/K/mol	gas constant
R_I	–	reflection coefficient for acoustic intensity
R_P	–	reflection coefficient for acoustic pressure
$R_{\mathrm{P,\,T/M}}$	–	reflection coefficient for acoustic pressure for a reflection at the phase boundary between a transducer T and a medium M
R_v	–	reflection coefficient for acoustic velocity
$R_{z,i}$	kg/m^2/s	resistive component of the acoustic impedance of medium i
Re		Reynolds number
S	m^2	surface of a transducer or a scatterer
S_P		shell elasticity factor
t	s	time
$t_{\max}$	s	time when a function reaches its maximum
T	K	temperature
$T_{\dot{\xi},\,1/2}$	–	transmission coefficient for acoustic pressure for a transmission across the phase boundary between medium 1 and 2
$T_{\mathrm{P,\,M/T}}$		transmission coefficient for acoustic pressure for transmission across the phase boundary between a medium M and a transducer T
$T_{\mathrm{P,\,T/M}}$		transmission coefficient for acoustic pressure for transmission across the phase boundary between a transducer T and a medium M
U_{Sender}	V	voltage applied in the Sender
U_{Receiver}	V	voltage generated in the Receiver

v	m/s	velocity
$v_{\max}$	m/s	maximum velocity of a vibrating surface
V	m^3	volume
V_l	m^3	volume occupied by liquid
V_h	m^3	volume of a capillary with length h
V_{h_0}	m^3	volume of a capillary with length h_0
W	W	power loss
x_i	mol/mol	mole fraction of component i
$X_{z,i}$	$kg/m^2/s$	reactive component of the acoustic impedance of medium i
z_o	m	axial component of a vector describing the position of an observer
z_s	m	axial component of a vector describing a position on the surface of the Sender
Z_i	$kg/m^2/s$	specific acoustic impedance of a medium i

1 Introduction

Paper is a material usually composed of natural fibres. Depending on the paper grade different amounts of filler and chemical additives are used. Paper is a porous material where the pore structure in most paper grades is a continuous three-dimensional network of voids. In the same manner the solid material, fibres and fillers, also form a continuous three-dimensional network. [38]

Today, a large variety of paper grades exists: woodfree, wood containing, rag containing, uncoated, single-side and two-side coated grades are available. The paper production process remains still the process developed by the chinese but with highly efficient and automated paper machines. A suspension of fibres at about 1% consistency is evenly distributed over a sieve and then dewatered by gravity and vacuum to a consistency of about 20% forming a paper web. The moister is further removed by a pressing section reaching a moisture level of about 50%. The remaining water is then removed by the means of thermal energy and the final paper reaches a moisture level of 10-5% before being reeled up.[35]

Depending on the paper grade, a coating process can be added during the paper production. During the coating process an aqueous blend of pigments, binder and additives is applied onto the surface. The coating is then metered off and dried.

In **Figure 1.1** an example of a single-side coated paper sample is shown. The fibres in this picture are white and form a network. The voids formed by the network are filled with air.

In most of the coating processes an excess of coating colour is applied onto the base-paper and then metered off. Modern paper machines have production speeds of up to 2000 m/min. Depending on the coating aggregate the distance between application of the coating colour and the metering can be up to 1 m. The time between application and metering is then of the order of 0.03 s. During this period the liquid phase can penetrate into the base-paper. The liquid can interact with the fibres and this has implications for the strength and roughness of the paper.

Printing is a second big area where liquid-paper-interactions are important. Almost all of today's printing techniques are based on interactions between

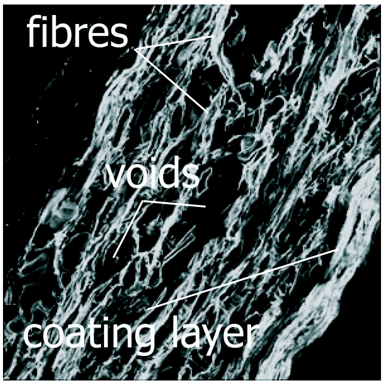

Figure 1.1: Picture of a cross-section of a board sample [39].

liquid and solid materials. Elftonson and Ström [10] define and categorize different mechanisms for the interaction between liquid and solid materials. The interactions may be divided into

- wetting, i.e. the contact of liquid with a solid surface,
- spreading, which refers to transport of liquid on a surface, and
- penetration or absorption, which occurs when a liquid is transported into a porous structure.

These processes are either spontaneous or forced. In certain printing nips, as the letterpress or the lithographic offset printing, the ink is forced to wet the solid and penetrate into its pore structure, while in others, for example gravure, liquid is sucked into the paper by capillary pressure. During inkjet printing ink droplets are first forced to penetrate the paper but spontaneous absorption soon becomes the major driving force. Offset printing involves a number of fairly complicated liquid-solid-interactions. In this process films of emulsions and fountain-solutions are transferred between different surfaces before the ink is forced into the paper structure. Not only the ink but also the fountain-solution wets the paper. The film of the fountain-solution remaining on the paper when it exits the printing nip may cause problems such as ink refusal and mottling in multicolor printing.

Preston et al. [34] investigate how the absorption of the ink vehicle into the coating layer influences print gloss and print evenness. Current models describing liquid penetration into paper are based on the Lucas-Washburn-Equation. Accordingly Preston [33] develops a model for paper as a series of capillaries of different sizes. She finds that the size of surface pores as well as the number of pores play an important role in print-gloss and print-density during the setting of offset inks.

Penetration into capillaries can be described using the Lucas-Washburn-Equation [23, 41] which in a gravity-free situation is obtained by balancing the liquid's viscous friction with the capillary suction. The velocity of change in capillary rise is a function of the height h of capillary rise, the surface tension γ of the liquid, the contact angle θ with the material of the capillary, the viscosity η of the liquid and the hydrostatic pressure P_h and is given below in Equation (1.1)

$$\frac{dh}{dt} = \frac{2 \cdot \gamma \cdot \cos \Theta \cdot R + P_h \cdot R^2}{8 \cdot \eta \cdot h(t)} \qquad (1.1).$$

Matthews [24] develops the Por-Cor computer model to calculate fluid permeation in porous structures. In the Por-Cor model the porous material is modelled by capillaries of varying diameters which intersect in cubic voids. The dynamic liquid penetration into this network is described by the Bosanquet-Equation:

$$\frac{8 \cdot \eta \cdot h(t)}{R^2} \frac{dh}{dt} + \rho \cdot \frac{d}{dt} \left(h(t) \cdot \frac{dh}{dt} \right) = \frac{2 \cdot \gamma \cos(\Theta)}{R} + P_h \qquad (1.2).$$

This equation was first developed by Bosanquet [5] and takes into account the change in inertial energy when a liquid penetrates into a capillary. The capillary suction is opposed by the change in inertial energy and a pressure loss due to viscous friction as given by the Hagen-Poiseuille-Law. The density ρ of the liquid is needed in addition to the variables introduced above. All these models assume that the influence of air can be neglected in the penetration process. However according to Baird and Irubesky [2] only 1.6 % of the pores in paper are in contact with both sides of the paper surface. This poses the question of what happens to the air when liquid penetrates into the surface of the paper sheet. Salminen [37] suggests that a part of the air will be compressed and another part will be expelled perpendicularly to the liquid penetrating into pores.

To verify the theory methods of measuring liquid penetration into a substrate are needed. Only very few of the current measurement devices can measure water penetration over short periods. Two of these measurements are the Drop-Absorption-Test and the Bristow-Test. The Drop-Absorption-Test records pictures of a drop whilst it is being placed onto a substrate. With image analysis techniques the base of the drop as well as its height is recorded as a function of the time. With these values the absorption rate of the liquid into the substrate can be calculated. It allows quite an efficient time resolution but changes in the paper's surface due to fibre swelling reduce its suitability. The Bristow-Test is specified in an American Standard Test Method [1]. A certain volume of liquid is brought into contact with a paper surface through a slit whilst the slit is moving at a constant speed. The length of the wet area is measured and evaluated. A fairly good time resolution is achieved but the roughness of the paper as well as its surface chemistry influence the result.

A quite recent device is the *Mutec Penetration Dynamics Analyser*. An Ultrasonic Attenuation Measurement is used to characterize liquid penetration into a porous substrate. To be precise, the *Mutec Penetration Dynamics Analyser* measures the attenuation of ultrasound due to air entrained in the paper when a liquid penetrates into the paper sheet, and it is consequently an indirect measurement for the liquid penetration. For the measurement a specimen is brought into contact with water and the attenuation of ultrasound passing through the sample is measured. As the liquid penetrates into the specimen air enclosures are formed which scatter the ultrasound. In the *Mutec Penetration Dynamics Analyser* the attenuation of ultrasound as a function of time is recorded. The first measurement is available after $8 \cdot 10^{-3}$ s.

It has to be pointed out here that there are alternative measurement devices basing on the same principle available on the market as eg the *emcoDPM* [3].

In this thesis an attempt is made to find a theory allowing to interpret and predict results of measurements obtained with the *Mutec Penetration Dynamics Analyser*.

2 State of the science

2.1 Ultrasound

Sound which can be heard by the human ear has frequencies from about 16 Hz to 20 kHz. Ultrasound cannot be heard by the human ear and starts at about 20 kHz and goes up to 10 GHz. The *Mutec Penetration Dynamics Analyser*, which is a subject of this thesis, uses ultrasound with a frequency of either 1 MHz or 2 MHz.

In general the use of ultrasound can be divided into high and low intensity applications. In low intensity applications the properties of the medium through which the sound is propagated are unchanged as amplitudes are small. These applications are used for non-destructive testing. In the case of high intensity ultrasound, changes in material properties can occur [11]. The *Mutec Penetration Dynamics Analyser* uses ultrasound with a maximum intensity of 10 $\mathrm{W/m^2}$. Under certain circumstances, as discussed in section 3.1.4 on page 49, the *Mutec Penetration Dynamics Analyser* can be regarded as a low intensity application.

Ultrasound propagates through media by compressional waves, transverse waves or surface waves. A compressional wave is also called longitudinal and is shown in **Figure 2.1**; the transverse wave is also known as shear wave and is shown in **Figure 2.2**. Longitudinal waves propagate through successive compressions and expansions along the direction of the propagation of the wave. In liquids and gases energy is manly transported by longitudinal waves. Transverse waves are only transmitted over very short distances in the order of micrometres. Shear waves transmit ultrasound through a displacement of particles orthogonally to the direction of the propagation of the wave. In solids all three forms of ultrasonic waves are observed.

A plane ultrasound wave can be described using the following equation of motion

$$\frac{\partial^2 \xi}{\partial t^2} - \left(\frac{\omega}{k}\right)^2 \frac{\partial^2 \xi}{\partial x^2} = 0 \tag{2.1}$$

with the time t, the distance x, the particle displacement ξ, the angular frequency $\omega = 2 \cdot \pi \cdot f$ with the frequency f, the wave number $k = \omega/c - \imath \cdot \alpha$ with the speed of sound c and the imaginary number $\imath = \sqrt{-1}$, and the

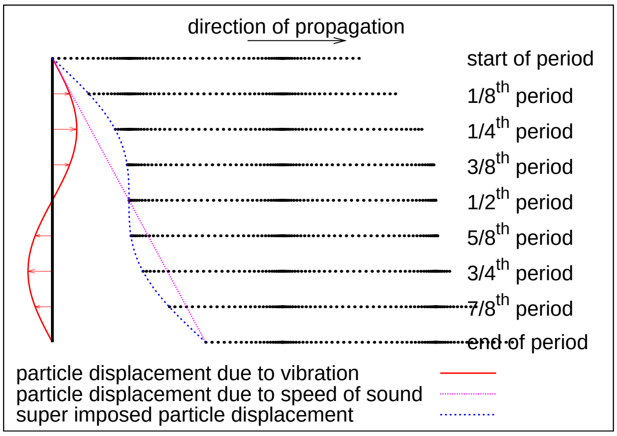

Figure 2.1: A longitudinal or compressional wave is transmitted through successive compressions and expansions in the direction of the spread of the wave. Sound is an example for a longitudinal wave. Areas of high and low pressure are indicated by the density of the dots.

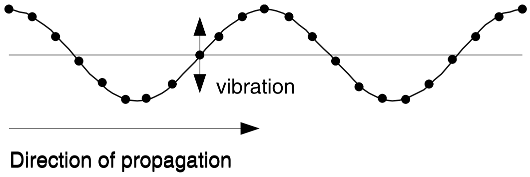

Figure 2.2: Transverse or shear waves are transmitted through displacement of particles orthogonally to the direction of spread. This is possible in an elastic medium. Hence transversal waves mainly occur in solid media and not in fluids. A vibrating string or light are examples of a transverse wave.

attenuation coefficient α. For a sinusoidal wave a solution to this equation is:

$$\xi = \xi_0 \cdot e^{\imath \cdot (\omega \cdot t - k \cdot x)}, \tag{2.2}$$

where ξ_0 is the initial amplitude of the particle displacement. The connection between the properties of the ultrasonic wave and the material through which it is propagated is given in textbooks e.g. Blitz [4]:

$$\frac{\partial^2 \xi}{\partial t^2} = \left(\frac{E}{\rho}\right)^2 \frac{\partial^2 \xi}{\partial x^2} \tag{2.3}$$

with the elasticity modulus E and the material density ρ. Combining Equations (2.1) and (2.3) leads to an equation which connects properties of the wave with properties of the medium it is propagating through [4]:

$$\left(\frac{\omega}{k}\right)^2 = \frac{E}{\rho} \qquad (2.4).$$

In highly attenuating materials the particle velocity and particle displacement are out of phase. The elasticity modulus and density are then complex and frequency dependant as is the wave number in Equation (2.1). But for many materials the attenuation coefficient is small ($\alpha \ll \omega/c$) and the velocity and the attenuation are in phase. Equation (2.4) can then be written as

$$c^2 = \frac{E}{\rho} \qquad (2.5).$$

For liquids and gases which transport shear-forces only over very short distances the main wave form is the longitudinal wave. Then the elasticity modulus E is equal to the bulk modulus $K = 1/\kappa$ with κ being the adiabatic compression. When a transverse wave is transmitted in a bulk solid the elasticity modulus is different because shear forces also operate. For bulk solids it becomes $E = K + 4 \cdot G/3$, with the shear modulus G.

The different properties of the sound-field, displacement ξ, velocity $\dot{\xi}$, acceleration $\ddot{\xi}$ and acoustic pressure p can be converted into each other using the angular frequency ω of the sound-field and the material properties speed of sound c and density ρ. This is given in Table 2.1 The intensity I of a sound-field can be expressed as a function of the acoustic pressure or the acoustic velocity:

$$I = \frac{\dot{\xi}_0^2}{2} \cdot \rho \cdot c = \frac{p_0^2}{2} \cdot \frac{1}{\rho \cdot c} \tag{2.6}$$

2.1.1 Generating and detecting ultrasound with a piezoelectric ceramic

The transducer in the *Mutec Penetration Dynamics Analyser* is made from a piezoelectric ceramic. A piezoelectric ceramic converts an applied voltage

	ξ_0	$\dot{\xi}_0$	$\ddot{\xi}_0$	p_0
ξ_0	ξ_0	$\frac{\dot{\xi}_0}{\omega}$	$\frac{\ddot{\xi}_0}{\omega^2}$	$\frac{p_0}{\omega\cdot\rho\cdot c}$
$\dot{\xi}_0$	$\omega\cdot\xi_0$	$\dot{\xi}_0$	$\frac{\ddot{\xi}_0}{\omega}$	$\frac{p_0}{\rho\cdot c}$
$\ddot{\xi}_0$	$\omega^2\cdot\xi_0$	$\omega\cdot\dot{\xi}_0$	$\ddot{\xi}_0$	$\frac{\omega\cdot p_0}{\rho\cdot c}$
p_0	$\rho\cdot c\cdot\omega\cdot\xi_0$	$\rho\cdot c\cdot\dot{\xi}_0$	$\frac{\rho\cdot c\cdot\ddot{\xi}_0}{\omega}$	p_0

Table 2.1: Conversion of different properties of a sound-field according to Sutilov [40]. The variables are the displacement ξ_0, the acoustic velocity $\dot{\xi}_0$ the acceleration $\ddot{\xi}_0$ and the acoustic pressure p_0.

into a volume change of the ceramic. A commonly used ceramic is barium titanate ($BaTiO_3$). A sketch of barium titanate is provided in **Figure 2.3(a)** and **Figure 2.3(b)**. The crystal is a dipol due to the fact that the ions are not positioned symmetrically. When an external voltage is applied the crystal responds with a volume change.

The change of volume caused by an electric voltage U_{Sender} is a material property of the piezoelectric ceramic. The thickness change Δx of a piezoelectric ceramic is a linear function of the piezoelectric modulus d_{33} when the voltage is applied over the surface of the ceramic:

$$\Delta x = d_{33} \cdot U_{\text{Sender}} \qquad (2.7).$$

At the Receiver the opposite effect is achieved. A volume change due to the received pressure pulse generates a voltage U_{Receiver}. This voltage is proportional to the electric deformation constant h_{33} which connects the volume change with the generated voltage. Alternatively the pressure change Δp can be connected with the piezoelectric pressure constant g_{33} and the thickness of the piezoelectric material h_{Receiver}, which converts the applied pressure directly into a generated voltage:

$$U_{\text{Receiver}} = h_{33} \cdot \Delta x = \Delta p \cdot h_{\text{Receiver}} \cdot g_{33} \qquad (2.8).$$

This equation is valid for a Sender/ Receiver operating in thickness mode. This means that only geometric changes of the thickness occur. Combining the piezoelectric modulus and the piezoelectric deformation constant gives the electro-mechanic coupling constant

$$\frac{U_{\text{Receiver}}}{U_{\text{Sender}}} = k_{33}^2 = d_{33} \cdot h_{33} \qquad (2.9).$$

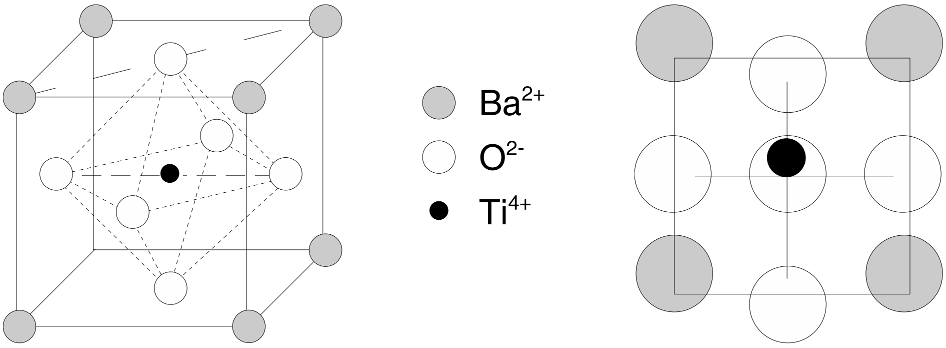

(a) 3D view of the structure of barium titanate.

(b) 2D view of the structure of barium titanate.

Figure 2.3: Structure of barium titanate from [19]. The structure of the crystal is not symmetrical as the Ti^{4+}-ion is slightly offset from the centre line of the crystal. This creates a dipol which will change its volume when an external voltage is applied.

This constant basically gives the effectiveness of a piezo Sender/ Receiver set-up when all volume change is transferred from Sender to Receiver without any losses. If instead a thin plate is used to produce and receive the sound the coupling constant is smaller as volume changes and distortion effects become more important. This coupling constant k_t is therefore smaller than k_{33}.

To generate a pulse in the ceramic an initial electric pulse is applied across its surface. This leads to an initial pulse in the form of a volume or pressure change at opposite surfaces of the ceramic. At the surface a part of the pulse is emitted into the medium and a part travels into the ceramic. The fraction of the pulse travelling through the ceramic respectively the medium is dependent upon the acoustic impedance Z of the ceramic and the surrounding medium. The generation of a pulse is shown in **Figure 2.4** where the ultrasonic transducer has its left surface exposed to air, which leads to the entire impulse at this side of the transducer being reflected within the ceramic. This approximation can be made when the acoustic impedance Z_{air} of the air is much smaller than the acoustic impedance Z_{Sender} of the Sender. In the next cycle a part of the pulse travelling through the ceramic is emitted into the medium and the remaining part is reflected at the phase boundary between ceramic and medium. This leads to a reduction of the pulses amplitude during each subsequent cycle.

The frequency of the generated sound-field depends on the thickness of the Sender whereas the radiated acoustic pressure depends also on the properties of the medium into which the sound-field is radiated. The frequency f itself depends upon thickness of the Sender and is connected via

$$h_{\text{Sender}} = \frac{\lambda}{2} = \frac{c \cdot f}{2} \tag{2.10}$$

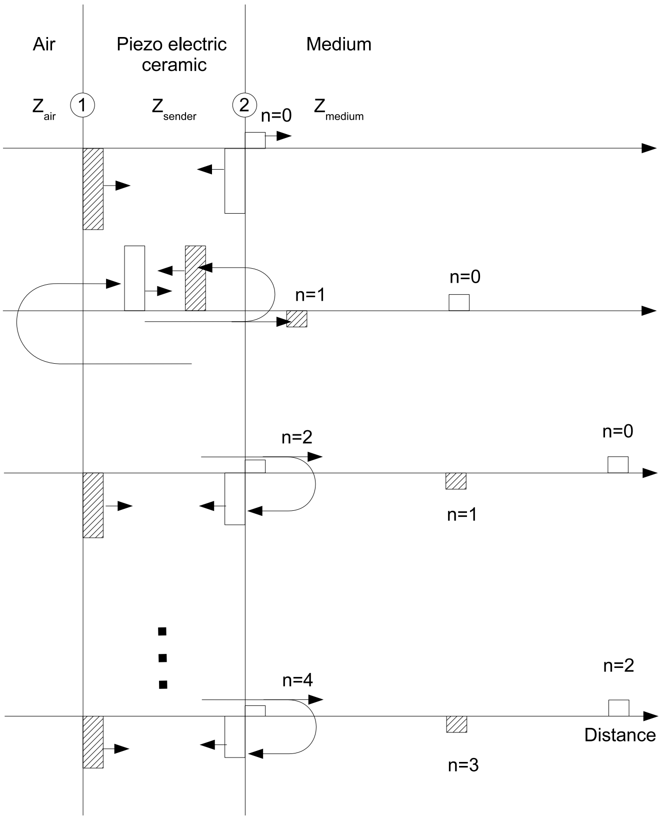

Figure 2.4: Applying an electric pulse between boundaries 1 and 2 generates a pressure pulse at the interface, which travels through both the ceramic and the surrounding medium. Depending upon the impedance of the different materials, a part of the pulse is reflected at the interface and a part of it is transmitted. The height of the bar represents the amplitude of the pulse. The hatching helps to differentiate between the two pulses. With each additional oscillation between the boundaries 1 and 2 the pulse strength decreases. [19]

with the speed of sound c in the Sender and the wavelength λ of the soundfield in the ceramic.

The emitted acoustic pressure depends on the physical properties of the Sender and the surrounding medium. One initial pulse $\hat{p}$ is generated in the Sender. Due to internal reflection and transmission into the medium, the pulse declines with time. With each cycle i a pulse is emitted from the Sender into the medium. For $i \in \mathbb{N}_+$ the value of this pulse is

$$p(i) = \hat{p} \cdot T_{\mathrm{P,\ T/M}} \cdot R^i_{\mathrm{P,\ T/M}} \qquad (2.11)$$

with the transmission coefficient T and the reflection coefficient R. The index P expresses that the coefficient is valid for acoustic pressure and the index T/M stands for the transmission from the transducer into the medium. The transmission coefficient T gives the part of the pulse which is emitted into the medium, and the reflection coefficient R is proportional to the part of the pulse remaining in the Sender. Equations to calculate these coefficients are given in **Table 2.2**.

Sender and Receiver in the *Mutec Penetration Dynamics Analyser* are made from the same material and have the same geometric size and shape. Sender and Receiver are a dynamic system. In order to describe the Receiver response, the pulse leaving the Sender has to be known. A mathematical description of the pulse generated in the Sender is given by Equation (2.11). This pulse travels to the Receiver and a part crosses the phase boundary (2) as shown in **Figure 2.5**. This part is called $I(i)$ and is obtained by multiplying Equation (2.11) with the Transmission coefficient $T_{P,M/T}$:

$$I(i) = T_{P,T/M} \cdot T_{P,M/T} \cdot R^i_{P,T/M} = k \cdot R^i_{P,T/M} \qquad (2.12).$$

The remaining pulse is reflected and no longer available for detection. Hence the energy $S(i)$ stored in the Receiver is increased by $I(i)$. At the same time, when the pulse $I(i)$ arrives at the Receiver and enters, a part of the stored energy $S(i-1)$ is transmitted across the phase boundary (2) into the medium. This part is called $O(i)$ and depends on the energy $S(i-1)$ stored in the Receiver before the new pulse enters and on the transmission coefficient $T_{P,T/M}$:

$$O(i) = T_{P,T/M} \cdot S(i-1) \qquad (2.13).$$

The pulse remaining in the Receiver is therefore

$$(1 - T_{P,T/M}) \cdot S(i-1) = R_{P,T/M} \cdot S(i-1) \qquad (2.14).$$

The mechanism for the pulse generation is described in [19]. It assumes that the entire pulse leaving the Sender arrives at the Receiver, with no losses between Sender and Receiver.

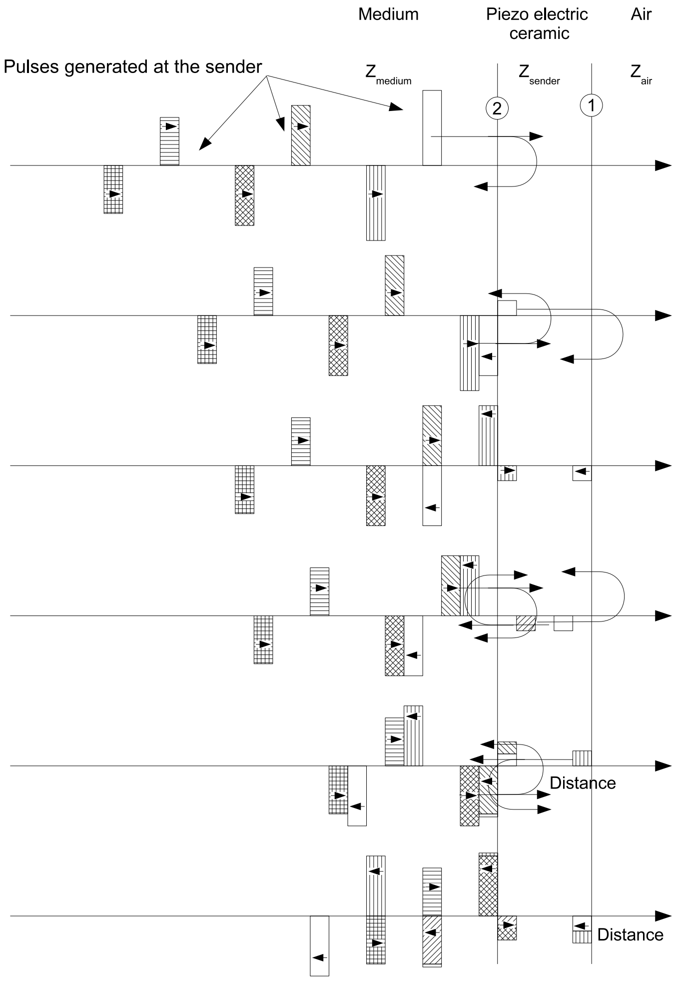

Figure 2.5: Simple model for a piezoelectric ceramic used as a Receiver. The pulse which has to be detected is generated in a Sender of the same properties as the Receiver. As a result of this the incoming pulse is in phase with the resonance frequency of the Receiver and its amplitude declines. Initially no energy is stored in the Receiver. Part of the first pulse crosses the phase boundary (2). The remaining part is reflected (rows 1 to 3). In the next cycle (rows 4 to 6), the next pulse arrives. Part of it is transmitted across the phase boundary and the remaining part of it is reflected. The transmitted part is added to the pulse in the ceramic. Part of the pulse in the ceramic is transmitted through the phase boundary (2) and the major part is reflected. A pulse is built up like this until the incoming part of the pulse is smaller than the part leaving the ceramic.

2.1.2 Sound-field generated by a piston transducer

The sound-field generated by a transducer behaving like a piston can be described using Huygens's principle of superimposing point-sources. Characteristic of a piston transducer is the fact that the entire surface of the transducer vibrates at the same maximum speed and also in phase. To calculate the sound-field emitted by a piston transducer point-sources are assumed to be spread over the entire surface of the Sender. These point-sources emit sound waves which at any arbitrary point outside the Sender interfere with each other. This leads to an area outside the Sender where interference occurs which is called the near-field. At a certain distance from the Sender the sound-field becomes similar to a spherical wave. This area is called the far-field. The near-field and the far-field for a piston transducer can be seen in **Figure 2.8** in which the envelope of the emitted pressure of a piston transducer is plotted. The near-field is characterized by a multitude of minima and maxima. The area of the near-field is described by $-0.005 \text{ m} < r_o < 0.005 \text{ m}$ and $0 < z_o < 0.03 \text{ m}$. The far-field is in the area described by $-0.005 \text{ m} < r_o < 0.005 \text{ m}$ and $0.03 \text{ m} < z_o$.

The sound-field generated by a piston transducer can be calculated using an equation first given by Rayleigh [36]. The radiating surface S can be described as a complex function of the angular frequency ω, the density ρ of the medium, the time t, the wave number $k = 2\pi/\lambda$ with the wavelength $\lambda = 2\pi c/\omega$, the maximum velocity $v_{\max}(t)$ of the radiating surface, the speed of sound c in the medium and the distance d from the source.

$$p(d) = \frac{\imath \cdot \omega \cdot \rho}{2 \cdot \pi} \cdot e^{\frac{\imath \cdot \omega \cdot t}{2 \cdot \pi}} \cdot \int_S v_{\max}(t) \cdot \frac{e^{-\imath \cdot k \cdot d}}{d} dS \tag{2.15}$$

The pressure on the centre-line perpendicular to the surface of the Sender according to Equation (2.15) can be evaluated analytically assuming a constant maximum velocity $v_{\max}(t) = v_{\max}$ of the surface and a circular shape of the transducer. The circular source has a diameter D. The z-axis is perpendicular to the surface of the source and has its origin in the center of the Sender. The pressure $p_z(z_o)$ is calculated for an observer at a distance $d = z_o$ from the Sender on the z-axis. The resulting solution to Equation (2.15) is then [19]

$$p_z(z_o, t) = 2 \cdot c \cdot \rho \cdot v_{\max} \cdot \left(\cos\left[\frac{t \cdot \omega}{2 \cdot \pi} - \frac{z_o \cdot \omega}{c}\right] - \cos\left[\frac{t \cdot \omega}{2 \cdot \pi} - \frac{\sqrt{\left(\frac{D}{2}\right)^2 + z_o^2} \cdot \omega}{c}\right] \right) \tag{2.16}$$

with the envelope

$$|p_z(z_o)| = \left| 2 \cdot \rho \cdot c \cdot v_{\max} \cdot \sin\left(\frac{\pi}{\lambda} \left[\sqrt{\left(\frac{D}{2}\right)^2 + z_o^2} - z_o \right] \right) \right| \qquad (2.17).$$

The dimension of Equation (2.17) can be eliminated by building the ratio of $p(z_o)$ and p_o using $p_o = \rho \cdot c \cdot v_{\max}$:

$$p_z^*(z_o) = \left|\frac{p(z_o)}{p_o}\right| = \left| 2 \cdot \sin\left(\frac{\pi}{\lambda}\left[\sqrt{\left(\frac{D}{2}\right)^2 + z_o^2} - z_o\right]\right)\right| \qquad (2.18).$$

Equation (2.18) is plotted in **Figure 2.6.** Due to interference, points where the maximum pressure is zero exist in the near-field. Interference also causes the maximum pressure in the sound-field to be twice the maximum pressure on the surface of the emitter. For points at large distances z_o from the transducer, Equation (2.17) can be approximated. The argument of the sinus function can be approximated for $\frac{D}{2} \ll z_o$ by:

$$\frac{\pi}{\lambda}\left[\sqrt{\left(\frac{D}{2}\right)^2 + z_o^2} - z_o\right] \approx \frac{\pi}{\lambda}\left[\frac{\left(\frac{D}{2}\right)^2}{2 \cdot z_o}\right] \qquad (2.19).$$

This approximation becomes very small for large z_o and the sinus function can be approximated by its argument. This approximates Equation (2.17) to become

$$|p_z(z_o)| \approx \left| \rho \cdot c \cdot v_{\max} \cdot \frac{\pi}{\lambda} \cdot \frac{\left(\frac{D}{2}\right)^2}{z_o}\right| \qquad (2.20)$$

as given in Krautkrämer and Krautkrämer [19]. Equation (2.20) is the solution to the pressure distribution of a spherical wave as it is radiated by a point-source.

The near-field finishes after the last maximum of the envelope (2.17). From this point on the sound-field is called the far-field. The distance N from the Sender to the last maximum can be calculated as

$$N = \frac{D^2 - \lambda^2}{4\lambda} \qquad (2.21)$$

and is called the near-field distance. For the same wavelength the near-field distance becomes larger, the larger the diameter of the transducer gets. This is shown in **Figure 2.7**. Goldstein et al. [15] measure the axial pressure distribution of circular Senders. As the applied receiver has a certain extent, i.e. cannot be regarded as a point, the results in the near-field are distorted, as an average pressure is measured. The results for the far-field give similar values to those predicted by the theory.

The sound pressure in locations different from the centre-line of the Sender can no longer be calculated analytically. Equation (2.15) and its envelope have to be evaluated numerically. The accuracy of the numeric values is checked for a calculation of the pressure on the centre line and the result is

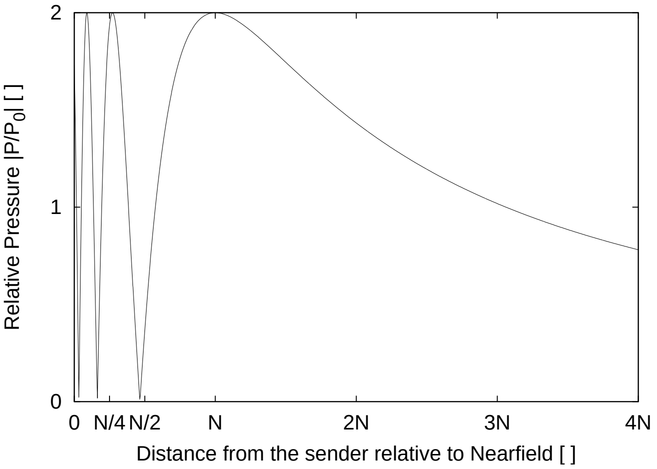

Figure 2.6: Envelope of the absolute of the pressure of sound. The near-field ends after the last maximum. From this point onwards the pressure distribution is monotone and declines. In the calculation the wavelength is $\lambda = 1.5 \cdot 10^{-3}$ m and the diameter of the Sender is $D = 0.01$ m

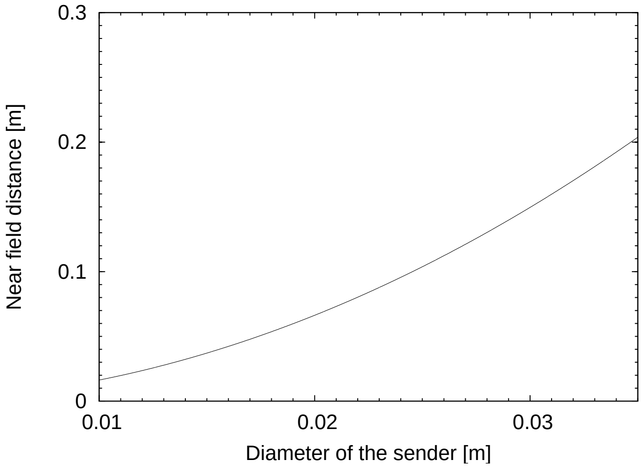

Figure 2.7: The near-field distance is a function of the diameter D of the ultrasonic Sender. The larger the Sender the higher the near-field distance. The wavelength used to calculate this graph is $\lambda = 1.5 \cdot 10^{-3}$ m, a value typical of ultrasound with the frequency 1 MHz in water.

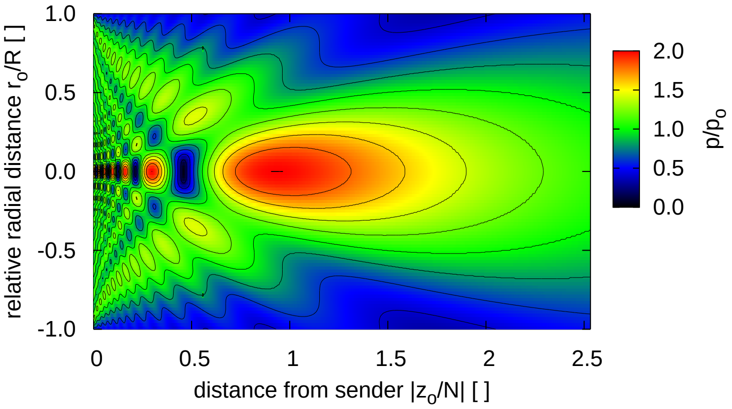

Figure 2.8: Plot of the envelope of the relative pressure distribution P/P_0 with the maximum pressure P_0 at the surface of the Sender. Equations (2.15) and (A.31) are evaluated in order to obtain the envelope. The acoustic pressure is generated by a circular Sender with the diameter 0.01 m. The medium is water with the speed of sound $c = 1500$ m/s. The frequency of the ultrasound is 2 MHz. Similar graphs can be found in [19].

given in **Figure A.4**. The result of a two dimensional numerical calculation of the envelope of a sound-field is plotted in Figure 2.8.

The near-field is at the bottom of the graph, just in front of the Sender. The far-field is further up. It can be seen that the beam spreads once it has reached the far-field. This spread is called geometric spread. A profile of the pressure distribution parallel to the Sender can be obtained by cutting the beam at any distance z_o in the far-field, as shown in **Figure 2.9**.

In order to obtain Figure 2.9 a two-dimensional integration has to be evaluated numerically. To calculate the average pressure at the Receiver a second two-dimensional integration over its surface has to be evaluated. The wavelength is small compared to the dimension of the Sender/Receiver and the integrand contains an oscillating function. This implies a fine resolution for the numerical integration and consequently a time-consuming evaluation. With the help of the first order Bessel function J_1 this calculation can be simplified. The beam profile at any point in the far-field is approximated by

$$p(z_o) = 2 \cdot |p_z(z_o)| \cdot \frac{J_1(X)}{X} \tag{2.22}$$

with

$$X = \pi \cdot \frac{D}{\lambda} \cdot \sin\phi \tag{2.23}$$

as given in [19, p. 76]. In this Equation the pressure $p(z_o)$ is from Equation (2.17), the diameter D of the Sender, the wavelength λ of the ultrasound

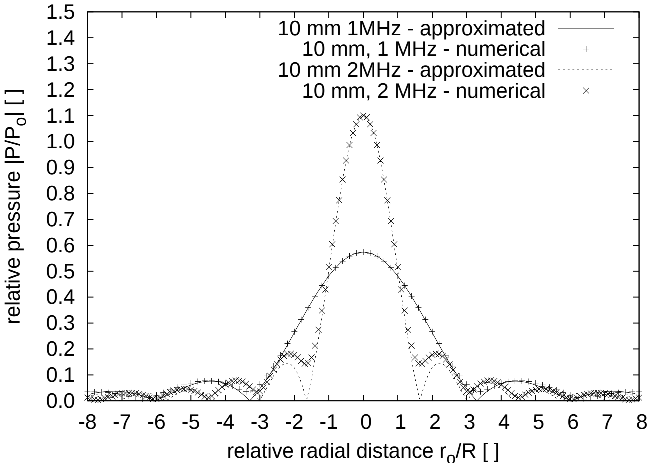

Figure 2.9: Pressure profile of a beam generated with a piston transducer. The piston transducer has the diameter 10^{-2} m and the distance z_o is $9 \cdot 10^{-2}$ m. The medium in which the ultrasound propagates is water with a density of $\rho = 10^3$ kg/m^3 and a speed of sound $c = 1500$ m/s The symbols represent the numerical evaluation of Equation (2.17). The lines represent the approximation of Equation (2.17) with Equation (2.22). The x-axis is normalised to the radius of the Sender. Until the first local minimum of Equation (2.17) the approximation by Equation (2.22) is very good. For the 1 MHz Sender this represents about 3 times the radius of the Sender and for the 2 MHz Sender it is about 1.5 times the radius of the Sender. Within one radius, which also represents the Receiver, the approximation is good for both frequencies.

and the angle ϕ between the perpendicular of the centre-line of the Sender and the point of observation. Equation (2.22) can of course be rearranged to give a relative pressure:

$$p^* = 2 \cdot p_z^*(z_o) \cdot \frac{J_1(X)}{X} \tag{2.24}$$

In Figure 2.9 the numerical evaluation of Equation (2.18) and its approximation by Equation (2.24) are plotted. The distance z_o is $9 \cdot 10^{-2}$ m. It is evident that the approximation becomes worse as the distance from the centre-line increases, but within one radius of the Sender the approximation is very good.

2.1.3 Pressure detected by a Sender-Receiver set-up

Equation (2.15) describes the pressure at a single point of the sound-field. Medium and Receiver have a different acoustic impedance. This means that only a part of the pressure in the medium is transmitted across the phase boundary between medium and Receiver. The part-pressure transmitted across the phase boundary can be calculated with the transmission coefficient $T_{\mathrm{P,\ M/R}}$ taken from Table 2.2. The pressure p_r in the Receiver can then be described with:

$$p_r(\vec{r}_r, t) = T_P \cdot p(d, t) \qquad (2.25).$$

The pressure in the medium at the boundary between medium and Receiver is $p(d, t)$. The detected pressure, which is translated into a voltage by the Receiver, is $p_r(\vec{r}_r, t)$. This leads to an equation for the Sender-Receiver-set-up. The pressure which is detected by a Receiver of the same dimension as the Sender is

$$p = \frac{\rho \cdot v \cdot \omega}{2 \cdot \pi} \cdot \frac{4}{\pi D^2} \cdot \int_0^{D/2} \int_0^{2\pi} \int_0^{D/2} \int_0^{2\pi} \frac{r_s \cdot r_o \sin \frac{\omega}{2} \left(\frac{t_{\max}}{\pi} - \frac{2 \cdot d}{c} \right)}{d} d\varphi_s \, dr_s \, d\varphi_o \, dr_o \tag{2.26}$$

with the distance

$$d = \sqrt{r_o^2 + r_s^2 + z_o^2 - 2 \cdot z_o \cdot z_s + z_s^2 - 2 \cdot r_o \cdot r_s \cdot \cos(\varphi_o - \varphi_s)} \tag{2.27}$$

between an element of the Sender (r_s, φ_s, z_s) and the position (r_o, φ_o, z_o) of an observer and the time $t_{\max}$ for the maximum pressure now being

$$t_{\max} = -\frac{2\pi}{\omega} \cdot \arctan \left(\frac{\int_0^{D/2} \int_0^{2\pi} \int_0^{D/2} \int_0^{2\pi} \frac{r_s \cos\left(\frac{\omega \cdot d}{c}\right)}{d} \, d\varphi_s \, dr_s \, d\varphi_o \, dr_o}{\int_0^{D/2} \int_0^{2\pi} \int_0^{D/2} \int_0^{2\pi} \frac{r_s \sin\left(\frac{\omega \cdot d}{c}\right)}{d} \, d\varphi_s \, dr_s \, d\varphi_o \, dr_o} \right) \qquad (2.28).$$

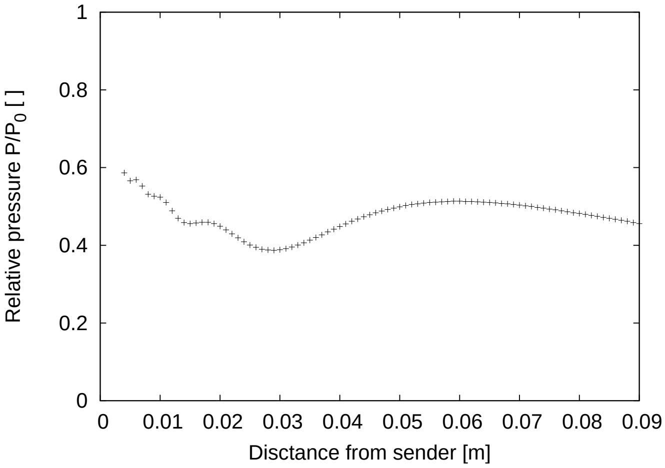

Figure 2.10: Pressure distribution along the centre line for a Sender-Receiver set-up. The values used are for the diameter $D = 10$ mm, frequency of the soundfield $f = 1$ MHz, density of the medium $\rho = 1000$ kg/m^3 and the velocity of sound $c = 1500$ m/s, maximum velocity of Sender surface $v_{\text{max}} = 1$ m/s.

Equations (2.26) and (2.28) are evaluated in **Figure 2.10**.

Comparing Figure 2.10 with Figure 2.6 it can be seen that the variation in pressure evens out and the curve is smoother. The maximum also shifts to larger distances from the Sender.

2.1.4 Attenuation of ultrasound

In the following subsections an overview of different attenuation mechanisms is given. The paper of Mc Clements [25] gives a good summary of ultrasound used in different systems. Mechanisms applying to non-scattering and scattering systems are reviewed.

As the sound wave travels through a medium its intensity decreases due to a range of mechanisms. Losses resulting from viscous friction and reflection at surfaces can occur. The attenuation of ultrasound can be described with the help of an attenuation coefficient. The general attenuation coefficient α of a medium is defined by

$$A = A_0 \cdot e^{-\alpha \cdot x} \tag{2.29}$$

with the initial peak amplitude A_0 and the amplitude A after the peak has travelled the distance x. It contains all sorts of losses. The attenuation coefficient can be specified for different mechanisms of loss. Viscous losses, reflection at phase boundaries and scattering are the most commonly occurring mechanisms. The unit of the attenuation coefficient is Nepers per metre (Np/m).

Viscous friction losses

The attenuation coefficient α_v for losses due to viscous friction in a Newtonian fluid is

$$\alpha_v = \frac{8 \cdot \pi \cdot f^2 \cdot \eta}{3 \cdot \rho \cdot c^3} \tag{2.30}$$

with the frequency f, the viscosity η, the speed of sound c in the medium and the density ρ of the medium [40]. The viscous loss in water over a distance $x = 9$ cm, typical for the *Mutec Penetration Dynamics Analyser*, is only 0.0989% for a frequency of 2 MHz. The attenuation coefficients for a solution of different salts and liquids for frequencies between 5 MHz and 100 MHz can be found in Dunkhin and Goetz [9]. A range of attenuation coefficients which are measured at a frequency of 1.5 MHz for binary mixtures of methanol, ethanol and n-propanol can be found in Petong et al. [31].

Attenuation of ultrasound due to difference in acoustic impedance

Attenuation due to reflection takes place if there is an impedance difference between the two media. The greater the difference, the more reflection will occur and the less transmission will happen (compare Equations (2.34) and (2.35)). The impedance Z_i is defined as the ratio of acoustic pressure p and particle velocity $\dot{\xi}$:

$$Z_i = \frac{p}{\dot{\xi}} = \frac{\omega \cdot \rho}{k} \tag{2.31}.$$

In general Z_i is complex and can be written as

$$Z_i = R_{z,i} + \imath \cdot X_{z,i}, \tag{2.32}$$

where $R_{z,i}$ is called the resistive component and $X_{z,i}$ the reactive component. If $\alpha \ll \omega / c$ the wave number k is dominated by the real part and Z_i becomes

$$Z_i \approx R_{z,i} = \rho_i \cdot c_i, \tag{2.33}$$

and is called the characteristic impedance. The characteristic impedance is a function of the density ρ_i of a medium i and its speed of sound c_i. The transmission and reflection at a boundary between medium 1 and 2 can be described with the help of the transmission coefficient and the reflection coefficient. It is always important to use the transmission and reflection coefficients with regard to the property of the sound-field i.e. displacement, velocity or acceleration. The transmission coefficient $T_{\xi,\,1/2}$ and the reflection coefficient $R_{\xi,\,1/2}$ for the particle displacement for perpendicular incidence of the beam are

$$T_{\xi,\,1/2} = \frac{2 \cdot Z_1}{Z_1 + Z_2}, \tag{2.34}$$

	Reflection	Transmission
Acoustic velocity	$R_{\dot{\xi},\,1/2} = \frac{Z_1 \cos\theta_i - Z_2 \cos\theta_t}{Z_2 \cos\theta_i + Z_1 \cos\theta_t}$	$T_{\dot{\xi},\,1/2} = \frac{2 \cdot Z_2 \cos\theta_i}{Z_2 \cos\theta_i + Z_1 \cos\theta_t}$
Pressure	$R_{\mathrm{p},\,1/2} = \frac{Z_2 \cos\theta_i - Z_1 \cos\theta_t}{Z_2 \cos\theta_i + Z_1 \cos\theta_t}$	$T_{\mathrm{p},\,1/2} = \frac{2 \cdot Z_1 \cos\theta_t}{Z_2 \cos\theta_i + Z_1 \cos\theta_t}$
Intensity	$R_{\mathrm{I},\,1/2} = \left(\frac{Z_2 \cos\theta_i - Z_1 \cos\theta_t}{Z_2 \cos\theta_i + Z_1 \cos\theta_t}\right)^2$	$T_{\mathrm{I},\,1/2} = \frac{4 \cdot Z_1 \cdot Z_2 \cdot \cos\theta_i \cdot \cos\theta_t}{(Z_2 \cos\theta_i + Z_1 \cos\theta_t)^2}$

Table 2.2: Overview of the equations for the determination of the reflection coefficient R and transmission coefficient T of ultrasound at a phase boundary between medium 1 and 2 with regard to acoustic velocity (index $\dot{\xi}$), pressure (index p) and intensity (index I) as a function of the acoustic impedances in media (1) and (2) as defined in Figure 2.11 [40].

and

$$R_{\xi,\,1/2} = \frac{Z_1 - Z_2}{Z_1 + Z_2} \qquad (2.35).$$

If the difference in impedance of the two media is very large, reflection will be large as well. In the case of a wave propagating at an angle to the perpendicular $\theta_i > 0$ as shown in **Figure 2.11**, Equations (2.34) and (2.35) have to be modified using Snell's law. The incident beam and the reflected beam have the same angle towards the normal of the surface. The incident angle θ_i and the transmission angle θ_t are connected via Snell's law, as a function of the wavelengths (λ_1, λ_2) in medium 1 and 2 and the acoustic velocity (c_1, c_2) in the two media:

$$\frac{\sin(\theta_i)}{\sin(\theta_t)} = \frac{\lambda_1}{\lambda_2} = \frac{c_1}{c_2} \qquad (2.36).$$

The determination of the reflection and transmission coefficient is explained in [40, pp. 144]. The transmission and reflection can be determined by a balance at the interface between liquid (1) and solid (2). At the interface the normal components of the stress have to be equal on both sides of the phase boundary. The normal components of the acoustic velocity have to be equal as well. These balances can be used to obtain the reflection and transmission coefficients with regard to the acoustic velocity, pressure and intensity of ultrasound. The results are listed in Table 2.2. Rearranging Equation (2.36) gives for the cosine of the angle of the transmitted beam

$$\cos\theta_t = \sqrt{1 - \left(\frac{c_2 \cdot \sin\theta_i}{c_1}\right)^2}, \qquad (2.37)$$

which can be included in the reflection and transmission coefficients. The transmitted intensity I_t is

$$I_\mathrm{t} = (1 - R_\mathrm{I}) \cdot I_0 = T_\mathrm{I} \cdot I_0, \tag{2.38}$$

$$I_\mathrm{t} = I_0 \cdot \left(1 - \left(\frac{Z_2\cos(\theta_i) - Z_1\cos(\theta_t)}{Z_2\cos(\theta_i) + Z_1\cos(\theta_t)}\right)^2\right) \tag{2.39}$$

or

$$I_\mathrm{t} = I_0 \cdot \left(\frac{4 \cdot Z_1 \cdot Z_2\cos(\theta_i)\cos(\theta_t)}{\left(Z_2\cos(\theta_i) + Z_1\cos(\theta_t)\right)^2}\right) \qquad (2.40).$$

Inserting Equation (2.36) into Equation (2.40) gives

$$I_t = I_0 \cdot \left(\frac{4 \cdot Z_1 \cdot Z_2\cos(\theta_i) \cdot \sqrt{1 - \sin(\theta_i)}}{\left(Z_2\cos(\theta_i) + Z_1 \cdot \sqrt{1 - \sin(\theta_i)}\right)^2}\right) \qquad (2.41).$$

In Equation (2.41) the term in brackets is the transmission coefficient T_I for ultrasonic intensity.

When a longitudinal wave crosses a boundary between a liquid and a solid the form of the wave can change into a transversal wave and a longitudinal wave as shown in Figure 2.11. The change of one form of ultrasonic wave into another form of ultrasound is called mode change. In the above case the mode change occurs due to the fact that in a solid shear stress can be propagated. In a solid the speed of sound c_{S2} of the transverse wave differs from the speed of sound c_2 of the longitudinal wave, which leads according to Equation (2.36) to two different transmission angles. The derivation of this case and other cases is discussed in [40, pp 216].

For completeness, a third form of ultrasound can occur additionally to this, namely the surface or Lamb wave. It travels on the surface of solids.

With the help of Equation (2.36) a transmission coefficient for a plane plate can be derived [40, pp 173]. In his derivation of an expression for the transmission coefficient Sutilov [40] neglects mode change from a longitudinal to a transverse wave and obtains an estimate for the transmission coefficient. A short reproduction of this way follows now, as the general case is modified later.

The plate has the thickness d, the acoustic impedance Z_2 and the wave number k_2. The surrounding liquid has the acoustic impedance Z_1. Stating and solving a pressure balance and the equality of acoustic velocity and pressure at the two interfaces of the plate at ($x \in \{0; d\}$) gives four equations. The incoming wave is called ϕ_1. The reflected part of this wave is ϕ_1' and the transmitted part is ϕ_2. Part of the transmitted wave is then reflected at the

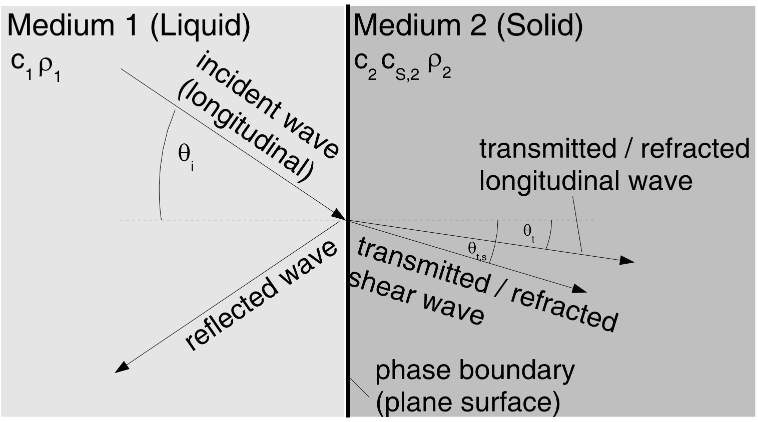

Figure 2.11: A connection between the physical properties of two media separated by a phase boundary and the angle of the incident and transmitted beam is given by Snell's law. When a longitudinal wave propagating in a liquid encounters a phase boundary of a solid, a part of the incident wave is reflected and another part is transmitted across the phase boundary. The transmitted part of the wave is split up into a longitudinal wave and a transverse wave due to the ability of the solid to transmit shear waves. The longitudinal wave and the transverse wave have different speeds c_2 and $c_{S,2}$. Sketch taken from [40, p. 221].

second boundary. This part is called ϕ_2' and the transmitted part is called ϕ_3. The angle of the incident beam is θ_1 and the angle of the diffracted beam θ_2, the wave numbers in the media are k_1 and k_2 and the densities are ρ_1 and ρ_2. A more detailed derivation of the expression for the reflection coefficient for a plate is shown in the appendix on page 143 pp.

The wave equations in cartesian coordinates (x, y) are

$$\begin{aligned}
\phi_1 &= \phi_{1,\text{ max}} \cdot \exp\{\imath[\omega \cdot t - k_1 \cdot (x \cdot \cos(\theta_1) + y \cdot \sin(\theta_1)]\}, & (2.42)\\
\phi_1' &= \phi_{1,\text{ max}}' \cdot \exp\{\imath[\omega \cdot t + k_1 \cdot (x \cdot \cos(\theta_1) - y \cdot \sin(\theta_1)]\}, & (2.43)\\
\phi_2 &= \phi_{2,\text{ max}} \cdot \exp\{\imath[\omega \cdot t - k_2 \cdot (x \cdot \cos(\theta_1) + y \cdot \sin(\theta_2)]\}, & (2.44)\\
\phi_2' &= \phi_{2,\text{ max}}' \cdot \exp\{\imath[\omega \cdot t + k_2 \cdot (x \cdot \cos(\theta_1) - y \cdot \sin(\theta_2)]\}, & (2.45)\\
\phi_3 &= \phi_{3,\text{ max}} \cdot \exp\{\imath[\omega \cdot t - k_1 \cdot (x \cdot \cos(\theta_1) + y \cdot \sin(\theta_1)]\} & (2.46).
\end{aligned}$$

The balance for $x = 0$ is then

$$\begin{aligned}
\rho_1 \cdot (\phi_1 + \phi_1') &= \rho_2 \cdot (\phi_2 + \phi_2'), & (2.47)\\
k_{1,x} \cdot (\phi_1 - \phi_1') &= k_{2,x} \cdot (\phi_2 - \phi_2') & (2.48)
\end{aligned}$$

and for $x = d$

$$\begin{aligned}
\rho_2 \cdot (\phi_2 + \phi_2') &= \rho_1 \cdot \phi_3, & (2.49)\\
k_{2,x} \cdot (\phi_2 - \phi_2') &= k_{1,x} \cdot \phi_3 & (2.50)
\end{aligned}$$

with the $k_{1,x} = k_1 \cdot \cos\theta_1$ and $k_{1,x} = k_2 \cdot \cos\theta_2$.

The reflection coefficient $R_{\text{p, plate}}$ of the plate with regard to the acoustic pressure is then

$$R_{\text{p, plate}} = \text{Real}\left(\frac{\phi_1'}{\phi_1}\right) = \text{Real}\left(\frac{\exp\left\{\imath \cdot 2 \cdot k_2 \cdot d \cdot \cos\left(\theta_2\right)\right\} \cdot A + B}{\exp\left\{\imath \cdot 2 \cdot k_2 \cdot d \cdot \cos\left(\theta_2\right)\right\} \cdot C + D}\right) \quad (2.51)$$

with

$$A = \left(\frac{\rho_1}{\rho_2} + \frac{k_{1,x}}{k_{2,x}}\right) \cdot \left(\frac{\rho_2}{\rho_1} - \frac{k_{2,x}}{k_{1,x}}\right), \quad (2.52)$$

$$B = \left(\frac{\rho_1}{\rho_2} - \frac{k_{1,x}}{k_{2,x}}\right) \cdot \left(\frac{\rho_2}{\rho_1} + \frac{k_{2,x}}{k_{1,x}}\right), \quad (2.53)$$

$$C = \left(\frac{\rho_1}{\rho_2} + \frac{k_{1,x}}{k_{2,x}}\right) \cdot \left(\frac{\rho_2}{\rho_1} + \frac{k_{2,x}}{k_{1,x}}\right), \quad (2.54)$$

$$D = \left(\frac{\rho_1}{\rho_2} - \frac{k_{1,x}}{k_{2,x}}\right) \cdot \left(\frac{\rho_2}{\rho_1} - \frac{k_{2,x}}{k_{1,x}}\right) \quad (2.55).$$

Hence the transmission coefficient is

$$T_{\text{p, plate}} = 1 - R_{\text{p, plate}} \quad (2.56).$$

An evaluation of Equation (2.56) is shown in **Figure 2.12** for a plate made of polycarbonate as a function of the thickness of the plate. The transmission coefficient depends on the thickness of the plate as well as the wavelength of the ultrasound within the plate.

Attenuation due to scattering

The intensity of ultrasound can also decrease through scattering. Depending on the nature of the scatterers, different forms of scattering can occur. If the scattering centres are small enough – $k \cdot R \ll 1$ – Rayleigh scattering occurs. Here $k = \frac{2 \cdot \pi}{\lambda}$ is the wave number, R is the radius of the scattering centres and λ is the wave length. The scattering of particles can be characterised using the scattering cross-section σ_s of a particle. It is defined as the ratio of the total scattered power D_s and the intensity of the incident beam I_0 [40]:

$$\sigma_s = \frac{D_s}{I_0} \quad (2.57).$$

The total scattered power D_s can be obtained integrating the scattered intensity I_s in each direction θ over the surface of a sphere [20, 40]

$$D_s = \int_0^\pi I_s \cdot 2 \cdot \pi \cdot d^2 \cdot \sin\theta \; d\theta \quad (2.58)$$

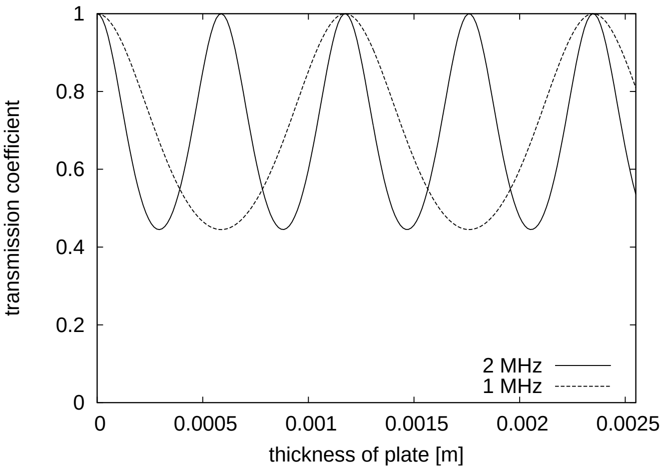

Figure 2.12: Plot of the transmission of ultrasound through a plate made from polycarbonate in the surrounding liquid water as a function of the thickness of the plate according to Equation (2.56). The angle of the incident beam is 9.5 °. The generation of a shear wave in the plate is neglected here. The transmission depends on the thickness and the wavelength.

with the distance d between scatterer and observer. For the scattering of a small incompressible stationary sphere with the radius R the scattered intensity I_s at large distances d is

$$I_s = I_0 \cdot \frac{k^4 \cdot R^6}{9 \cdot d^2} \cdot \left(1 + \frac{3}{2} \cdot \cos\theta\right)^2 \qquad (2.59)$$

which leads to an expression for the total scattered intensity

$$D_s = \frac{7}{9} \cdot \pi \cdot d^2 \cdot k^4 \cdot R^4 \cdot I_0 \qquad (2.60)$$

or the effective scattering area of a particle

$$\sigma_s = \frac{7}{9} \cdot \pi \cdot R^2 \cdot (k \cdot R)^4 \qquad (2.61).$$

Rayleigh also solved the problem of a small compressible particle with the compressibility K_s and the density ρ_s in a medium with the compressibility K_m and the density ρ_m, obtaining for the scattered intensity

$$I_s = I_0 \cdot \frac{k^4 \cdot R^6}{9 \cdot d^2} \left(\frac{K_s - K_m}{K_s} + 3 \cdot \frac{\rho_s - \rho_m}{2 \cdot \rho_s + \rho_m} \cdot \cos\theta\right)^2 \qquad (2.62).$$

With Equation (2.58) this leads to the effective scattering area for Rayleigh scattering of

$$\sigma_s = \frac{4}{9} \cdot \pi \cdot R^2 \cdot (k \cdot R)^4 \cdot \left(\left(\frac{K_s - K_m}{K_s}\right)^2 + 3 \cdot \left(\frac{\rho_s - \rho_m}{2 \cdot \rho_s + \rho_m}\right)^2\right) \qquad (2.63).$$

Minnaert [28] concludes that this equation does not describe the behaviour of gas bubbles in a liquid. By solving the energy balance of the displaced water and the compressed air when a bubble is pulsating, he obtains the resonance frequency f_r

$$f_r = \frac{1}{2 \cdot \pi \cdot R} \cdot \sqrt{\frac{3 \cdot \kappa \cdot P}{\rho}}\,, \tag{2.64}$$

which is a function of the adiabatic compressibility of the gas $\kappa = C_p/C_v$, the ratio of heat capacity at constant pressure and constant volume. It is also a function of the ambient pressure P. The bubble then radiates a sound-field which leads to a scattering cross-section which, for air in water, is larger than found in Equation (2.63). For air in water with $\kappa = 1.4$, the pressure $P = 10^5$ Pa, the density of water $1000\,\mathrm{kg/m^3}$ the resonance frequency can be calculated as

$$f_r = \frac{3.26}{R}\ \mathrm{Hz} \qquad (2.65).$$

A bubble which has been subject to an initial pulse will follow a harmonic oscillation with resonance frequency if no dissipative energy losses occur. Leighton [21] develops Minnaert's solution in a slightly different way which also enables him to calculate the scattering cross-section of a bubble. As it is of importance later on, a brief survey of the derivation is given now. A differential equation describing the bubble-wall movement ξ is solved. In the case of the free oscillating bubble the equation is

$$m \cdot \ddot{\xi} + k \cdot \xi = 0 \tag{2.66}$$

with the mass m of the displaced liquid and the spring constant k due to the elasticity of the bubble. The solution to this is

$$\xi = \Xi_1 \cdot e^{\imath \cdot \omega . t} + \Xi_2 \cdot e^{-\imath \cdot \omega . t} \tag{2.67}$$

with the angular resonance frequency of the oscillation

$$\omega_0 = \sqrt{k/m} \tag{2.68}$$

and the constant Ξ_1 and Ξ_2, which may be complex. With appropriate calculations [21] it is found that $\omega_0 = 2 \cdot \pi \cdot f_r$, with f_r from Equation (2.68). This situation is then developed further to the situation of the bubble in a sound-field, being a coupled system consisting of the bubble and the sound-field. This is described by a differential equation for the bubble with an external force F_0 which oscillates at the frequency ω:

$$m \cdot \ddot{\xi} + k \cdot \xi = F_0 \cdot e^{\imath \cdot \omega \cdot t} \qquad (2.69).$$

The solution to this equation is

$$\xi = \Xi_1 \cdot e^{\imath \cdot \omega_0 \cdot t} + \Xi_2 \cdot e^{-\imath \cdot \omega_0 \cdot t} + A \cdot e^{\imath \cdot \omega \cdot t} \tag{2.70}$$

with the angular resonance frequency $\omega_0 = 2 \cdot \pi \cdot f_r$ of the bubble and the angular frequency ω of the sound-field. For the steady state of this oscillation the dominant part of the equation is $A \cdot e^{\imath \omega \cdot t}$. Inserting $\xi = A \cdot e^{\imath \omega \cdot t}$ and $\ddot{\xi} = A \cdot \omega^2 \cdot e^{\imath \omega \cdot t}$ into Equation (2.69) gives an expression for A:

$$A = \frac{F_0}{m \cdot \omega^2 \cdot \left(\left(\frac{\omega_0}{\omega} \right)^2 - 1 \right)} \qquad (2.71).$$

Hence the displacement of the liquid air interface due to the external oscillating force F_0 is

$$\xi = \xi_0 \cdot e^{\imath \cdot \omega \cdot t} = \frac{F_0}{m \cdot \omega^2 \cdot \left(\left(\frac{\omega_0}{\omega} \right)^2 - 1 \right)} \cdot e^{\imath \cdot \omega \cdot t} \qquad (2.72).$$

Equation (2.72) is the answer of the bubble-wall displacement to the external stimulation. The stimulation is the force introduced into the system, which is the right hand side of Equation (2.69). With this the scattering cross-section σ_s can be determined as a function of the surface S of the scatterer [40, p 168]:

$$\sigma_s = \frac{D_s}{I_0} = \frac{I_s \cdot S}{I_0} \qquad (2.73).$$

The scattered intensity I_s and the incident intensity I_0 have to be known. The scattered intensity can be calculated using Equation (2.72) and the expression for the conversion of acoustic velocity into intensity as given by Equation (2.6):

$$\begin{aligned} I_s &= \frac{\rho \cdot c \cdot \dot{\xi}_0}{2} && (2.74) \\ &= \frac{\rho \cdot c \cdot \omega^2 \cdot \xi_0^2}{2} && (2.75) \\ &= \frac{\rho \cdot c \cdot F_0^2}{2 \cdot \omega^2 \cdot m^2} \cdot \frac{1}{\left(\left(\frac{\omega_0}{\omega} \right)^2 - 1 \right)^2} && (2.76). \end{aligned}$$

The intensity of incoming ultrasound is I_0 and can be calculated with the help of the right hand side of Equation (2.69) which describes the oscillating force with the amplitude $F_0 = m \cdot \ddot{\xi}_0$ where $\ddot{\xi}_0$ is the maximum acceleration. Using the equations given in Table 2.1 the acceleration can be expressed as a function of the velocity $\dot{\xi}_0$. $\partial \dot{\xi}_0 / \partial t = \ddot{\xi}_0$ results in $\dot{\xi}_0 = \ddot{\xi}_0 / \omega$ and with

$F_0 = m \cdot \ddot{\xi}_0 \Leftrightarrow \ddot{\xi}_0 = F_0/m$ from Equation (2.69) one obtains

$$I_0 = \frac{\rho \cdot c \cdot \dot{\xi}_0^2}{2} \tag{2.77}$$

$$= \frac{\rho \cdot c \cdot \ddot{\xi}_0^2}{2 \cdot \omega^2} \tag{2.78}$$

$$= \frac{F_0^2 \cdot \rho \cdot c}{2 \cdot \omega^2 \cdot m^2} \tag{2.79}.$$

This leads to the scattering cross-section $\sigma_s = I_s \cdot S/I_0$ as a function of the surface area S:

$$\sigma_s = \frac{S}{\left(\left(\frac{\omega_0}{\omega}\right)^2 - 1\right)^2} \tag{2.80}.$$

By adjusting the Surface area to different geometries the scattering cross-section for a bubble or gas trapped in a pore can be calculated. The scattering cross-section $\sigma_{s,bubble}$ of a bubble with the radius R is then

$$\sigma_{\text{s, bubble}} = \frac{4 \cdot \pi \cdot R^2}{\left(\left(\frac{\omega_{0,bubble}}{\omega}\right)^2 - 1\right)^2} \tag{2.81}$$

and for a circular pore with the radius R and the length h it is

$$\sigma_{\text{s,pore}} = \frac{2\pi \cdot R^2 + 2 \cdot \pi \cdot R \cdot h}{\left(\left(\frac{\omega_{0,pore}}{\omega}\right)^2 - 1\right)^2} \tag{2.82}.$$

The resonance frequencies $\omega_{0,\text{ bubble}} = 2 \cdot \pi \cdot f_r$ for a bubble taken from Equation (2.64) and $\omega_{0,\text{pore}}$ for a pore are different. In Section 3.5 the resonance frequency for a pore is derived.

In a situation where losses due to dissipation occur, the above calculations have to be modified. A dissipative term $b \cdot \dot{\xi}$ with the dampening constant b is included in Equation (2.66) to give

$$m \cdot \ddot{\xi} + b \cdot \dot{\xi} + k \cdot \xi = 0 \tag{2.83}.$$

The resonance frequency ω_d of the damped system is

$$\omega_d = \sqrt{\frac{k}{m} - \frac{b^2}{4 \cdot m^2}} = \sqrt{\omega_0^2 - \beta^2} \tag{2.84}$$

with the resonance frequency ω_0 of the undamped system as given by Equation (2.68) and $\beta = b/(2 \cdot m)$. The scattering cross-section can be calculated in almost the same way as in the undamped case, and the intermediate results become

$$|A| = \frac{F_0/m}{\sqrt{(\omega_0^2 - \omega^2)^2 + (2 \cdot \beta \cdot \omega)^2}} \tag{2.85}$$

and following the same steps as before, the scattering cross-section becomes

$$\sigma_s = \frac{S}{\left(\left(\frac{\omega_d}{\omega}\right)^2 - 1\right)^2 + \left(\frac{2\cdot\beta}{\omega}\right)^2} \qquad (2.86).$$

The different results for the scattering cross-section are plotted in **Figure 2.13**. The physical data for the calculation are air and water. It can be seen that the difference in compressible and noncompressible scattering is small for ultrasound of the same frequency. When resonance is taken into account the scattering cross-section is much larger.

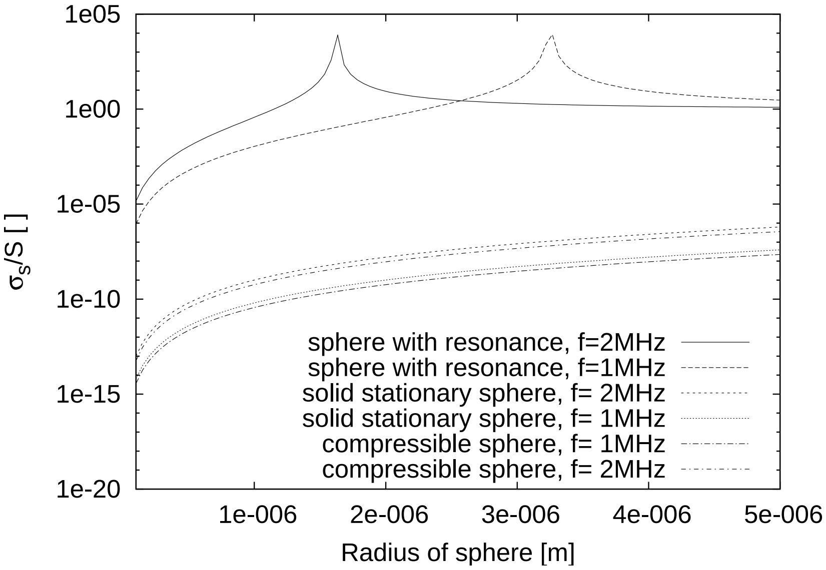

Figure 2.13: Scattering cross-section σ_s in relation to the particle's geometric surface S as a function of the particle diameter for a solid stationary sphere (Equation (2.61)), a compressible sphere (Equation (2.63)) and a sphere with resonance scattering (Equation (2.86)) for two different frequencies (1 MHz and 2 MHz). The density of the liquid is $\rho = 1000\,\text{kg/m}^3$. The scattering cross-section of a bubble with a diameter larger than $1 - 2\ \mu\text{m}$ is in the case of a non-dissipative system, larger than its geometric surface by several magnitudes.

Using the derivation of the resonance frequency Miller and Nyborg [27] give different terms for the dissipation of sound in cylindrical pores, i.e. losses due to scattering and viscous friction as well as losses occurring in the boundary layer. The results are validated using nucleopore membranes. The membranes consist of polycarbonate and have cylindrical pores within a very close diameter range. When in contact with a liquid, the pores will fill with the liquid depending on the contact angle. Miller and Nyborg assume equilibrium conditions at the air-liquid interface and hence no mass transfer between the two phases. They then derive several formulae for the resonance

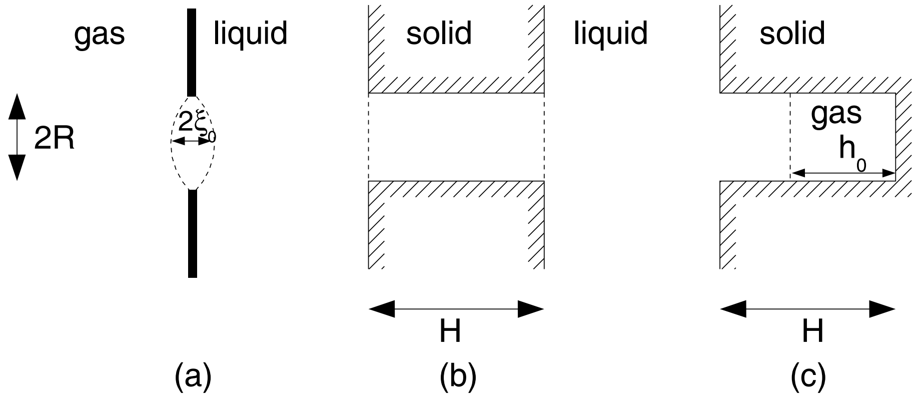

Figure 2.14: Illustration of the three situations considered in Miller [26]:
(a) circular gas-liquid interface at a hole in a rigid baffle,
(b) a straight-through cylindrical pore in a solid sheet of the thickness h,
(c) a cylindrical cavity of the depth H in a solid which is partly filled with gas to a depth h_0.

frequency of nucleopore membranes. The model for the contact line of liquid, gas and membrane varies from clamped to free moving. The clamped contact line results in a drumlike behaviour of the interface. Partly filled pores are considered as well. These situations are shown in **Figure 2.14**.

The result for the resonance frequency $f_{\text{r, clamped}}$ with respect to the clamped contact line as shown in Figure 2.14 (a) is

$$f_{\text{r, clamped}} = \frac{1}{2 \cdot \pi} \sqrt{\frac{15 \cdot \pi \cdot \gamma}{4 \cdot \rho \cdot R^3}} \qquad (2.87).$$

The power loss W dissipated during one oscillation is given as

$$W = d_r \cdot \bar{\dot{\xi}}^2 \qquad (2.88)$$

with the velocity $\bar{\dot{\xi}}$ averaged over the surface and the radiation resistance d_r. For situation (a) the radiation resistance is

$$d_r = \frac{\pi \cdot \omega \cdot k \cdot R^3}{3}, \qquad (2.89)$$

where k is the wave number. The resistance d_v due to viscous flow of a liquid in a capillary is

$$d_v = 2 \cdot \pi \cdot \eta \cdot R \qquad (2.90)$$

as a function of the viscosity η. Losses occurring in the boundary layer of the flowing liquid are captured by the resistance d_b:

$$d_b = \frac{\pi \cdot \rho \cdot \omega \cdot l \cdot R^2}{16} \qquad (2.91)$$

with the density ρ of the liquid and the boundary layer thickness $l = \sqrt{2 \cdot \eta/(\rho \cdot \omega)}$. For cases (b) and (c) in Figure 2.14 two variations are calculated: a so-called clamped contact line model and a model with a free moving contact line where the interface does not change its shape. Case (b) is an extension to case (a) and the resonance frequency is

$$f_{\text{r, clamped}} = \frac{1}{2 \cdot \pi} \sqrt{\frac{120 \cdot \pi \cdot \gamma \cdot H + 15 \cdot \pi \cdot \kappa \cdot P_0 \cdot R^2}{23 \cdot \rho \cdot R^3 \cdot H}} \tag{2.92}$$

being a function of the polytropic exponent κ, the surface tension γ, and the ambient pressure P_0. If the contact line moves freely, the resonance frequency $f_{\text{r, p, free}}$ becomes

$$f_{\text{r, p, free}} = \frac{1}{2 \cdot \pi} \cdot \sqrt{\frac{3 \cdot \pi \cdot \kappa \cdot P_0}{8 \cdot \rho \cdot H \cdot R}} \qquad (2.93).$$

The partly filled pore or cavity with a clamped contact line has the resonance frequency $f_{\text{r, p, clamped}}$

$$f_{\text{r, p, clamped}} = \frac{1}{2 \cdot \pi} \sqrt{\frac{120 \cdot \pi \cdot \gamma \cdot b + 15 \cdot \pi \cdot \kappa \cdot P_0 \cdot R^2}{32 \cdot \rho \cdot R^3 \cdot h_0 + 15 \cdot \rho \cdot R^2 \cdot b(H - h_0)(1 + l/R)}} \qquad (2.94).$$

In addition to the earlier defined variables the length h_0 of the gas volume in the pore is used as shown in Figure 2.14 (c).

The resistance d_p is given by

$$d_p = \frac{1}{2} \cdot \pi \cdot l \cdot R \cdot (H - h_0) \cdot \rho \cdot \omega, \tag{2.95}$$

which is a function of the density ρ of the liquid. The main conclusion of Miller is that the results obtained by measurements of hydrophobic porous membranes is between the results obtained by the two models for the clamped contact line and the free moving contact line, as is discussed in the papers by Miller [26], Miller and Nyborg [27]. However scattering cross-sections for the pores in the membranes are neither derived nor measured.

Regimes of scatterers

In systems with small amounts of scattering centres, the scatterers do not influence each other. The loss in intensity can be calculated as a function of the attenuation coefficient α_s for scattering

$$I(x) = I_0 e^{-\alpha_s \cdot x} \tag{2.96}$$

as a function of the incident intensity I_0 and the distance x. The attenuation coefficient for scattering (α_s) is a function of the scattering cross-section (σ_s) and the number of scatterers (N_s)

$$\alpha_s = N_s \cdot \sigma_s \tag{2.97}$$

The scattering of micro-bubbles has become increasingly important for medical ultrasonic application. The micro-bubbles are usually encapsulated in a shell which separates the air from the surrounding medium. de Jong et al. [8] include this shell in a modified term for the resonance frequency $f_{\text{r, microbubble}}$ of the micro-bubble. Equation (2.68) becomes

$$f^2_{\text{r, micro-bubbles}} = \left(f_r^2 + \frac{2 \cdot S_P}{m \cdot \pi}\right) \tag{2.98}$$

with the shell elasticity factor S_P and the effective mass of the bubble m. The elasticity factor S_P is a property of the material used to generate the micro-bubbles. The attenuation coefficient α_s of a regime of micro-bubbles with different radii r can be calculated with

$$\alpha_s = \int_0^\infty \sigma_s \cdot n(r) dr \tag{2.99}$$

where $n(r)$ is the number of scatterers.

Pietikäinen [32] uses an ultrasonic transmission technique to measure the air content at different positions in a paper machine. He uses an extinction scattering cross-section σ_e which contains all mechanisms of loss of ultrasonic intensity to calculate a loss in signal. The loss in signal is the change in sound pressure level ΔSPL. The bubbles are assumed to be of constant size. The loss in signal ΔSPL is then

$$\Delta SPL = 20 \cdot \log\left(\frac{P(d)}{P(0)}\right) = -10 \cdot \sigma_e \cdot N_s \cdot d \cdot \log e \tag{2.100}$$

where N_s is the number of bubbles per unit volume and $P(0)$ is the pressure amplitude of the incident beam and $P(d)$ is the pressure amplitude of the transmitted and attenuated beam. He also finds that bubbles attached to a solid (i.e. fibre) give a larger scattering cross-section than expected from Equation (2.81).

2.2 Liquid penetration into capillaries

One model substrate used in this thesis to validate the mathematical model for the Mutec is a nucleopore membrane, made of polycarbonate. The pores of the membrane are cylindrical and of a very close size distribution. When these membranes are mounted onto the sample-holder, one end of the capillaries is sealed. This leads to a build-up of pressure when a liquid penetrates into the capillary. This pressure works against the capillary suction.

The dynamics of liquid penetration into capillaries is fairly complex. The liquid is sucked into the capillary depending on the contact angle. The interface between air and liquid is curved. During the process of liquid penetration into the capillary its shape changes. It is not yet fully understood how the contact line moves during the penetration process, in particular when a sound-field is superimposed, as pointed out by Miller and Nyborg [27].

When a liquid penetrates into a capillary which is sealed at one side, different physical processes take place. The liquid penetrates into the capillary due to the capillary suction and replaces the air which occupied the capillary before the process started. As the capillary is sealed, no gas can escape from the system, hence the pressure in the gas increases as it is compressed.

Due to the increase in pressure the equilibrium between the gas in the gas phase and the gas dissolved in the liquid is disturbed, and a mass transfer from the gas phase into the liquid takes place.

The compression of air can take place via different changes of condition. An infinitely slow penetration process does not change the temperature of the gas, as it would be in equilibrium with the surroundings. An adiabatic change of condition occurs when no heat transfer between the gas and the surroundings takes place, implying an increased temperature in the gas.

For the description of the penetration dynamics the velocity profile of the penetrating liquid is of importance as it influences the frictional losses occurring during the penetration. Frictional losses due to the liquid flowing into the capillary are opposed to the capillary suction. In the case of small penetration velocities, the flow profile is laminar otherwise it can be turbulent.

The dynamics of liquid penetration into capillaries can be formally divided into three different regions as shown in **Figure 2.15**.

In the first region the velocity profile changes from a plug flow profile with a uniform velocity across the air-liquid interface to a laminar or parabolic velocity profile. In Figure 2.15 the first region is located at the left side of the air-liquid interface. During this region a boundary layer is formed at the surface of the capillary. Once it has the dimension of the capillary radius, the second region starts. It is the region of the laminar flow, where the velocity profile is still laminar. The third region is the entrance flow where

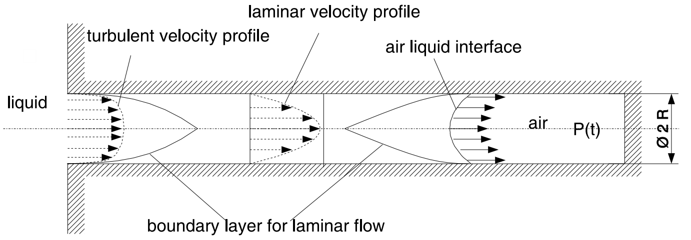

Figure 2.15: Dynamics of liquid penetration into a sealed capillary. From right to left: It is assumed that the air-liquid interface is moving with uniform speed. Depending on the speed a laminar velocity profile develops in the capillary. A laminar velocity profile is characterized by a parabolic shape. The laminar velocity profile exists after a transition distance along the centre-line of the capillary. At the entrance of the capillary liquid is flowing from the bulk into the capillary. The velocity in the bulk is zero. Again, after a transition distance the laminar profile is developed. From Levic [22] but adapted to the situation of a pore in the membrane.

the fluid entering the capillary forms a boundary layer on the capillary wall. The third region lasts as long as the boundary layer thickness is smaller than the radius of the capillary. Whether a laminar profile is developed depends on the volume flow of liquid into the capillary and its dimensions. The Reynolds number Re puts the inertial force in relation to the frictional force. For a capillary the Reynolds number is:

$$\mathrm{Re} = \frac{D \cdot v \cdot \rho}{\eta} \tag{2.101}$$

with the density ρ of the liquid, its viscosity η, the velocity v and the diameter D of the capillary. Values smaller than 2500 indicate laminar flow. The distance x, until the boundary layer thickness is the same as the radius of a capillary, can be approximated according to Levic [22] by:

$$x \approx 0.1 \cdot R \cdot \mathrm{Re} \qquad (2.102).$$

Dynamic penetration processes into capillaries were first described by Lucas [23] and Washburn [41] in 1918 and 1921. The situation in Figure 2.15 is simplified by neglecting the transition regions and only taking viscous laminar friction and capillary suction into account. The Lucas-Washburn-Equation (1.1) can be solved by direct integration with the boundary condition $h(0) = 0$. For a gravity-free situation, as is the case for horizontal capillaries the result for the penetration length $h(t)$ is

$$h(t) = \sqrt{2 \cdot A \cdot t} \tag{2.103}$$

with

$$A = \frac{R^2 \cdot \rho}{8 \cdot \eta} \qquad (2.104).$$

A further development of the Lucas-Washburn-Equation (1.1) is the Bosanquet-Equation (1.2), which takes the inertia of the moving liquid into account. Substituting $h(t) \cdot \dot{h}(t)$ with $z(t)$ the form becomes

$$\dot{z}(t) + A \cdot z(t) = B \tag{2.105}$$

with

$$B = \frac{P \cdot R^2}{8 \cdot \eta}, \tag{2.106}$$

$$P = P_{Laplace} + P_0 = \frac{2 \cdot \gamma \cos(\Theta)}{R} + P_0 \tag{2.107}$$

and A from Equation (2.104). The solution to Equation (2.105) with the starting condition $z(0) = 0$ gives

$$z(t) = \frac{B \cdot e^{-A \cdot t} \cdot \left(e^{-A \cdot t} - 1\right)}{A} \qquad (2.108).$$

In Equation (2.108) the substitution $z(t) = h(t) \cdot \dot{h}(t)$ is performed and the solution with regard to the start condition $h(0) = 0$ is then

$$h(t) = \pm\sqrt{2} \cdot \sqrt{-\frac{B}{A^2} + \frac{B \cdot e^{-A \cdot t}}{A^2} + \frac{B \cdot t}{A}} \qquad (2.109).$$

The solutions of Equations (2.103) and (2.109) are plotted in **Figure 2.16(a)** for two different capillaries. As the capillary diameter becomes smaller, the difference between the two solutions decreases.

The main difference between Equations (1.1) and (1.2) consists in the fact that the initial velocity $\dot{h}(t \rightarrow 0)$ is finite for the Bosanquet-Equation whereas it is infinite for the Lucas-Washburn-Equation. This is also shown in **Figure 2.16(b)**, which is obtained by calculating the derivatives of Equations (2.109) and (2.103). The derivation with regard to the time is

$$\dot{h}(t) = \frac{A}{\sqrt{2 \cdot A \cdot t}} \tag{2.110}$$

for Equation (2.103) and

$$\dot{h}(t) = \frac{A - A \cdot e^{-\frac{t}{B}}}{\sqrt{2}\sqrt{-A \cdot B + A \cdot B \cdot e^{-\frac{t}{B}} + A \cdot t}} \tag{2.111}$$

for Equation (2.109) with the above-defined variables A and B. The limit of the velocity is infinite for the Lucas-Washburn-Equation (2.110) as the time approaches zero. For the Bosanquet-Equation (2.111) the limit is $\sqrt{A/B}$, as derived in section A.4.

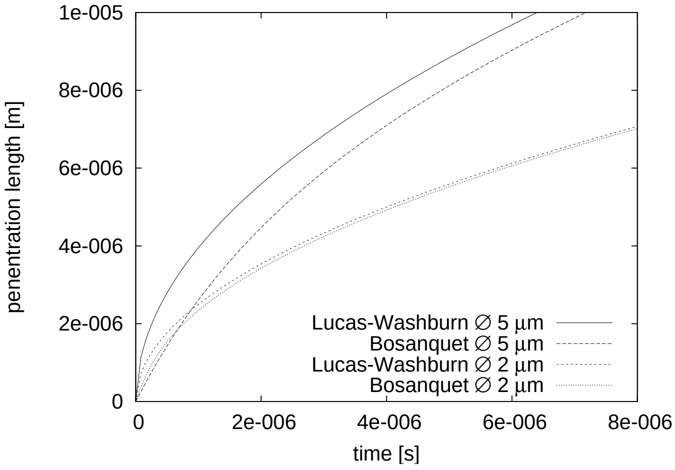

(a) Evaluation of the penetration length calculated with Equations (2.103) and (2.109). Capillaries with smaller diameters reduce the difference between the two solutions.

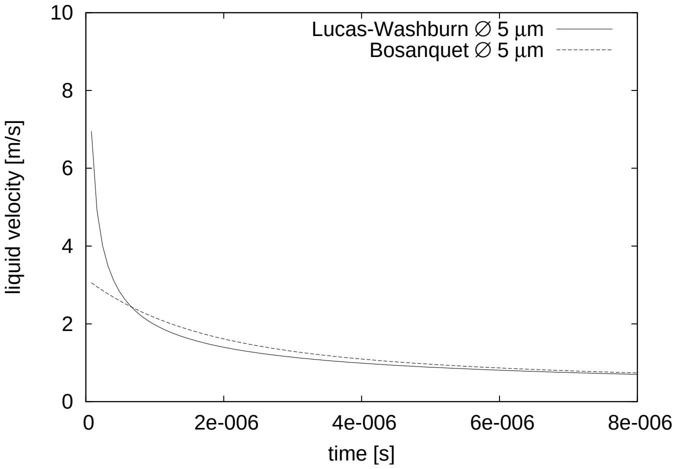

(b) Evaluation of Equations (2.111) and (2.110). The initial velocity of the liquid for the Lucas-Washburn-Equation is infinite. The initial velocity calculated with the help of the Bosanquet-Equation is finite. This is due to the inertia of the liquid, which is taken into account.

Figure 2.16: Plot of the penetration length into a capillary and penetration velocity as a function of time. The capillary diameter is indicated in the legend. The liquid is water with the density $\rho = 10^3$ kg/m^3, the viscosity $\eta = 10^{-3}$ Pa s and the contact angle with the material of the capillary is $\Theta = 80$ °

2.3 Influence of Solubility and Diffusion of gas in water

In section 2.2 liquid penetration into a sealed capillary is described. Due to capillary suction, the pressure in the capillary rises. The equilibrium between air in the gas phase and air dissolved in the liquid changes. This equilibrium can be described for dilute systems with the law found by Henry. The partial pressure p_i of any component i in the air is in an equilibrium with its mole fraction X_i in the water according to the Henry's law constant He_i:

$$p_i = \mathrm{He}_i \cdot x_i \qquad (2.112).$$

The higher the partial pressure of a component, the more of it is dissolved in the liquid. The solubilities of gases in water are tabulated and summarised by Wilhelm et al. [42]. The solubility at a pressure of 1 atm $\approx 10^5$ Pa of nitrogen in water is $x_{N_2} = 0.1695 \cdot 10^{-4}$ mol/mol and for oxygen $x_{O_2} = 0.3459 \cdot 10^{-4}$ mol/mol. This is of importance when describing the penetration of a liquid into a pore. Due to the curved liquid-air interface the pressure is increased. This leads to a changed equilibrium and more gas being dissolved, and hence a higher concentration at the surface of the interface compared to the bulk of the liquid in the pore. Diffusion of the gas into the liquid-bulk will reduce the difference. Diffusion can be described using Fick's 2nd law. The change in concentration c_i with time t depends on the second derivative of the concentration with regard to the distance h and the diffusion coefficient D_i:

$$\frac{\partial c_i}{\partial t} = D_i \cdot \frac{\partial^2 c_i}{\partial h^2} \qquad (2.113).$$

Using Equation (2.113) the situation of a semi-infinite capillary can be described by choosing the start and boundary conditions.

$$\begin{aligned} c_i(h, t=0) &= c_{i,\infty} && (2.114) \\ c_i(h=0, t>0) &= c_{i,0} && (2.115) \\ c_i(h=\infty, t>0) &= c_{i,\infty} && (2.116) \end{aligned}$$

The solution to Equation (2.113) with $\zeta = \frac{h^2}{4 \cdot D_i \cdot t}$ is then

$$c_i(h,t) = c_{i,0} - (c_{i,\infty} - c_{i,0}) \cdot \int_0^{\zeta} e^{-t^2} \, dt \qquad (2.117).$$

The diffusion flux per unit area $j_i = -D \frac{\partial c_i}{\partial t}$ at an arbitrary point h is

$$j_i = \sqrt{\frac{D_i}{\pi \cdot t}} \cdot e^{-\frac{h^2}{4 \cdot D_i \cdot t}} \cdot (c_{i,\infty} - c_{i,0}) \qquad (2.118).$$

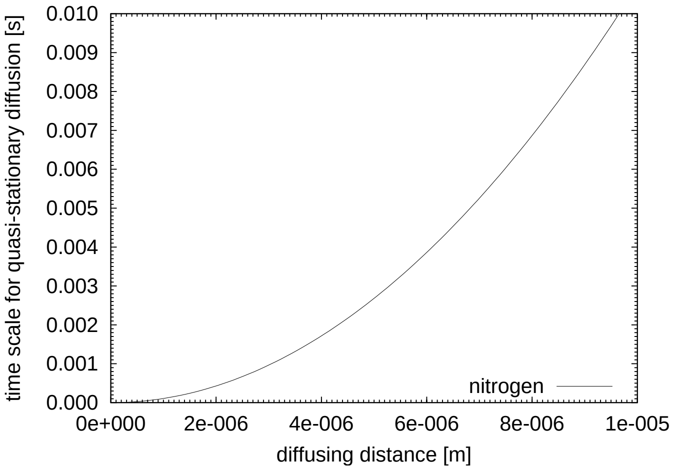

Figure 2.17: Plot of Equation (2.120). For the evaluation the diffusion coefficient of nitrogen is used. For small distances the diffusion can be regarded as quasi-stationary if the time is larger than the time given in the plotted graph.

The dimensionless term

$$\frac{h^2}{4 \cdot D \cdot t} > 1 \tag{2.119}$$

indicates that the diffusion process is starting or

$$\frac{h^2}{4 \cdot D \cdot t} < 1 \tag{2.120}$$

that a quasi-stationary situation has developed. The length of a capillary in the model membrane is of the order of 10^{-5} m. For this dimension Equation (2.120) is evaluated and plotted in **Figure 2.17** using nitrogen as the diffusing component. The time-scale for quasi-stationary diffusion is then in the order of several milliseconds.

The mole flux at the interface is of interest as it can be used to describe the mass transfer from the gas phase into the liquid phase in a capillary. It is obtained from Equation (2.118) by setting h equal to zero:

$$j_i(h=0) = \sqrt{\frac{D_i}{\pi \cdot t}} \cdot (c_{i,\infty} - c_{i,0}) \qquad (2.121).$$

The total amount n of the component i diffused through the cross-section at $h = 0$ is

$$\begin{aligned} n_i(t, h=0) &= \pi \cdot R^2 \cdot \int_0^t j_i(t')\, dt' && (2.122) \\ &= \pi \cdot R^2 \cdot \sqrt{\frac{4 \cdot D_i \cdot t}{\pi}} \cdot (c_{i,\infty} - c_{i,0}) && (2.123) \end{aligned}$$

The total amount diffused from the gas phase into the liquid can be converted into a volume with Boyle's gas law. The volume of gas diffused into the liquid is replaced by the liquid penetrating into the capillary. Together with the cylindrical geometry of the capillary, the penetration depth $h'(t)$ can be calculated:

$$h'(t) = \frac{n(t) \cdot R_g \cdot T}{(P_o + P_L) \cdot \pi \cdot R^2} \qquad (2.124).$$

Substituting h'' for h in Equation (2.113) gives

$$\frac{\partial c_i}{\partial t} = D_i \cdot \frac{\partial^2 c_i}{\partial h''^2} \qquad (2.125).$$

The double prime indicates the coordinate system as introduced in **Figure 2.18** on page 41. The double prime coordinate system has its origin at the gas-liquid interface in the capillary and points to the liquid phase. In the same Figure the situation of a pore partly filled with liquid is shown, the liquid having an interface with air. Assuming a quasi-steady state the left-hand side of Equation (2.125) is zero:

$$0 = D_i \cdot \frac{\partial^2 c_i}{\partial h''^2} \qquad (2.126).$$

At the interface the concentration of the dissolved component is c_0 whilst at the exit of the capillary after a distance H'' the concentration is assumed to be c_∞. The resulting concentration profile is then

$$c_i(h'') = c_0 - \frac{c_0 - c_\infty}{H''} \cdot h'' \qquad (2.127).$$

The resulting mole flux $\dot{n}_i$ also depends on the radius R of the cross-section through which the molecules are diffusing and is

$$\dot{n}_i(h'') = -D_i \cdot \frac{\partial c_i}{\partial h''} \cdot \pi \cdot R^2 \qquad (2.128).$$

With Equation (2.127) one obtains

$$\dot{n}_i(h'') = D_i \cdot \frac{c_0 - c_\infty}{H''} \cdot h'' \cdot \pi \cdot R^2 \qquad (2.129).$$

Now the situation of a pore in a membrane can be evaluated. The pore has a diameter of 5 μm and the radius is R. The penetration depth due to the capillary suction is $H'' = \frac{P_L}{P_0 + P_L} \cdot H$ and the total length of a capillary in the membrane is $H = 10$ μm. The volume V_0 of the gas in the pore before penetration takes place is $V_0 = \pi \cdot R^2 \cdot H$. The number n_i of molecules at the temperature $T = 298$ K in an ideal gas is then $n_i = \frac{P_0 \cdot V_0}{R \cdot T} = 7.925 \cdot 10^{-15}$ mol.

The pressure in the capillary is $P_{h_0} = P_o + P_L$. It can be calculated using the Laplace-Equation:

$$P_L = 2 \cdot \gamma \cos{(\Theta)}/R \tag{2.130}$$

which connects the capillary suction pressure P_L with the contact angle Θ, the radius of the capillary R, and the surface tension γ of the liquid which is penetrating into the capillary. The ambient pressure P_0 has to be added as the capillary is subject to the ambient pressure before penetration takes place, and it is sealed at one side so no gas can escape there:

$$P_{h_0} = P_L + P_0 = \frac{2 \cdot \gamma \cdot \cos{(\Theta)}}{R} + P_0 \qquad (2.131).$$

The concentration in the bulk of the liquid can be calculated with the help of Equation (2.112), assuming a saturated liquid:

$$c_\infty = \frac{n_i}{V_i + V_{H_20}} \approx \frac{n_i}{V_{H_2O}} = x_{\infty,i} \cdot \frac{\rho_{H_2O}}{M_{H_2O}} = \frac{P_0}{\mathrm{He}_i} \cdot \frac{\rho_{H_2O}}{M_{H_2O}} \qquad (2.132).$$

In analogy the concentration c_0 at the interface is

$$c_0 \approx \frac{P_0 + P_L}{\mathrm{He}_i} \cdot \frac{\rho_{H_2O}}{M_{H_2O}} \qquad (2.133).$$

The flux out of the capillary can be calculated with Equation (2.129). The values for the calculation are

- the ambient pressure $P_0 = 10^5$ Pa,
- the radius of the capillary $R = 2.5$ µm,
- the contact angle $\Theta = 85$ °,
- the surface tension $\gamma = 72 \cdot 10^{-3}$ N/m,
- the density of water $\rho_{H_20} = 1000$ kg/m^3,
- the molar mass of water $M_{H_20} = 18$ kg/kmol,
- the Henry constant for Nitrogen $\mathrm{He}_{N_2} = 5.899 \cdot 10^9$ Pa,
- the diffusion coefficient of Nitrogen in water $D_{N_2} = 2.34 \cdot 10^{-9}$ m^2/s,
- the gas constant $R_g = 8.31441$ J/K/mol.

The results are

- the Laplace pressure $P_L = 5 \cdot 10^3$ Pa,
- the pressure in the capillary $P_{h_0} = 1.05 \cdot 10^5$ Pa,
- the concentration of nitrogen in the water at ambient pressure $c_{\infty,N_2} = 9.417 \cdot 10^{-7}$ mol/m^3,
- the concentration of nitrogen at the interface in the capillary $c_{0,N_2} = 1.413 \cdot 10^{-6}$ mol/m^3,

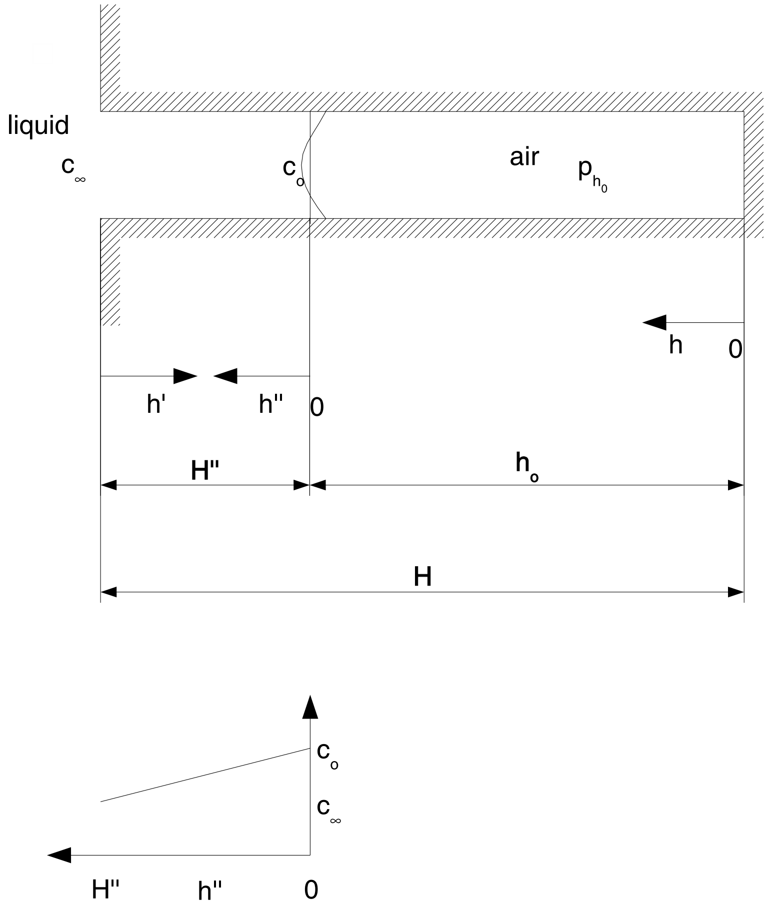

Figure 2.18: Situation of a pore in a membrane. Due to capillary suction liquid penetrates into a capillary. This leads to higher pressure in the capillary. The increased pressure leads to a concentration difference of gas in the liquid phase between the bulk of the liquid and the phase boundary with the gas in the capillary. Due to Henry's law the concentration at the phase boundary is increased. Consequently a flux of gas from the interface into the bulk liquid occurs. In steady conditions the concentration profile between the gas-liquid interface and the exit of the capillary is linear, as shown at the bottom of the plot.

- the molar flux of nitrogen due to the concentration difference over a distance $H = 10\ \mu\mathrm{m}$ being $\dot{n}_{N_2} = 1.102 \cdot 10^{-10}\ \mathrm{mol/s/m^2}$.

This means that in the capillary a flux of gas moves from the gas-liquid interface into the liquid bulk. When the gas in the capillary is dissolved as shown in Figure 2.18 the phase boundary moves. This leads to a slightly different differential equation. The equation for the diffusion due to the concentration difference in the bulk of the liquid and at the gas-liquid interface in the capillary can be described as before using Fick's law. The result is a concentration gradient which is linear for the steady state. In order to obtain the molar flux, Crank [6] introduces a moving coordinate system on the liquid gas interface, as shown in Figure 2.18. According to this coordinate system the mole flux $\dot{n}$ is

$$\dot{n}(h') = -\dot{n}(h'') = D_i \cdot \frac{c_o - c_\infty}{h''} \cdot \pi R^2 \qquad (2.134).$$

Steady state for the mole flux in the liquid phase in the capillary means that the mole flux at the exit of the capillary is the same as the mole flux leaving the gas phase. All changes in the gas are assumed to be isothermal. With Boyle's law the mole flux leaving the gas can be translated into a volume change $\dot{V}$ of the gas phase.

$$\dot{n}(h') = \frac{P \cdot \dot{V}}{R_g \cdot T} = \frac{P \cdot \pi R^2 \cdot \dot{h}}{R_g \cdot T} = \frac{P \cdot \pi R^2 \cdot (H - \dot{h}'(t))}{R_g \cdot T} = -\frac{P \cdot \pi R^2 \cdot \dot{h}'(t)}{R_g \cdot T} \qquad (2.135).$$

The further connection between liquid and gas is Henry's law

$$x_i = \frac{P_i}{\mathrm{He}_i} \qquad (2.136).$$

The mole concentration c_i has to be converted into the mole fraction x_i. This can be achieved with the help of Equation (2.132). The resulting differential equation is of the form

$$\dot{h}' = A \cdot \frac{1}{h'(t)} \qquad (2.137)$$

with the boundary condition $h'(t=0) = H'' = \frac{P_L}{P_L + P_0} \cdot H$, which accounts for the initial compression and penetration by the capillary suction. The variables are

$$\begin{aligned} A &= \frac{D_i \cdot P_L \cdot \rho_{H_2O} \cdot R_g \cdot T}{(P_0 + P_L) \cdot \mathrm{He}_i \cdot M_{H_2O}}, && (2.138) \\ B &= \frac{P_L}{P_L + P_0} \cdot H && (2.139). \end{aligned}$$

A solution to this differential equation is

$$h'(t) = \sqrt{B^2 + 2 \cdot A \cdot t} \qquad (2.140)$$

which it is plotted in **Figure 2.19**.

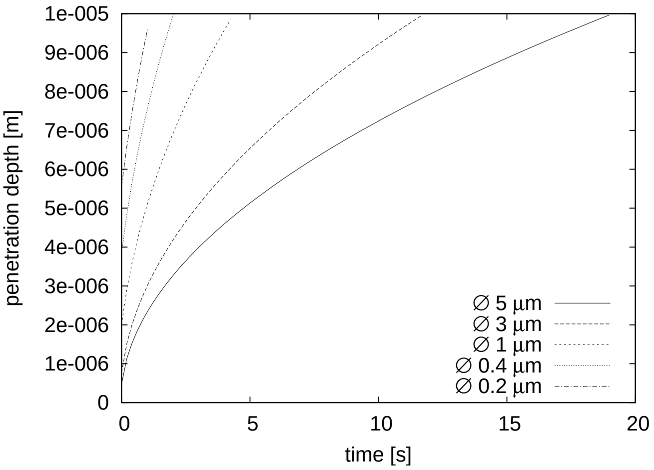

Figure 2.19: Penetration curve of a water into a membrane when the gas phase is pure nitrogen. The length of the capillary is 11 µm and the diameter is indicated in the legend.

2.4 Mutec Penetration Dynamics Analyser

The work of Gabriel [13] is mainly of an experimental nature. Through variation of different parameters the *Mutec Penetration Dynamics Analyser* is evaluated. Four main areas are explored. The measurement set-up, the liquids for the measurement, and the paper properties are varied. The fourth area is a correlation of the results obtained with the *Mutec Penetration Dynamics Analyser* with current measurement methods.

The variation of the set-up includes the frequency, the measurement diameter, the steel insert and the ambient temperature as well as sample preparation. With increasing temperature the intensity detected at the Receiver drops from 100% at 23 °C to 50% at 68 °C. This behaviour is explained by different ultrasonic absorption of water in this temperature range.

The conditioning of the paper and the way it is mounted is investigated. It is found that water penetrating into the sides of the sample has a relevant influence on measurements with board but not with paper.

Different liquids including isopropanol, water, mineral oil, silicon oil, ink-jet inks, and acetone are measured. It is apparent that in particular the measurements with acetone and isopropanol contain dissolved air which degasses during the measurements. Water is evaluated also in terms of pH-value and ion concentration. Measurements of cellulose paper in water with increasing concentration of sodium chloride show a retarded decrease in transmitted intensity compared to water. It is suggested that these differences are due to a reduction in vapour pressure with increased concentrations of sodium chloride. The penetration of the vapour phase into the paper is slowed down and the detected signal changes accordingly.

The paper properties sizing, pore-size, calendering level and filling level are varied. The influence of refining, density, roughness, air permeability, water retention and wet expansion are also evaluated.

Gabriel's thesis is of lesser importance for this work as it is mainly a collection of data for measurements with the *Mutec Penetration Dynamics Analyser*. However, apart from the manual, it is the only published work at hand.

3 Model for the Mutec Penetration Dynamics Analyser

In general only measurements using physical properties are of scientific value and a model should be based on physical grounds. For the formulation of a model three basic rules can be set up according to Kanzamár [18]:

- The measurement result has to be a physical property, in this case the attenuation of ultrasound or intensity of ultrasound.
- The processes taking place during a measurement have to be modelled using physical relationships.
- Each part of the model has to be verified.

The first rule poses some difficulty for measurements with the *Mutec Penetration Dynamics Analyser*, as its implementation does not directly deliver a physical property. This is why some effort has to be made concerning the development of a model for the sound generation and attenuation within the device.

A structure for the model can be given in accordance to the rules: firstly the generation and detection of ultrasound at the Sender and the Receiver using piezoelectric ceramics; secondly the physical processes taking place between Sender and Receiver have to be defined. These processes depend upon the set-up of the *Mutec Penetration Dynamics Analyser* and can be divided into different parts:

- The geometry of the device as well as the size of the Sender and Receiver and the wavelength of ultrasound used;
- Losses of ultrasound in the medium between Sender and Receiver;
- Transmission of ultrasound through the sample-holder;
- Transmission of ultrasound through the steel insert;
- Influence of a model-sample onto the ultrasound.

Finally the applicability of the model to measurements with paper is investigated.

3.1 General description of the Mutec Penetration Dynamics Analyser

Before a model is developed which takes the different aspects of the *Mutec Penetration Dynamics Analyser* into account, the geometry, the general functioning, and the technical background of the *Mutec Penetration Dynamics Analyser* have to be described, as far as they are known. In addition appropriate assumptions for the unknown parts of the device have to be made.

3.1.1 Geometry of the Mutec Penetration Dynamics Analyser

The *Mutec Penetration Dynamics Analyser*, referred to simply as Mutec, is controlled by a separate control box which stores and transmits the data to a computer with a software program which allows parameters to be set.

A sketch of the Mutec device is shown in **Figure 3.1(a)**. It consists of a sample chamber (1), on one side of which there is the piezoelectric ultrasonic Sender (2), on the opposite side the ultrasonic Receiver (3). The sample chamber is filled with water up to a level where the Sender and Receiver are fully covered with water. A steel insert (4) with two plastic windows (5) can be used for test-liquids different from water. The sample (8) is attached to the sample-holder (6) with two-sided sticky tape (7). The sample-holder is then connected to the stepper motor (9), which pushes the sample into the test-liquid within a certain time.

A detailed sketch of the measurement chamber is shown in **Figure 3.1(b)**. The measurement chamber consists of a metal block containing Sender and Receiver. There are two sets of Sender and Receiver, for a measurement frequency of 1 MHz and 2 MHz respectively. Each Sender and Receiver has the two concentric measurement areas of 0.035 m diameter and 0.01 m diameter. The steel insert, as well as the sample-holder, is not parallel to the Sender and Receiver but at an angle of about 9.5^o. The steel insert has two plastic windows to allow ultrasound to be transmitted.

3.1.2 Functioning of the Mutec Penetration Dynamics Analyser

In order to calibrate the instrument the attenuation of the ultrasonic intensity must be determined. Based on this calibration measurement, a cell

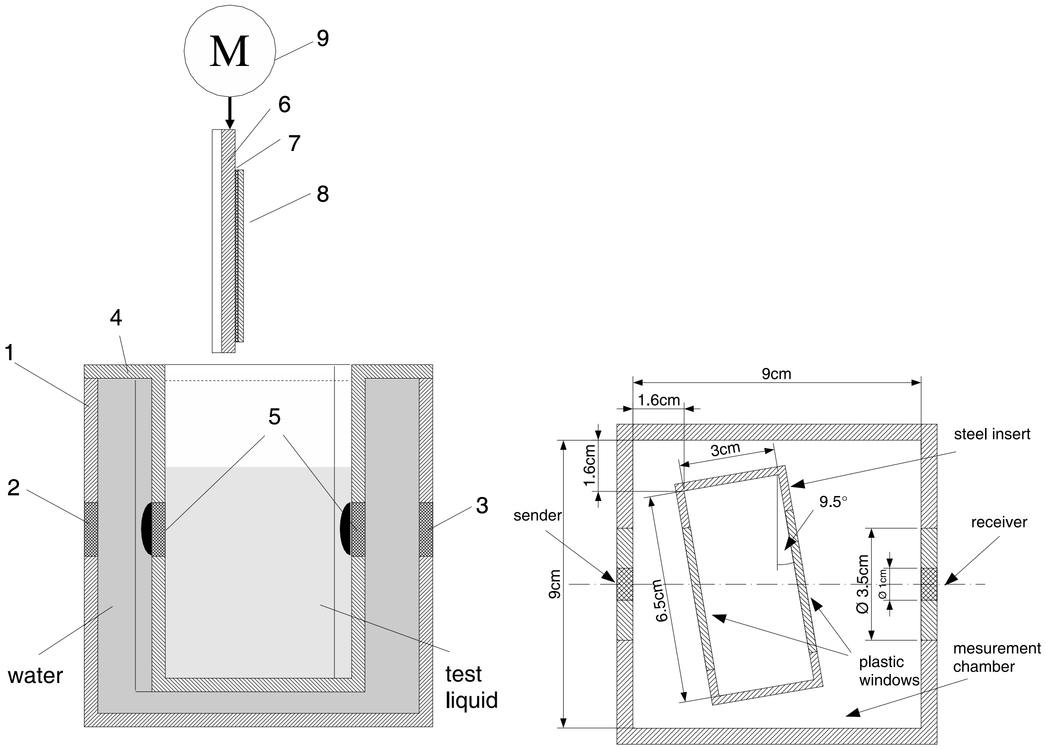

(a) Diagram of the Mutec device (b) Sketch of the measurement chamber

Figure 3.1: The Mutec measurement set-up: measurement chamber (1) filled with water, ultrasonic Sender (2), ultrasonic Receiver (3), the steel insert (4) filled with the test-liquid, two plastic windows (5) for transmission of ultrasound, the sample-holder (6), two-sided sticky tape (7), paper sample (8), and the stepper motor (9). the Sender (2) and Receiver (3) have a large (0.035 m) and a small (0.01 m) measurement area. The steel insert (4) and the sample-holder (6) are tilted.

constant is calculated. The cell constant allows results to be given as a pseudo-attenuation value $\alpha(t)$. By setting the input voltage of the Sender and the amplification of the Receiver to the values used during the calibration, similar measuring conditions are created and a direct comparison of the results, in terms of pseudo-attenuation values (α_{Mutec}), is possible. The manufacturer of the device points out that this is not an absolute value of the attenuation, as all the measurements are still relative measurements. If the device is used to measure a sample attached to the sample-holder, the initial calibration must be done using the sample-holder and the two-sided sticky tape.

There are two ways of using the Mutec. The first is an automated measurement and the second a diagnostic mode, which allows direct control of parameters.

The automated method works as follows. To undertake a measurement, the parameters are set in the computer software. These parameters contain the duration of the measurement, the Transducer selected, the level of the liquid in the measurement device, and a sample identification. The parameters are transmitted to the control box which adjusts the input voltage of the Sender and the amplification of the Receiver according to the liquid in the sample chamber. The detected intensity at the Receiver is subsequently controlled to remain in a certain range. A measurement is started by pressing the release button and the sample-holder is pushed into the test-liquid. If the initial values of ultrasound intensity detected at the Receiver are too small or too large, the amplification or the input voltage is automatically adjusted. The attenuation of ultrasound between Sender and Receiver is measured and the first value is available after 8 ms if the smaller measurement area is selected and 31 ms if it is the larger measurement area. The change of the intensity of ultrasound measured at the Receiver is monitored and displayed online. When the measurement is finished, the data are transmitted from the control box to the computer and the attenuation of ultrasound as a function of time is calculated. The attenuation is always normalized, based on either the first value, the maximum, or the last value.

In the diagnostic mode the internal parameters such as the input voltage or the amplification are displayed. It is also possible to adjust these parameters and to force the Mutec device to use these values. If the diagnostic mode is used, the measurement is displayed as an intensity change with time.

3.1.3 Operation of the Mutec Penetration Dynamics Analyser

To perform a measurement, the measurement chamber is filled with water which has been treated in an ultrasonic bath to remove any dissolved gases. The liquid level is adjusted so that the Sender and Receiver are covered with water. The sample-holder is prepared by fixing a sample onto the sample-holder. Measurement parameters such as Transducer diameter, measurement time, and liquid level in the measurement chamber are set in the software. The measurement is started by pressing the release button which is located on the device. The sample-holder is then pushed into the liquid at constant speed. As soon as the sample-holder is in measurement position, the ultrasonic attenuation is measured and recorded. When the measurement is finished, the sample-holder is moved into its starting position by pressing the release button again. The measurement data are then transferred to the computer and saved.

The speed of the immersion of the sample-holder into the liquid is constant. Consequently the time for the exposition of the sample to the liquid in the measurement chamber before a first value is recorded depends on the level of liquid in the measurement chamber. Since the Transducer with the smaller diameter allows lower levels of liquid in the measurement chamber, the first measurement value is already available after 8 ms. For the larger diameter the first value is recorded after 31 ms.

3.1.4 Technical details for the Mutec Penetration Dynamics Analyser

According to the manufacturer, the ultrasonic wave has a frequency f of 1 MHz or 2 MHz. The length of the initial pulse in the Sender is approximately 1 µs, and the applied voltage is up to 70 kV. At the Receiver the ultrasonic pulse builds up over 7 oscillations and declines over 7 oscillations [16]. According to Krautkrämer and Krautkrämer [19], no difference with regard to the interference between a pulse and a continuous wave is seen in practice if more than about 6 oscillations are in the pulse.

The maximum intensity generated in the Sender is $I_{\text{max, Sender}} = 10\ \text{W/m}^2$ [17]. Assuming the liquid in the Mutec to be water with an acoustic impedance of $Z_2 = 1.5 \cdot 10^6\ \text{kg/s/m}^2$, its intensity has a maximum pressure in the Sender of

$$\begin{aligned} P_{\text{max, Sender}} &= \sqrt{2 \cdot Z_{\text{Sender}} \cdot I_{\text{max, Sender}}} \\ &= 2.5 \cdot 10^4\ \text{Pa.} \end{aligned} \tag{3.1}$$

With the appropriate equation for the transmission coefficient for acoustic intensity T_i from Table 2.2 and using $\theta = 0$, the maximum acoustic pressure transmitted into the liquid in the Mutec is

$$\begin{aligned} P_{\text{max, liquid}} &= T_\text{p} \cdot P_{\text{max, Sender}} \\ &= 2.3 \cdot 10^3\ \text{Pa.} \end{aligned} \tag{3.2}$$

As has been pointed out in Equation (2.17) on page 13, the maximum pressure in the sound-field is twice as great as on the surface of the emitter. With this information the absolute minimum pressure p in the liquid can be calculated:

$$\begin{aligned} p &= p_0 - 2 \cdot P_{\text{max, liquid}} \\ &\approx 10^5 \text{ Pa} - 2 \cdot 2.3 \cdot 10^3 \text{ Pa} = 0.954 \cdot 10^5 \text{ Pa}. \end{aligned} \tag{3.3}$$

This eliminates the possibility of cavitation in the liquid. It emphasizes the need to degas the liquid, as degassing already occurs at much smaller pressure differences than those needed for cavitation. As bubbles in the measurement chamber of the *Mutec Penetration Dynamics Analyser* ruin the measurement, the liquids used for the measurements have to be degassed in an ultrasonic bath. This also means that, in this model, the assumption of Miller and Nyborg [27], namely equilibrium conditions at the gas-liquid interface in a capillary, cannot be applied to the *Mutec Penetration Dynamics Analyser* . However the Mutec only uses the maximum intensity of the ultrasound in highly attenuating media, and cavitation is not observed or measured during measurements with water.

3.2 Model for measurements of liquids

The model for measurements of liquids consists of three parts:

- the generation of the ultrasonic pulse in the Sender and its detection in the Receiver depending on the material properties of Sender and Receiver as well as their geometry and the liquid in the measurement chamber;
- the geometric spread of the sound-field in the measurement chamber as a function of the geometry of the Sender and the medium in the measurement chamber;
- the attenuation of sound in the measurement chamber depending on the material properties of the medium in the measurement chamber.

In the following sections these parts will be described.

3.2.1 Model for the pulse generation of a circular piston transducer

The transducer in the Mutec is made from a piezoelectric ceramic. A piezoelectric ceramic converts an applied voltage into a volume change in the ceramic.

It is assumed that the ceramic behaves similarly to the commonly used barium titanate ($BaTiO_3$), but no details are available from Mutec. Barium titanate has a density of 5850 kg/m^3, and the speed of sound within the ceramic is 5200 m/s. The resulting acoustic impedance is

$$\begin{aligned} Z_{\text{Sender}} &= 5850\ \text{kg/m}^3 \cdot 5200\ \text{m/s} \\ &= 30.42 \cdot 10^6\ \text{kg/m}^2/\text{s}. \end{aligned}$$

Its piezoelectric modulus is [19]

$$d_{33} = 125 \cdot 10^{-12}\ \text{m/V} \qquad (3.4).$$

The change of volume caused by an electric voltage U_{Sender} is a material property of the piezoelectric ceramic. The thickness change Δx of barium titanate is a function of the piezoelectric modulus d_{33}:

$$\Delta x = d_{33} \cdot U_{\text{Sender}} \qquad (3.5).$$

The Mutec uses up to 70 kV. For barium titanate this leads to an approximated thickness change in the ceramic of

$$\Delta x = 125 \cdot 10^{-12} \cdot 70 = 8.75 \cdot 10^{-6}\ \text{m} \qquad (3.6)$$

for the first cycle. In the subsequent cycles the thickness change is reduced. The voltage is applied during a short period of time $\Delta t = 1\ \mu\text{s}$. The maximum velocity of the surface of the ceramic can be approximated by

$$v_{\text{max, 1}} \approx \frac{\Delta x}{\Delta t} = \frac{8.75 \cdot 10^{-6}\ \text{m}}{1 \cdot 10^{-6}\ \text{s}} = 8.75\ \text{m/s} \qquad (3.7).$$

The maximum pressure inside the ceramic as a function of its density ρ is then

$$P_{\text{max, Sender}} = \rho \cdot \frac{\Delta x}{\Delta t} \approx 50000\ \text{Pa} \qquad (3.8).$$

Converting the maximum pressure $P_{\text{max, Sender}}$ into intensity $I_{\text{max, Sender}}$ gives

$$I_{\text{max, Sender}} = \frac{P_{\text{max}}^2}{2 \cdot \rho \cdot c} \approx \frac{50000\ \text{Pa}}{2 \cdot 5850\ \text{kg/m}^3 \cdot 5200\ \text{m/s}} \approx 42\ \text{W/m}^2 \qquad (3.9).$$

The intensity which crosses the phase boundary between Sender and medium, in this case water, is

$$I_{\text{max, medium}} = T_{\text{I,(T/M)}} \cdot I_{\text{max, Sender}} \approx 0.18 \cdot 42\ \text{W/m}^2 = 7.56\ \text{W/m}^2 \quad (3.10).$$

This value is of the same order as given by the supplier of the device. The difference is probably due to slight differences in material properties as well as non-linearities in the process.

The conversion of intensity into pressure gives

$$P_{\text{max, medium}} = \sqrt{2 \cdot Z_{\text{medium}} \cdot I_{\text{max, medium}}} \approx 4760\ \text{Pa} \qquad (3.11).$$

The maximum pressure $P_{\text{max, medium}}$ in the medium is below the evaporation pressure of the liquids used. This means that cavitation will not occur. However $P_{\text{max, medium}}$ is strong enough to degas dissolved air from certain liquids. This became obvious during some measurement but degassing the liquid with the help of an ultrasonic bath overcomes this problem.

The generation of a pulse as described in section 2.1.1 is now applied to the Mutec. If an electric pulse is applied across the surface of the ceramic, a volume change/ pressure pulse is originated at the two surfaces. These pulses start to travel through the ceramic and the surrounding medium. The fraction of the pulse travelling through the ceramic with regard to the medium is dependent upon the impedance Z of the ceramic and the surrounding medium.

It is assumed that the ultrasonic transducer has one surface in air (see Figure 2.4), and the entire impulse at this side of the transducer is reflected. This is shown in Figure 2.4, where $Z_{\text{air}} = 0.44 \cdot 10^6\ \text{kg/m}^2\text{/s} \ll Z_{\text{Sender}} = 30.42 \cdot 10^6\ \text{kg/m}^2\text{/s}$.

Equations (2.12), (2.13) and (2.14) can be developed to describe the pulse generation in the Mutec. The variable $S(i)$ is the energy stored in the Receiver in the cycle i. In each cycle a part of the stored pulse leaves the Receiver and a part $I(i)$ enters from the sound-field.

$$\begin{aligned}
S(0) &= I(0) \\
S(1) &= R_{\text{P, R/M}} \cdot S(0) + I(1) = R_{\text{P, R/M}} \cdot I(0) + I(1) \\
S(2) &= R_{\text{P, R/M}} \cdot S(1) + I(2) = R^2_{\text{P, R/M}} \cdot I(0) + R_{\text{P, R/M}} \cdot I(1) + I(2) \\
&\;\;... \\
S(i) &= R_{\text{P, R/M}} \cdot S(i-1) + I(i) \\
&= R^i_{\text{P, R/M}} \cdot I(0) + R^{i-1}_{\text{P, R/M}} \cdot I(1) + R^{i-2}_{\text{P, R/M}} \cdot I(2) + ... \qquad (3.12) \\
&\quad ... + R_{\text{P, R/M}} \cdot I(i-1) + I(i)
\end{aligned}$$

Inserting Equation (2.12) into Equation (3.12) gives

$$\begin{aligned}
S(i) = \;& R^i_{\text{P, R/M}} \cdot k \cdot R^0_{\text{P, S/M}} + R^{i-1}_{\text{P, R/M}} \cdot k \cdot R^1_{\text{P, S/M}} + \qquad (3.13) \\
& + R^{i-2}_{\text{P, R/M}} \cdot k \cdot R^2_{\text{P, S/M}} + ... + R_{\text{P, R/M}} \cdot k \cdot R^{i-1}_{\text{P, S/M}} + \cdot k \cdot R^i_{\text{P, S/M}} \cdot
\end{aligned}$$

This is the sum of a geometric series and can be solved to give an explicit solution

$$S(i) = k \cdot \frac{R^{i+1}_{\text{P, S/M}} - R^{i+1}_{\text{P, R/M}}}{R_{\text{P, S/M}} - R_{\text{P, R/M}}} \qquad (3.14).$$

Equation (3.14) is still discrete. Formally introducing a continuous variable x gives

$$S(x) = k \cdot \frac{R_{\mathrm{P,\ S/M}}^{x+1} - R_{\mathrm{P,\ R/M}}^{x+1}}{R_{\mathrm{P,\ S/M}} - R_{\mathrm{P,\ R/M}}} \tag{3.15}$$

and enables the calculation of the maximum of $S(x)$. This is of interest as the *Mutec Penetration Dynamics Analyser* only records the maximum of the detected pulse. If the reflection coefficient R for the pressure (index P) between Sender (index S) and the medium (index M) is different from the reflection coefficient of the Receiver (index R), $R_{\mathrm{P\ ,S/M}} \neq R_{\mathrm{P,\ R/M}}$, the maximum is

$$S(x_{max}) = \frac{k}{R_{\mathrm{P,\ S/M}} - R_{\mathrm{P,\ R/M}}} \cdot \left(R_{\mathrm{P,\ S/M}}^{\frac{\ln\left(\frac{\ln(R_{\mathrm{P,\ R/M}})}{\ln(R_{\mathrm{P,\ S/M}})}\right)}{\ln\left(\frac{R_{\mathrm{P,\ S/M}}}{R_{\mathrm{P,\ R/M}}}\right)}} - R_{\mathrm{P,\ R/M}}^{\frac{\ln\left(\frac{\ln(R_{\mathrm{P,\ R/M}})}{\ln(R_{\mathrm{P,\ S/M}})}\right)}{\ln\left(\frac{R_{\mathrm{P,\ S/M}}}{R_{\mathrm{P,\ R/M}}}\right)}} \right) \quad (3.16).$$

If the reflection coefficients in Sender and Receiver are equal – $R_{\mathrm{P,\ S/M}} = R_{\mathrm{P,\ R/M}} =: R_{\mathrm{P,\ T/M}}$ – one obtains:

$$S(x_{max}) = k \cdot R_{\mathrm{P,\ T/M}}^{-\frac{1}{\ln(R_{\mathrm{P,\ T/M}})}} \cdot \left(\frac{1}{\ln(R_{\mathrm{P,\ T/M}})} \right) \quad (3.17).$$

Equations (3.16) and (3.17) are time-independent. They only depend on the material properties of the ceramic used in the Sender and Receiver and the properties of the medium between Sender and Receiver. This is assumed to be the case of the *Mutec Penetration Dynamics Analyser*, as is indicated by the supplier of the device.

In Equations (2.12), (3.12), (2.13) and (2.14) i is replaced by a continuous variable. The resulting graphs are plotted in **Figure 3.2**.

The frequency f of the generated pulse relates to the thickness h_{Sender} of the ceramic and the velocity of sound c in the ceramic. The thickness of the ceramic is just half a wavelength λ, so pulses will be emitted with a separation distance of 1 wavelength. Equation (2.10) gives a thickness of

$$h_{Sender} = \frac{\lambda}{2} = \frac{c}{2 \cdot f} = \frac{5200\ \mathrm{m/s}}{2 \cdot 1\ \mathrm{MHz}} = 2.6\ \mathrm{mm} \tag{3.18}$$

and

$$h_{Sender} = \frac{5200\ \mathrm{m/s}}{2 \cdot 2\ \mathrm{MHz}} = 1.3\ \mathrm{mm} \tag{3.19}$$

for the 1 MHz-Sender, made from barium titanate, and the 2 MHz-Sender respectively. The geometry of the ultrasonic transducer is shown in **Figure 3.3**.

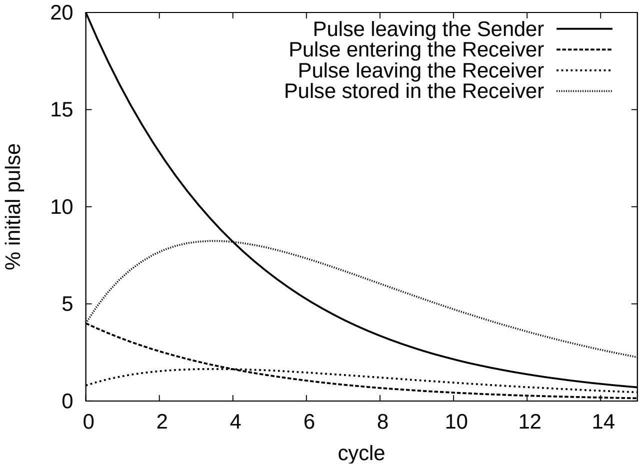

Figure 3.2: Illustration of the dynamics of the pulse generation in the Mutec. The dynamics of the pulse generation is calculated with the help of Equation (2.11) for the part of the pulse which leaves the Sender, Equation (2.12) for the part which enters the Receiver, Equation (2.13) for the part which leaves the Receiver and Equation (3.12) for the strength of the pulse stored in the Receiver. With each oscillation the pulse leaving the Sender is reduced and consequently the pulse entering the Receiver is reduced as well. This leads to a build-up of the energy stored in the Receiver. The pulse leaving the Receiver increases with the pulse stored in the Receiver. Consequently the part of the signal leaving the Receiver increases up to the point where the pulse entering the Receiver is smaller than the part of the pulse leaving the Receiver. Then the pulse in the Receiver decreases again. The result is a curve which goes through a maximum before declining again. The values for the calculation are $R_{\text{P, S/M}} = R_{\text{P, R/M}} = 0.8$ and $T_{\text{P, S/M}} = T_{\text{P, M/S}} = T_{\text{P, R/M}} = 0.2$.

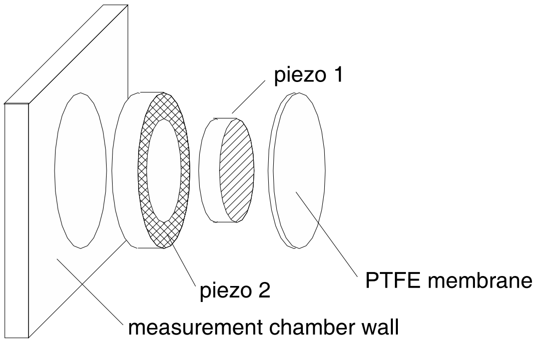

Figure 3.3: Exploded drawing of the ultrasonic Sender: two concentric piezoelectric ceramics are mounted in the wall of the measurement chamber. They are covered by a PTFE membrane with a thickness of 0.1 mm. The diameter of the smaller piezo 1 is roughly 10 mm and the diameter of the larger piezo 2 is approximately 35 mm.

It is mounted in the wall of the measurement chamber and protected from the medium in the chamber by a thin PTFE film. The PTFE film is bonded to the ceramic, and it can be assumed that the ceramic is connected to the membrane over the entire surface. The transducer will therefore behave as a circular piston Sender.

As the PTFE film is connected to the Sender, a transversal wave can be transmitted. The liquid in the measurement chamber will not transmit a transverse wave but only a longitudinal wave.

The construction of the Sender and the Receiver is basically the same with the difference at the Receiver being a pressure pulse converted into an electrical pulse which is amplified and may be displayed. The maximum value stored in the Receiver will be recorded. As information about the amplification method and possible nonlinearities is not available, the model for the Receiver cannot be adapted further.

The coupling constant for the Sender-Receiver set-up can be calculated with the help of Equation (2.9). For barium titanate $BaTiO_3$ it is

$$\frac{U_{\text{Receiver}}}{U_{\text{Sender}}} = k_{33}^2 = d_{33} \cdot h_{33} = 0.19 \qquad (3.20).$$

The coupling constant for a thin plate made from barium titanate is

$$k_t^2 = 0.11 \qquad (3.21).$$

This value coincides with the value of the efficiency of the Sender/Receiver given by the supplier.

3.2.2 Sound-field in the Mutec Penetration Dynamics Analyser

A simplified model for the distribution of the sound-field in the Mutec can be obtained using Huygens's principle of superimposing point sources. The geometry of the Sender and the observer at an arbitrary position $\vec{r_o}$ on the surface of the Receiver is shown in **Figure 3.4**. the Sender itself is modelled using Huygens's principle of superimposing point sources. For this model, these point sources are just on the surface of the Sender within the medium. The strength of the point sources can be calculated with the help of Equation (3.7) and the transmission coefficient $T_{\dot{\xi},\,1/2}$ from Table 2.2. As the Mutec varies the pulse strength according to the attenuation in the measurement chamber without displaying the value, it is impossible to determine the maximum velocity $v_{\max}$ of the Sender surface.

An intensity distribution supplied by the manufacturer and based on a continuous wave shows a variation of the beam within the measurement

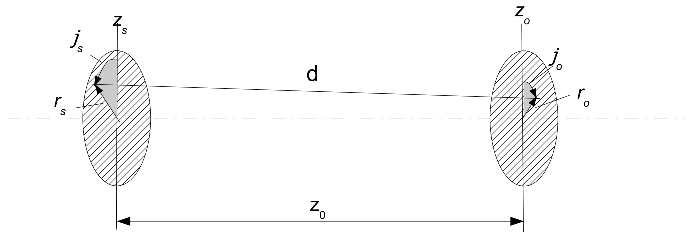

Figure 3.4: Geometry of a source/Sender and an observer/Receiver in cylindrical coordinates with the radius r, the angle φ and the distance along the centre-line z. The index s stands for an element on the Sender and the index o for an observer at an arbitrary position. In this particular case the observer's position is on the Receiver.

chamber of about 10 % [29]. Sutilov [40, pp. 203] states that in a set-up of Sender and Receiver with the same radiation/ detecting area the local pressure varies $10 - 15$ % from the ideal plane wave.

the Sender emits ultrasound on the entire surface S. The consequent pressure at an arbitrary point can therefore be calculated with Equation (2.15). The distance d between a point of the Sender $\vec{r_s}$ and an observer at $\vec{r_o}$ with

$$\vec{r_s} = \begin{pmatrix} r_s \\ \varphi_s \\ z_s \end{pmatrix} \quad \text{and} \quad \vec{r_o} = \begin{pmatrix} r_o \\ \varphi_o \\ z_o \end{pmatrix} \tag{3.22}$$

is

$$d = \sqrt{r_o^2 + r_s^2 + z_o^2 - 2 \cdot z_o \cdot z_s + z_s^2 - 2 \cdot r_o \cdot r_s \cdot \cos\left(\varphi_o - \varphi_s\right)} \qquad (3.23).$$

The variables are also pointed out in Figure 3.4. The earlier introduced Equation (2.15) describing the pressure distribution in the Mutec is taken up again:

$$p(d) = \frac{i \cdot \omega \cdot \rho}{2 \cdot \pi} \cdot e^{\frac{i \cdot \omega \cdot t}{2 \cdot \pi}} \cdot \int\limits_s v_{\max}(t) \cdot \frac{e^{-ik \cdot d}}{d} ds \qquad (3.24).$$

The maximum velocity $v_{\max}(t)$ has to be adapted for the situation in the Mutec. The ultrasound used in the Mutec is pulsed. This means that the maximum velocity $v_{\max}(t)$ of the pulsating surface is time-dependent. The time depending behaviour of $v_{\max}(t)$ can be described using Equation (2.11). The discrete value of the cycle i in Equation (2.11) is substituted by $i = \frac{\omega \cdot (t-d/c)}{2 \cdot \pi}$ to calculate the pressure at any point in time and space:

$$v_{\max}(t) = T_{\mathrm{P,\ T/M}} \cdot R_{\mathrm{P,\ T/M}}^{\frac{\omega \cdot (t-d/c)}{2 \cdot \pi}} \cdot \hat{p} \qquad (3.25).$$

The reflection coefficient $R_{\mathrm{P,\ T/M}}$ can be calculated with the equations found in Table 2.2. The pressure pulse is applied at time zero, having limited speed c of spreading. After the time t, the pulse has travelled the distance d. Beyond this distance the pressure pulse has no influence and the value is therefore zero. Within the distance d the influence of the pressure pulse can be described using Equation (2.15). Equation (2.15) has to be modified by these conditions to give:

$$p(d) = \begin{cases} \frac{i\cdot\omega\cdot\rho}{2\cdot\pi} \cdot e^{\frac{i\cdot\omega\cdot t}{2\cdot\pi}} \cdot \int\limits_S v_{\max}(t) \cdot \frac{e^{-ik\cdot d}}{d} dS & \text{if} \quad t > 0 \wedge d < c \cdot t \\ 0 & \text{else} \end{cases} \qquad (3.26).$$

Equation (3.26) can be divided into a time-dependent term and a second term depending on the position which describes the diffraction. The diffractive part of Equation (3.26) is plotted in **Figure 3.5(a)** and **Figure 3.5(b)** for two different times. The dimensions are taken from the Mutec: radius of the Sender 0.005 m and distance between Sender and Receiver 0.09 m. Evaluating Equation (3.26) for different diameters of the Sender shows that the sound-field in the Mutec only reaches far-field conditions for the smaller diameter of 0.01 m as is seen in Figures 3.5(a) and 3.5(b). the Sender with the larger diameter generates a sound-field which, within the dimensions of the Mutec, is still in the near-field. Therefore all the following measurements and evaluations will be done using the Sender with 0.01 m diameter. A stable sound-field without diffraction develops within the first 0.03 m. This is well before the sound beam encounters the sample-holder, which is at a distance of 0.045 m from the Sender surface.

The time t required by the sound-field to develop fully, i.e. when all wavelets on the Sender interfere with each other on the surface of the Receiver, depends upon the size of the Sender and Receiver, their distance $z = z_s - z_o$ and the speed of sound c. The distance between two wavelets at opposite points on the circumference of the Sender is the Sender's diameter D. In order to interfere at a point perpendicular to the first wavelet on the surface of the Receiver, the wave generated at the second wavelet has to travel a longer distance $\sqrt{D^2 + z^2}$. The time difference between the arrival of the first wave at the Receiver at a point perpendicular to its origin and the second wave reaching the same point is then:

$$t = \sqrt{\frac{D^2 + z^2}{c^2}} - \frac{z}{c} = 0.37\ \mu\text{s} \qquad (3.27).$$

This means, once the first wave front generated at the Sender arrives at the Receiver, it will take an additional 0.37 µs for the sound-field to develop fully on the entire surface of the Receiver. This is less than one cycle of the ultrasound if the frequency is 1 MHz.

From a numeric point of view the initial time of 0.37 µs means additional evaluations. The integration has to be split up into various smaller sections

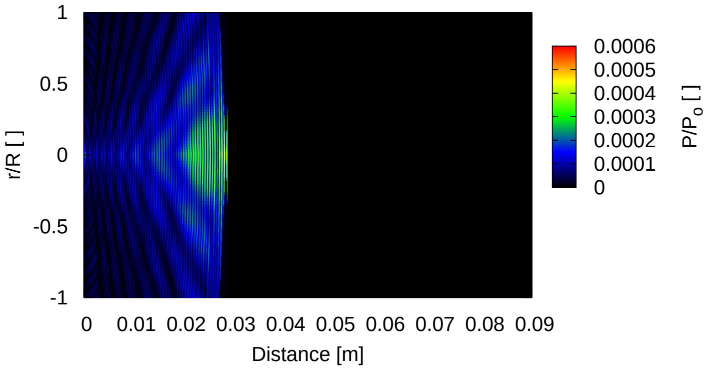

(a) Sound-field in front of the Sender in the Mutec at $t = 2 \cdot 10^{-5}$ s. It can be seen that at short distances behind the Sender interference phenomena occur. These are present up to a distance of about $2-3$ cm from the Sender. After this distance the pressure field only contains one local extremum. By the time the pulse reaches the sample-holder at a distance of 4.5 cm from the Sender, the field is developed fully, hence the incident beam can be described using geometric methods.

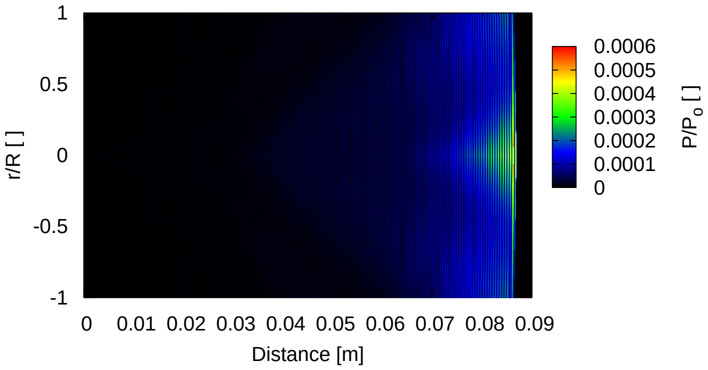

(b) Sound-field in front of the Sender in the Mutec at $t = 6 \cdot 10^{-5}$ s. The front of the pulse has reached about 8.5 cm and at this distance the pressure field contains one local extremum.

Figure 3.5: Evaluation of Equation (3.26). The values for the evaluation are: frequency $f = 1$ MHz, time of observation after generation of pulse $t = 2 \cdot 10^{-5}$ s, Radius of Sender and Receiver $R = 10$ mm, speed of sound in the Sender and Receiver $c_t = 5200$ m/s, density of the Sender and Receiver $\rho_T = 5850$ kg/m^3. The liquid in the measurement chamber is water with a speed of sound $c_m = 1450$ m/s and the density $\rho_m = 1000$ kg/m^3.

in order to account for regions on the Receiver's surface where only a part of the Sender area interferes. In the two-dimensional case, when only the pressure in one point has to be determined, this means changing the integration boundaries, as shown in **Figure 3.6**. The circle with the diameter R in Figure 3.6 (a)-(e) specifies the area of the Receiver. The variables r_o and φ_o define a position of an observer. In Figure 3.6 (a) and (b) the coloured circles describe an area on the Sender which has an influence on the detected pressure at (r_o, φ_o) on the Receiver's surface. The radius is in direct relation to the time after the generation of the pulse. The larger the radius, the longer the time since the generation of the pulse. Depending on the position of the observer and the time, the area of the Sender generating the pressure detected at the observer varies. The time after the generation of the pressure pulse defines the radius r_c. r_c can be calculated as a function of the speed of sound c and the distance between Sender and observer $z_o - z_s$:

$$r_c = \sqrt{(c \cdot t)^2 - (z_o - z_s)^2} \qquad (3.28).$$

In Figure 3.6 (b) - (d) r_c is constant. If for the same time an observer is located at different positions, the radial position, for example, increases, the circle describing the Receiver and the circle described by Equation (3.28) intersect. In order to calculate the pressure at the observer in case (b) one integral, in case (c) two integrals and in case (d) three integrals have to be evaluated. Once the time has exceeded a certain value, only one integral has to be evaluated (e). For the evaluation of the pressure over the entire Receiver area the pressure distribution at the Receiver's surface has to be calculated by means of an integration. As a two-dimensional integration of a two-dimensional integral has to be calculated, the number of sections and numerical integrals to be evaluated becomes very extensive, as is shown in Figures A.1, A.2 and A.3 in appendix A.5.

The model for measurements of a medium in the measurement chamber is based on the following assumptions for Sender, Receiver and the sound-field.

- The dynamics of Sender and Receiver are described in section 3.2.1. As Sender and Receiver have the same physical and geometrical properties and the medium in the measurement chamber is in contact with Sender and Receiver, Equation (3.17) is used to describe the dynamics of Sender and Receiver.
- For measurements with liquids similar to water and the Sender and Receiver with 1 cm diameter, far-field conditions are applicable in the *Mutec Penetration Dynamics Analyser*.
- The geometric spread is approximated by Equations (2.17), (2.22) and (2.23).
- The dissipation of ultrasound is taken into account by the appropriate attenuation coefficient according to Equation (2.29).

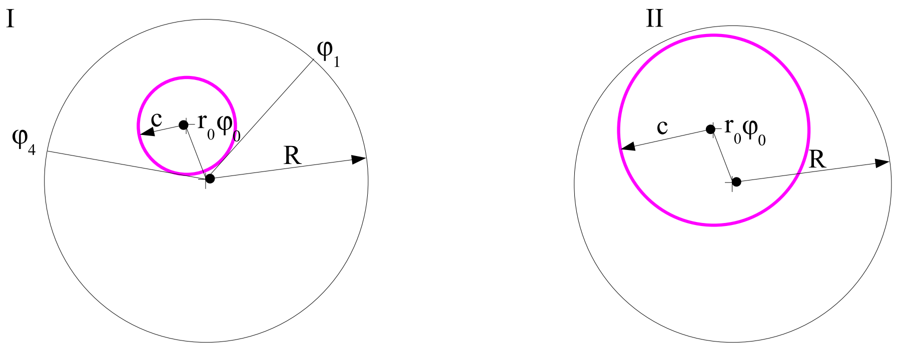

(a) $0 < r_c < R/2 \wedge r_c < R - r_o$
$\int_{\varphi_1}^{\varphi_4}\int_{r_1}^{r_2} f(r_s,\varphi_s)\,dr_s\,d\varphi_s$

(b) $R/2 < r_c < R - r_o \wedge r_c < R - r_o$
$\int_{0}^{2\pi}\int_{r_1}^{r_2} f(r_s,\varphi_s)\,dr_s\,d\varphi_s$

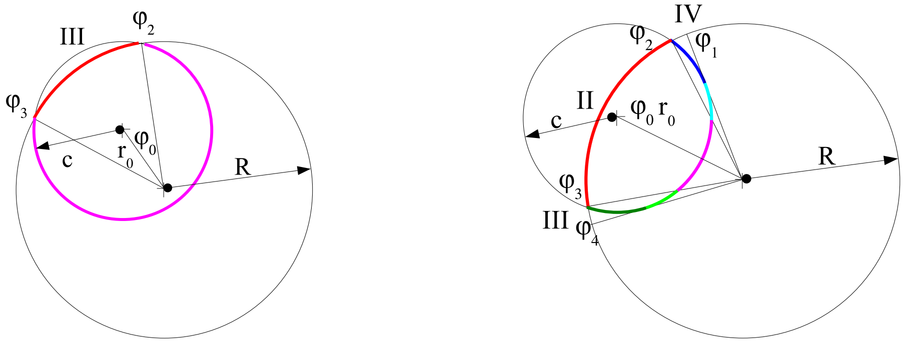

(c) $r_o < r_c < R + r_o \wedge R - r_o < r_c$
$\int_{0}^{\varphi_2}\int_{r_1}^{r_2} f(r_s,\varphi_s)\,dr_s\,d\varphi_s +$
$\int_{\varphi_2}^{\varphi_3}\int_{r_1}^{R} f(r_s,\varphi_s)\,dr_s\,d\varphi_s +$
$\int_{\varphi_4}^{2\pi}\int_{r_1}^{r_2} f(r_s,\varphi_s)\,dr_s\,d\varphi_s$

(d) $R - r_o < r_c < r_o \wedge R - r_o < r_c$
$\int_{\varphi_1}^{\varphi_2}\int_{r_1}^{r_2} f(r_s,\varphi_s)\,dr_s\,d\varphi_s +$
$\int_{\varphi_2}^{\varphi_3}\int_{r_1}^{R} f(r_s,\varphi_s)\,dr_s\,d\varphi_s +$
$\int_{\varphi_3}^{\varphi_4}\int_{r_1}^{r_2} f(r_s,\varphi_s)\,dr_s\,d\varphi_s$

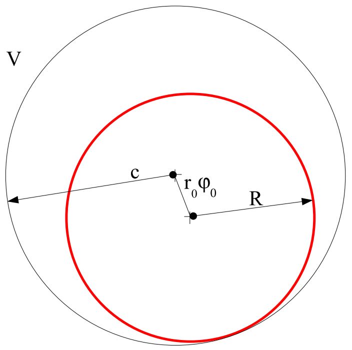

(e) $R + r_o < r_c$
$\int_{0}^{2\pi}\int_{0}^{R} f(r_s,\varphi_s)\,dr_s\,d\varphi_s$

$$
\begin{aligned}
A &= r_c^2 - r_o^2 + r_o^2\cos^2(\varphi_s - \varphi_o)\\
B &= \sqrt{r_o^2 - r_c^2/r_o)}\\
C &= \sqrt{R^2 + r_o^2 - r_c^2}\\
r_1 &= r_o\cos(\varphi_s - \varphi_o) - \sqrt{A}\\
r_2 &= r_o\cos(\varphi_s - \varphi_o) + \sqrt{A)}\\
\varphi_1 &= \varphi_o - \arccos(B/r_o)\\
\varphi_4 &= \varphi_o + \arccos(B/r_o)\\
\varphi_2 &= \varphi_o - \arccos(C/(2\,R\,r_o))\\
\varphi_3 &= \varphi_o + \arccos(C/(2\,R\,r_o))
\end{aligned}
$$

Figure 3.6: Evaluation of the pressure observed at a single point observer at different times.

This leads to an equation for the pressure detected at the Receiver:

$$p_{\text{Receiver}} = \iint\limits_{\text{Receiver}} p_{\text{Sender},0} \cdot S(x_{\max}) \cdot 2 \cdot p_{\text{z}}(z_o) \cdot \frac{J_1(X)}{X} \cdot e^{-\alpha \cdot x} \qquad (3.29).$$

Two variables are unknown in Equation (3.29), the strength $p_{\text{Sender},0}$ of the initial pulse in the Sender and the attenuation coefficient α of the liquid. But if the device is calibrated using a standard liquid, i.e. water, the strength of the initial pulse is kept constant and the pseudo-attenuation coefficient α_{Mutec} measured by the *Mutec Penetration Dynamics Analyser* gives at least a relative measurement result. The pseudo-attenuation coefficient α_{model} for the Mutec predicted by the model is then:

$$\alpha_{\text{model}} = \frac{p_{\text{Receiver, test-liquid}}}{p_{\text{Receiver, calibration liquid}}} \qquad (3.30).$$

3.3 Model for the sample-holder

The model for the sample-holder accounts for the loss of the detected ultrasonic intensity due to reflection at the sample-holder's surface. These losses depend on the thickness of the sample-holder, its material properties, and the surrounding liquid.

For measurements with the sample-holder the device is calibrated using degassed water in the measurement chamber. This gives the pressure $p_{\text{without sample-holder}}$ detected at the receiver. Unfortunately this pressure is not readily available in the *Mutec Penetration Dynamics Analyser*, but the calibration will put all subsequent measurements in relation to the calibration, thus allowing the formulation of a model for the pseudo-attenuation coefficient α_{model} of the *Mutec Penetration Dynamics Analyser*.

The situation of the 10 mm Sender and Receiver with the sample-holder is sketched in **Figure 3.7**. The sample-holder is at an angle α with regard to the centre-line of the Sender-Receiver set-up. This angle is $\alpha_{sh} = 9.5^o$. Hence the pressure field on the surface is not symmetrical. The projected area of the beam on the sample-holder has to be calculated in order to determine the pressure on the sample-holder. The position vector of the sample-holder is $\vec{r_{sh}}$, and its coordinates denoted by the index sh are:

$$\vec{r_{sh}} = \begin{pmatrix} r_{sh} \\ \varphi_{sh} \\ z_{sh,0} + r_{sh} \cdot \tan \alpha_{sh} \cdot \cos(\varphi_{sh}) \end{pmatrix} \qquad (3.31).$$

In the sample-holder's position vector $\vec{r_{sh}}$, the position of the sample-holder on the centre-line between Sender and Receiver is $z_{sh,0}$. In Equation (2.15) z_o can be replaced by $z_{sh,0} + r_{sh} \cdot \tan(\alpha_{sh}) \cdot \cos(\varphi_{sh})$ from Equation (3.31) to give the z-component of the sample-holder. The distance between an element of the Sender and an element on the sample-holder is then a function of ($\vec{r_s}$, $\vec{r_{sh}}$):

$$d(r_s, \varphi_s, z_s, r_{sh}, \varphi_{sh}, z_{sh}) = \mid \vec{r_{sh}} - \vec{r_s} \mid =$$

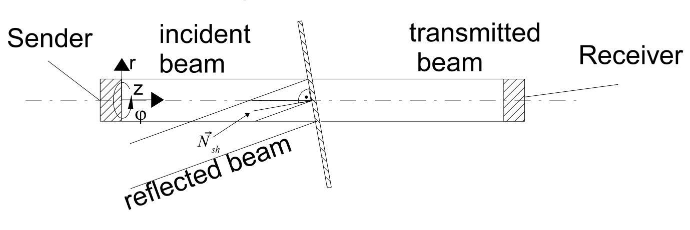

Figure 3.7: Situation of the 10 mm Sender and Receiver with the sample-holder. $\vec{N}_{sh}$ is the normal vector of the sample-holder. α is the angle between the centre line of the Sender and the sample-holder.

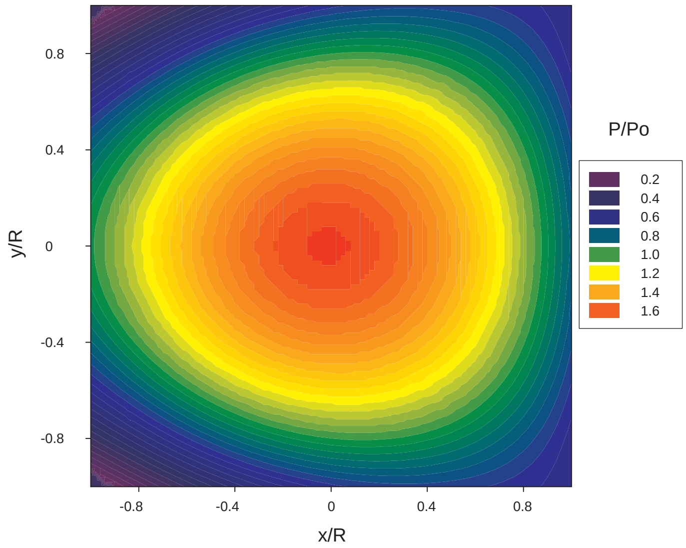

Figure 3.8: Acoustic pressure distribution on the sample-holder using Equation (3.33). The values used are for the diameter $D = 10$ mm, the frequency of the sound-field $f = 1$ MHz, the density of the medium $\rho = 1000$ kg/m^3, and the velocity of sound $c = 1500$ m/s, the maximum velocity of Sender surface $v_{\max} = 1$ m/s. An arbitrary value of 1 m/s is used for the maximum velocity of the Sender. The calculation is performed using a 101 × 101 grid.

$$\frac{\sqrt{r_{sh}^2 + r_s^2 + (z_{sh,0} + r_{sh} \cdot \tan(\alpha) \cdot \cos(\varphi_{sh})^2 - ...}}{... \, 2 \cdot (z_{sh,0} + r_{sh} \cdot \tan(\alpha) \cdot \cos(\varphi_{sh}) \cdot z_s + z_s^2 - 2 \cdot r_{sh} \cdot r_s \cdot \cos\left(\varphi_{sh} - \varphi_s\right).} \tag{3.32}$$

The distance is introduced into Equation (2.15)

$$p = \frac{\rho \cdot v \cdot \omega}{2 \cdot \pi} \int\limits_0^{D/2} \int\limits_0^{2\pi} \frac{r_s \sin \frac{\omega}{2} \left(\frac{t_{max}}{\pi} - \frac{2 \cdot d(r_s, \varphi_s, z_s, r_{sh}, \varphi_{sh}, z_{sh})}{c} \right)}{d(r_s, \varphi_s, z_s, r_{sh}, \varphi_{sh}, z_{sh})} d\varphi_s \, dr_s \qquad (3.33).$$

An evaluation of Equation (3.33) for the 10 mm Sender shows that far-field conditions are established. It is also evident that the pressure distribution is no longer rotationally symmetric, but has an axial symmetry with regard to the x-axis. The result is plotted in **Figure 3.8**.

Figure 3.8 implies also that for the 0.01 m-diameter-Sender far-field conditions are reached at the position of the sample-holder. Due to this the Sender can be regarded as a point source, and interference need not be taken into account when calculating the transmission of ultrasound through the sample-holder.

The sample-holder is a thin plate consisting of polycarbonate. It can be treated as a thin plate in the path of the ultrasonic beam as shown in

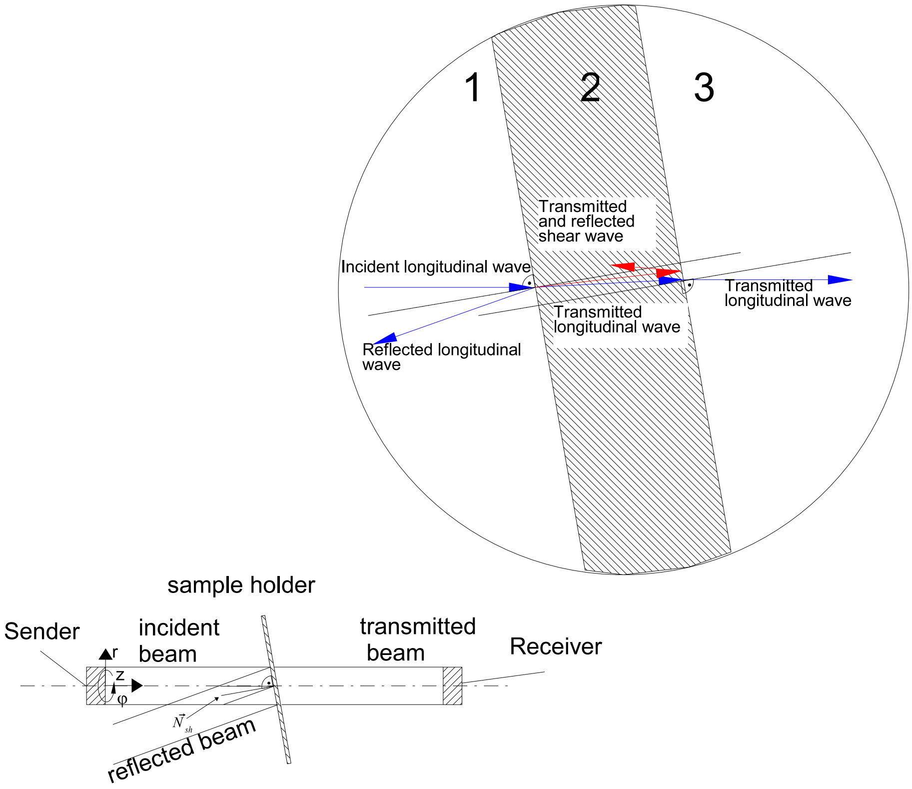

Figure 3.9: Magnified sketch of the sample-holder. The incident longitudinal wave originating at the Sender travels through a liquid and reaches the phase boundary between liquid (1) and sample-holder (2). Part of the wave is reflected, the other part is transmitted. The transmitted part is split into a longitudinal wave (blue) and a shear wave (red). At the boundary between sample-holder (2) and liquid (3), the shear wave is completely reflected whereas one part of the longitudinal wave is transmitted and the other part is reflected. The liquids (1) and (3) have the same physical properties.

Figure 3.9. At the boundary between liquid and sample-holder (1/2) a part of the ultrasonic beam is reflected and a part of it is transmitted. The incident wave is a longitudinal wave, as it is propagated through a liquid. At the boundary (1/2) the transmitted part of the wave is partly converted into a transverse wave. The transverse wave is partly reflected at the second boundary (2/3) and partly transmitted and converted into a longitudinal wave, as liquid cannot propagate shear waves [40, pp217]. The longitudinal wave which is transmitted into the sample-holder at (1/2) is partly transmitted through the phase boundary (2/3) into the medium. It is parallel to the incident wave, as the physical properties in 1 and 3 are the same. This allows Equations (2.51) to (2.56) to be used to calculate the transmission through the sample-holder. The pressure detected at the Receiver is

$$p_{\text{with sample-holder}} = p_{\text{without sample-holder}} \cdot T_{\text{p,plate}} \tag{3.34}$$

or as a relative pressure $p^*_{\text{with sample-holder}}$:

$$p^*_{\text{with sample-holder}} = T_{\text{p,plate}} \tag{3.35}$$

The pseudo-attenuation coefficient for the model is then

$$\alpha_{\text{model}} = \frac{p_{\text{with sample-holder}}}{p_{\text{without sample-holder}}} = T_{\text{p,plate}} \tag{3.36}$$

The part of the wave transmitted through a plate is calculated and plotted in Figure 2.12 on page 25. The thickness of the sample-holder is about $2.12 \cdot 10^{-3}$ m. This leads to different degrees of attenuation for the sample-holder, depending on the frequency. The influence of the material properties for a plate made from different plastics is shown in **Figure 3.10**.

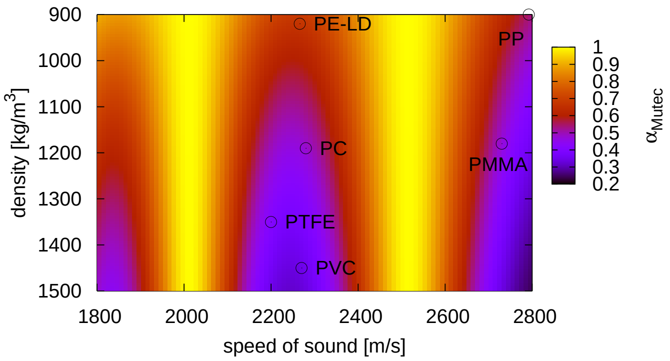

Figure 3.10: Evaluation of the transmission coefficient according to Equation (3.36) regarding the density of and speed of sound in different materials. The medium surrounding the plate is water and the angle of the incident beam is 9.5 °. Different materials are included in the plot. The material properties of polycarbonate (PC), low density polyethylene (LD-PE), polyvinyl chlorine (PVC) and polypropylene are from Folds [12]. The material properties of polytetrafluoroethylene (PTFE) and Plexiglas (PMMA) are from Krautkrämer and Krautkrämer [19].

3.4 Model for the steel insert

As described above, the steel insert in the *Mutec Penetration Dynamics Analyser* is used to measure liquids different from water. The model for the steel insert consists of several parts all depending on the properties of the material within the steel insert:

- The geometric spread of the beam changes the detected signal.
- The ultrasonic beam is refracted and has an offset from the centre line of Sender and Receiver. This leads to a reduction of the detected signal at the Receiver.
- Attenuation reduces the intensity of the ultrasonic beam.
- The loss of intensity due to reflection at the phase boundaries results in a transmission coefficient for the steel insert.

These mechanisms occur inside and outside of the steel insert. Calibrating the *Mutec Penetration Dynamics Analyser* allows compensation for the losses in intensity outside the steel insert. These losses then remain constant for measurements. This means that the model only needs to take into account the change in ultrasonic intensity inside the steel insert.

The challenge when determining the influence of the geometric spread is the fact that the ultrasound travels through different media before reaching the Receiver. The ultrasound travels 3 cm through water, then 3 cm through the test-liquid in the steel insert, and finally 3 cm through water. The precise geometric size of the steel insert is shown in Figure 3.1(b) on page 47.

The reflection at the phase boundaries is neglected for the moment and only the geometric spread is determined. The sound-field in the *Mutec Penetration Dynamics Analyser* is sufficiently described with the help of the near-field distance N. In Figure 3.11 Figure 2.6 is supplemented by the geometry of the *Mutec Penetration Dynamics Analyser*. The location on the centre line of the Sender of the first plastic window, the second plastic window and Receiver are shown. The different symbols indicate a different liquid in the steel insert. The circles indicate water, which is also used for calibration, the triangles stand for ethanol with a concentration of 96% by weight and the squares stand for ethanol with a concentration of 25% by weight. The near-field distance of 96%-ethanol is smaller than the near-field distance of water. This means for 96%-ethanol that within the steel insert the development of the sound-field is less advanced than for water. The near-field distance of 25%-ethanol is larger than the near-field distance of water. This means that within the distance of the steel insert the development of the sound-field is more advanced than with water. The distance z_o for the evaluation of the geometric spread according to Equation (2.20) therefore

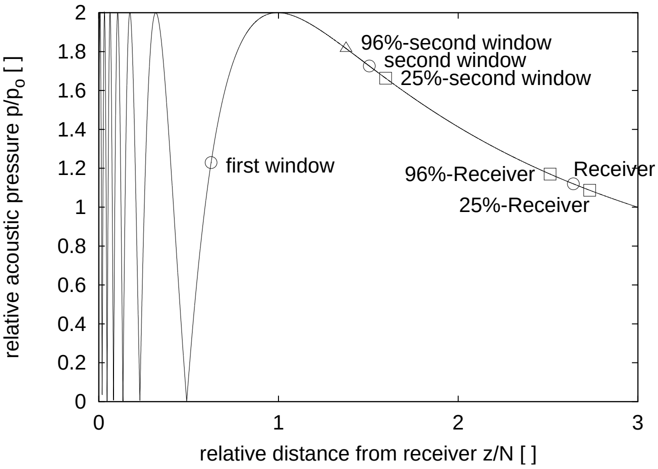

Figure 3.11: Normalized pressure distribution along the centre-line of Sender and Receiver. Significant points of the *Mutec Penetration Dynamics Analyser* are indicated with symbols. The circle stands for a measurement with water as for example during the calibration. The sound-field is compressed or expanded when different materials are in the steel insert. This is shown for different liquids being indicated by different symbols. The triangle stands for an ethanol-water mixture of 25% by weight and the square for an ethanol-water mixture of 96% by weight.

depends on the medium in the steel insert as a function of the near-field distance N_{water} in water and of the near-field distance N_{liquid} in the test-liquid:

$$z_o = 2.13 \text{ cm} + 3 \text{ cm} \cdot \frac{N_{\text{water}}}{N_{\text{liquid}}} + 3.87 \text{ cm} \qquad (3.37).$$

z_o can as well be used for Equations (2.22) and (2.23) to describe the radial distribution of pressure.

For geometric reasons the sinus in Equation (2.23), which again is used to calculate Equation (2.24), is in cartesian coordinates

$$\sin\phi = \frac{\sqrt{x^2+y^2}}{z_o} \qquad (3.38).$$

The pressure in the plane of the Receiver is then

$$p^*_{\text{geometric}}(z_o) = \frac{1}{\pi \cdot R^2} \cdot \int_{-R}^{R} \int_{-\sqrt{R^2-x^2}}^{\sqrt{R^2-x^2}} 2 \cdot p^*(z_o) \cdot \frac{J_1(X)}{X} \, dy \, dx \qquad (3.39).$$

The pseudo-attenuation coefficient $\alpha_{\text{model, geometric}}$ for the geometric spread in the model is therefore

$$\alpha_{\text{model, geometric}} = \frac{p^*_{\text{geometric}}(z_o)}{p^*_{\text{geometric}}(9 \text{ cm})} \qquad (3.40).$$

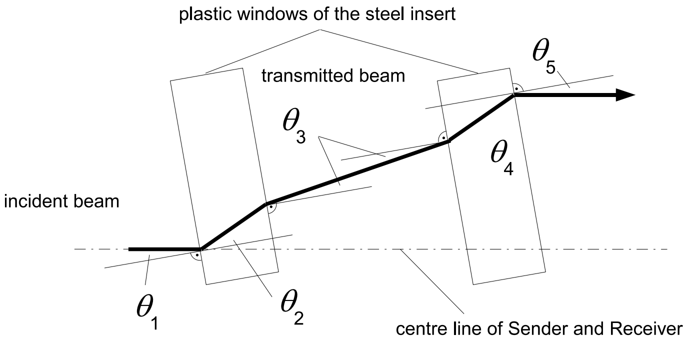

Figure 3.12: Sketch of the path of the ultrasound when the steel insert is used. The medium between the plastic windows is different from the medium on either side of the plastic windows. The angles θ_1 to θ_5 result from Equation (2.36) and are the angles between the path of the beam and the normal of the plastic window.

The volume between the two windows is filled with a liquid which has physical properties different from those of the liquid surrounding the steel insert. Refraction becomes important, as the distance between the two windows cannot be neglected. This leads to an offset between the centre line of the Sender and the Receiver and the centre line of the beam, which means that the cross-section of the beam will only partially cover the area of the Receiver once it has arrived there. The angles θ_1 to θ_5 of the ultrasonic beam with the normal of the plastic window of the steel insert are sketched in **Figure 3.12** and can be calculated as a function of the physical properties of the media using Equation (2.36).

Equation (3.39) is modified to account for the change of the direction of the ultrasonic beam and the resulting offset. The offset of the beam to the centre-line of the Sender and Receiver leads to a reduction in the detected intensity. The offset of the centre-line of the beam towards the centre line of the Sender and Receiver is to a minor extent a function of the material of the window and to a major extent a function of the distance and the material between the two windows. Neglecting the thickness of the plastic windows, the offset of the ultrasonic beam can be calculated. The distance between the two windows is 3 cm and the offset x_{offset} is then a function of the angle θ_3 and θ_1 as defined above:

$$x_{\text{offset}} = 3\ \text{cm} \cdot \frac{\sin(\theta_3 - \theta_1)}{\cos(\theta_3)} \qquad (3.41).$$

Equation (3.41) is plotted in **Figure 3.13**. The offset according to Equation (3.41) results in the fact that the centre of the ultrasonic beam does not coincide with the centre of the Receiver. This means that due to these geometric reasons the detected signal at the Receiver will be weaker than for the case where the centre-line of beam and Receiver coincide. The

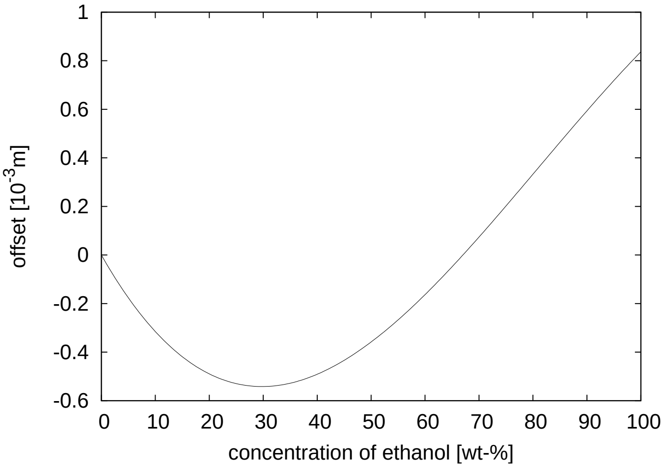

Figure 3.13: Offset of the ultrasonic beam as a function of the medium in the steel insert. The medium in the steel insert is ethanol-water with varying concentrations of ethanol. According to Equation (3.41) the centre line of the ultrasonic beam differs from the centre line of the Sender and Receiver. It is obvious that the diffraction in the steel insert has an impact on the measured result in the *Mutec Penetration Dynamics Analyser*.

pressure at the surface of the Receiver can be calculated with the help of Equation (2.15) or approximated by Equation (2.22). The average relative pressure p^*_{offset} at the surface of the Receiver with regard to its surface area and the offset x_{offset} is:

$$p^*_{\text{offset}}(z_o) = \frac{1}{\pi \cdot R^2} \cdot \int\limits_{-R+x_{\text{offset}}}^{R+x_{\text{offset}}} \int\limits_{-\sqrt{R^2-x^2}}^{\sqrt{R^2-x^2}} 2 \cdot p^*(z_o) \cdot \frac{J_1(X)}{X}\, dy\, dx \qquad (3.42).$$

This gives the pseudo-attenuation coefficient $\alpha_{\text{model, geometric + offset}}$ for the model accounting for the geometric spread and the offset:

$$\alpha_{\text{model, geometric + offset}} = \frac{p^*_{\text{offset}}(z_o)}{p^*_{\text{geometric}}(9\text{ cm})} \qquad (3.43)$$

When the insert is used, the ultrasonic beam has additional phase boundaries to cross, as is shown in **Figure 3.14**. These phase boundaries are the windows in the steel insert. The steel itself reflects almost all the ultrasound and is therefore regarded as impermeable for the ultrasonic beam. The windows are made out of polycarbonate transmitting ultrasound. They can be described by a transmission coefficient in the same manner as the sample-holder. The main difference to the sample-holder consists in the fact that there are different liquids on either side of the plate. The transmission coefficient is derived in the appendix.

The physical properties of the two media (index 1 and 2) in Equations (2.51), (2.52), (2.53), (2.54), (2.55) and (2.56) are not the same. Due to the fact

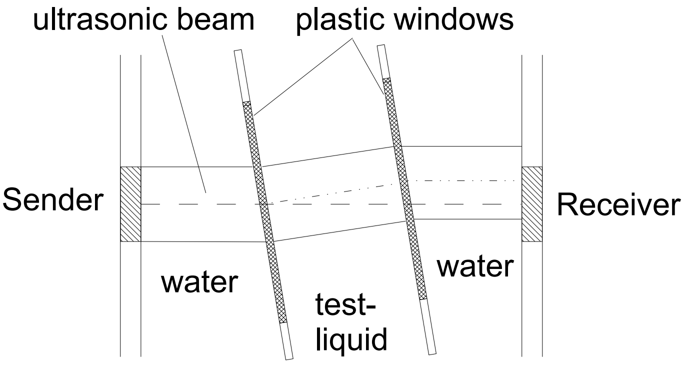

Figure 3.14: Sketch of the steel insert. The steel insert is used for measurements of liquids different from water. On its way from the Sender to the Receiver, the ultrasonic beam has to cross several interfaces. The material properties of the media are different and the propagation of the ultrasonic beam is not perpendicular to the surface of the plastic windows. As a result diffraction occurs and leads to an offset of the centre line of the beam (− · ·) to the centre line of the Sender and Receiver (−−). Consequently the maximum of the beam does not coincide with the centre of the Receiver.

that the chamber is tilted at a certain angle, refraction becomes important, as the distance between the two windows cannot be neglected.

The angles θ_1 to θ_5 are shown in Figure 3.12. These angles are needed to calculate the transmission coefficient of the steel insert. The variables A, B, C and D from Equation (2.51) depend upon $k_{i,x} = k_i \cdot \cos(\theta_i)$ with $i \in [1..5]$. For the situation at the first window A, B, C and D have to be redefined which accounts for the different media on either side of the plastic window. The modifications of A, B, C and D are derived in Appendix A7.

$$A = \left(\frac{\rho_3}{\rho_2} + \frac{k_{3,x}}{k_{2,x}}\right) \cdot \left(\frac{\rho_2}{\rho_1} - \frac{k_{2,x}}{k_{1,x}}\right), \tag{3.44}$$

$$B = \left(\frac{\rho_3}{\rho_2} - \frac{k_{3,x}}{k_{2,x}}\right) \cdot \left(\frac{\rho_2}{\rho_1} + \frac{k_{2,x}}{k_{1,x}}\right), \tag{3.45}$$

$$C = \left(\frac{\rho_3}{\rho_2} + \frac{k_{3,x}}{k_{2,x}}\right) \cdot \left(\frac{\rho_2}{\rho_1} + \frac{k_{2,x}}{k_{1,x}}\right), \tag{3.46}$$

$$D = \left(\frac{\rho_3}{\rho_2} - \frac{k_{3,x}}{k_{2,x}}\right) \cdot \left(\frac{\rho_2}{\rho_1} - \frac{k_{2,x}}{k_{1,x}}\right) \qquad (3.47).$$

The variables for the calculation of the transmission of the second window are A', B', C' and D' and they are defined as:

$$A' = \left(\frac{\rho_1}{\rho_2} + \frac{k_{1,x}}{k_{2,x}}\right) \cdot \left(\frac{\rho_2}{\rho_3} - \frac{k_{2,x}}{k_{3,x}}\right), \tag{3.48}$$

$$B' = \left(\frac{\rho_1}{\rho_2} - \frac{k_{1,x}}{k_{2,x}}\right) \cdot \left(\frac{\rho_2}{\rho_3} + \frac{k_{2,x}}{k_{3,x}}\right), \tag{3.49}$$

$$C' = \left(\frac{\rho_1}{\rho_2} + \frac{k_{1,x}}{k_{2,x}}\right) \cdot \left(\frac{\rho_2}{\rho_3} + \frac{k_{2,x}}{k_{3,x}}\right), \quad (3.50)$$

$$D' = \left(\frac{\rho_1}{\rho_2} - \frac{k_{1,x}}{k_{2,x}}\right) \cdot \left(\frac{\rho_2}{\rho_3} - \frac{k_{2,x}}{k_{3,x}}\right) \quad (3.51).$$

The transmission coefficient for the first window is

$$T_{\text{p, window 1}} = 1 - \text{Real}\left(\frac{\exp\{\imath \cdot 2 \cdot k_2 \cdot d \cdot \cos(\theta_2)\} \cdot A + B}{\exp\{\imath \cdot 2 \cdot k_2 \cdot d \cdot \cos(\theta_2)\} \cdot C + D}\right) \quad (3.52)$$

and for the second window

$$T_{\text{p, window 2}} = 1 - \text{Real}\left(\frac{\exp\{\imath \cdot 2 \cdot k_2 \cdot d \cdot \cos(\theta_2)\} \cdot A' + B'}{\exp\{\imath \cdot 2 \cdot k_2 \cdot d \cdot \cos(\theta_2)\} \cdot C' + D'}\right) \quad (3.53).$$

The transmission coefficient for the entire steel insert, including the medium but neglecting the geometric spread of the beam, is then

$$T_{\text{p, steel insert}} = T_{\text{p, window 1}} \cdot T_{\text{p, window 2}} \quad (3.54).$$

Like the pseudo-attenuation coefficient for the sample-holder, the pseudo-attenuation coefficient $\alpha_{\text{model, transmission}}$ for the reflection occurring at the steel insert is:

$$\alpha_{\text{model, transmission}} = \frac{T_{\text{p, steel insert, liquid}}}{T_{\text{p, steel insert, water}}} \quad (3.55)$$

as a function of the transmission coefficient $T_{\text{p, steel insert, water}}$ of the steel insert filled with water and the transmission coefficient $T_{\text{p, steel insert, liquid}}$ of the steel insert filled with test-liquid.

Equation (3.54) is plotted in **Figure 3.15** for the steel insert filled with water-ethanol blends of different concentrations.

The pressure loss due to attenuation is accounted for by Equation (2.29):

$$p^*_{\text{attenuation}} = e^{-\alpha . x} \quad (3.56)$$

It has to be noted here that the attenuation coefficient α is the *real* attenuation coefficient.

For the model the pseudo-attenuation coefficient $\alpha_{\text{model, attenuation}}$ is

$$\alpha_{\text{model, attenuation}} = \frac{e^{-\alpha_{\text{water}} \cdot 5.13\text{ cm} - \alpha_{\text{water}} \cdot 3.0\text{ cm}}}{e^{-\alpha_{\text{water}} \cdot 9\text{ cm}}} = e^{(-\alpha_{\text{liquid}} + \alpha_{\text{water}}) \cdot 3\text{ cm}} \quad (3.57)$$

as a function of the attenuation coefficient α_{water} of water and the attenuation coefficient α_{liquid} of the liquid in the steel insert.

Equations (3.43), (3.55) and (3.57) are plotted in **Figure 3.16**. These equations can be applied to Equations (3.16) and (3.17) in order to complete the model.

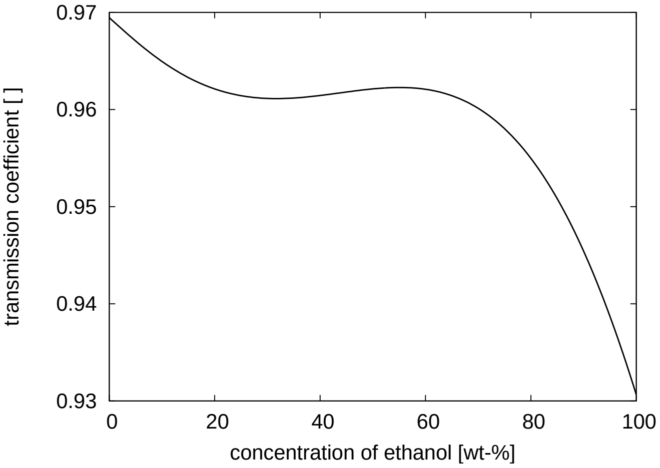

Figure 3.15: Transmission coefficient of the steel insert. The transmission coefficient of the steel insert depends on the liquid inside the steel insert, the properties of the plastic windows, their thickness, and the distance between the two windows. For this calculation polycarbonate $Z = 2.69 \cdot 10^6$ kg/m^2/s with a thickness of $1.22 \cdot 10^{-3}$ m is used. The distance between the windows is 0.03 m and the frequency of ultrasound is 2 MHz.

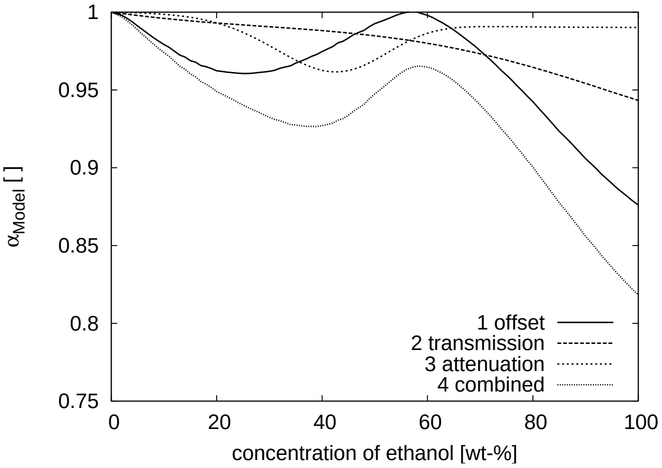

Figure 3.16: Plot of evaluation of Equation (3.42), series (1), Equation (3.54), series (2), Equation (3.56), series (3) and the combination Equation (3.57), series (4) for different blends of water with ethanol relative to the pressure detected at the Receiver when the steel insert is filled with water. This relation is the pseudo-attenuation coefficient α_{model} for the *Mutec Penetration Dynamics Analyser*. The relative pressure at the Receiver due to the offset of the centre line of the beam is curve 1, the relative pressure resulting from transmission losses in the steel insert is 2 and the combination of both is 3.

Equations (3.16) and (3.17) describe the maximum pressure detected in the Receiver. The pressure detected in the Receiver is also a result of the dynamics of Sender and Receiver. As the transmission coefficient for the steel insert is independent of the ultrasonic intensity of the beam and constant for a given set-up i.e. liquid in the steel insert, Equation (3.16) respective Equation (3.17) are proportional to the transmission coefficient.

The pseudo-attenuation coefficient puts all measurements in relation to a calibration measurement. If this calibration measurement is a measurement with a water-filled steel insert, all the following measurements will be normalised to this measurement and α_{model} is

$$\alpha_{\text{model}} = \alpha_{\text{geometric + offset}} \cdot \alpha_{\text{transmission}} \cdot \alpha_{\text{attenuation}} \qquad (3.58).$$

3.5 Model for the membrane

The model for the membrane results in a qualitative description of the processes occurring during a measurement. The result is a scattering cross-section of a membrane which corresponds to an attenuation coefficient.

The membrane consists of polycarbonate with straight and cylindrical pores as shown in **Figure 3.17**. The pores are filled with air. When the membrane is exposed to a liquid the pores are filled depending on the contact angle between liquid and membrane. This leads to enclosures of air. Due to the difference in acoustic impedance of air and water scattering occurs. A calculation following Minnaert [28] is performed to obtain the resonance frequency of a partly filled membrane pore. The situation of an empty pore (a), a partly filled pore (b) and a partly filled pore with a superimposed displacement of the liquid air interface (c) is shown in **Figure 3.18**.

Ultrasound propagating through the liquid-membrane system causes the interface between liquid and air to move. The interface in the pore of the

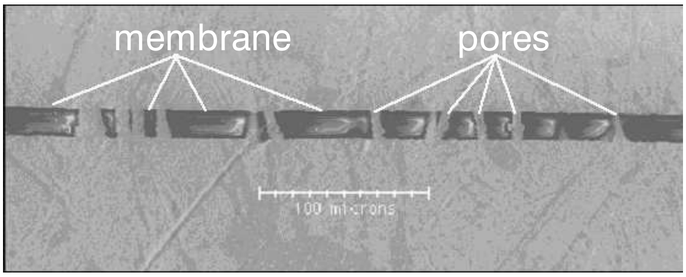

Figure 3.17: SEM picture of the cross-section of a membrane embedded in Woods-Metal. It can be seen that the pores are relatively straight. The centre line of the pores is not orthogonal to the surface of the membrane.

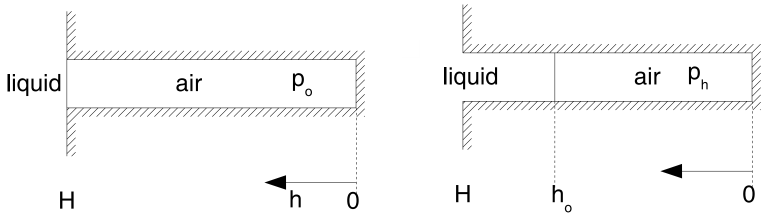

(a) Sketch of a pore without penetration. The ambient pressure in the pore is p_o.

(b) Sketch of a pore after penetration has taken place. Due to the penetration the pressure p_h in the pore has increased.

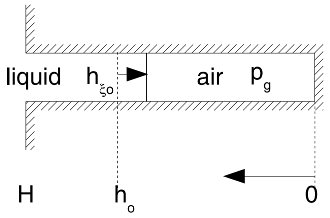

(c) Sketch of a sealed pore after penetration has taken place. The interface of the pore is displaced by Δh. The pressure in the gas has increased to $p_g = p_{h+\Delta h}$

Figure 3.18: Sketch of a pore. The pore is initially filled with air at the ambient pressure. The liquid penetrates and the pressure in the pore increases. The interface of liquid and air is then displaced by a short distance and a further pressure change takes place.

membrane is initially displaced by a maximum of ξ_0 and then follows a harmonic undamped wave equation

$$m \cdot \ddot{\xi} + k \cdot \xi = 0 \tag{3.59}$$

with the solution

$$\xi = \xi_0 \cdot e^{i \cdot \omega_0 \cdot t} \tag{3.60}$$

and with $\omega_0 = \sqrt{\frac{k}{m}}$.

Minnaert's way of treating a bubble can be adopted for a pore. The result is a resonance frequency of a pore. The pore has the depth H and is partly filled with water. The remaining gas volume in the pore is $V_h = \pi \cdot R^2 \cdot h_0$ as a function of the radius R of the pore. The penetrated liquid volume is $V_l = \pi \cdot R^2 \cdot (H - h_0)$. The equation is regarded as stationary without penetration due to capillary suction, the penetration depth being $H - h_0$. Minnaert balances the kinetic energy E_{kin} of the liquid with the energy E_{pot} stored in the elastic compression of the air. The kinetic energy of the gas is neglected, as is the compression of the liquid. This is justified, as the density ρ_{air} of air is much lower than the density ρ_l of the liquid, hence the kinetic energy is much lower. The liquid is almost incompressible compared to the air and therefore the potential energy stored in the elastic deformation of the liquid is much lower than that of the air.

The surface of the air-liquid interface can be expressed using a differential equation (2.66), described in further details below. The velocity of the movement is $\dot{\xi}$ and its maximum is $\dot{\xi}_0 = \xi_0 \cdot \omega$ with the initial displacement ξ_0 and the angular frequency ω. The kinetic energy of the water slug moving in the pore is at its maximum when the velocity is at its maximum:

$$E_{\text{kin}} = V_l \cdot \rho_l \cdot \frac{\dot{\xi}_0^2}{2} = \pi \cdot R^2 \cdot (H - h_0) \cdot \rho_l \cdot \frac{\omega_{0,pore}^2 \cdot \xi_0^2}{2} \qquad (3.61).$$

The energy stored in the compression due to the displacement can be calculated for a polytropic gas. According to the spring-and-bob analogy, the energy stored in the volume change is called potential energy:

$$E_{\text{pot}} = \int_{V_h}^{V_{min}} (P_h - P_{h_0})\, dV \qquad (3.62).$$

In this equation P_h is the pressure of the gas phase in the pore at any given penetration depth h. The volume can be substituted for the penetration depth with $V_{min} = \pi \cdot R^2 \cdot (h_0 - \xi_0)$, $V_h = \pi \cdot R^2 \cdot h$ and $dV = \pi \cdot R^2 \cdot dh$. The pressure difference can be calculated with the help of

$$V_{h_0}^{\kappa} \cdot P_{h_0} = P_h \cdot V_h^{\kappa} \tag{3.63}$$

hence

$$
\begin{aligned}
P_h &= \left(\frac{\pi \cdot R^2 \cdot h_0}{\pi \cdot R^2 \cdot h}\right)^{\kappa} \cdot P_{h_0}: && (3.64)\\
P_h - P_{h_0} &= P_{h_0} \cdot \left(\frac{h}{h_0}\right)^{-\kappa} - P_{h_0} && (3.65)\\
&= \left[\left(\frac{h}{h_0}\right)^{-\kappa} - 1\right] \cdot P_{h_0} && (3.66)
\end{aligned}
$$

under the assumption of a polytropic gas with the polytropic exponent κ. The knack is now formally to introduce $h_\xi = h - h_0$ and afterwards to perform a development of a binomial series using the linear term

$$
\left[\left(\frac{h_0 + h_\xi}{h_0}\right)^{-\kappa} - 1\right] = \left[\left(1 + \frac{h_\xi}{h_0}\right)^{-\kappa} - 1\right] \qquad (3.67).
$$

For small displacements h_ξ the binomial series for the term in parentheses is

$$
\left(1 + \frac{h_\xi}{h_0}\right)^{-\kappa} \approx 1 - \kappa \frac{h_\xi}{h_0} \qquad (3.68).
$$

Reintroducing the original variables gives a linearised form of the equation for the energy stored in the compression.

$$
\begin{aligned}
E_{\text{pot}} &\approx \int_{h_0}^{h_0 - \xi_0} \kappa \cdot \frac{h - h_0}{h_0} \cdot P_{h_0} \cdot \pi R^2 \, dh && (3.69)\\
&= \kappa \cdot \pi \cdot R^2 \cdot P_h \cdot \left.\frac{-h_0 \cdot h + h^2/2}{h_0}\right|_{h_0}^{h_0 - \xi_0} && (3.70)\\
&= \frac{\xi_0^2 \cdot \kappa}{2 \cdot h_0} \cdot P_0 \cdot \left(\frac{H}{h_0}\right)^{\kappa} \cdot \pi \cdot R^2 && (3.71)
\end{aligned}
$$

Now the maximum kinetic energy and the maximum energy stored in the compression have to be equal:

$$
\frac{\xi_0^2 \cdot \kappa}{2 \cdot h_0} \cdot P_0 \cdot \left(\frac{H}{h_0}\right)^{\kappa} \cdot \pi \cdot R^2 = \pi \cdot R^2 \cdot (H - h_0) \cdot \rho_l \cdot \frac{\omega_{0,pore}^2 \cdot \xi_0^2}{2} \qquad (3.72).
$$

This leads directly to a term for the resonance frequency $\omega_{0,pore}$ for a pore:

$$
\omega_{0,pore} = \sqrt{\frac{\kappa \cdot P_0}{(H - h_0) \cdot h_0 \cdot \rho_l} \cdot \left(\frac{H}{h_0}\right)^{\kappa}} \qquad (3.73)
$$

with the ambient pressure P_0. The resonance frequency depends on the total pore length H as well as on the length h_0 of the gas volume. The penetration depth can be calculated by $H - h_0$.

On comparing Equation (3.73) for a pore with Equation (2.68) for a bubble it becomes clear that the level of liquid penetrated into the pore and the

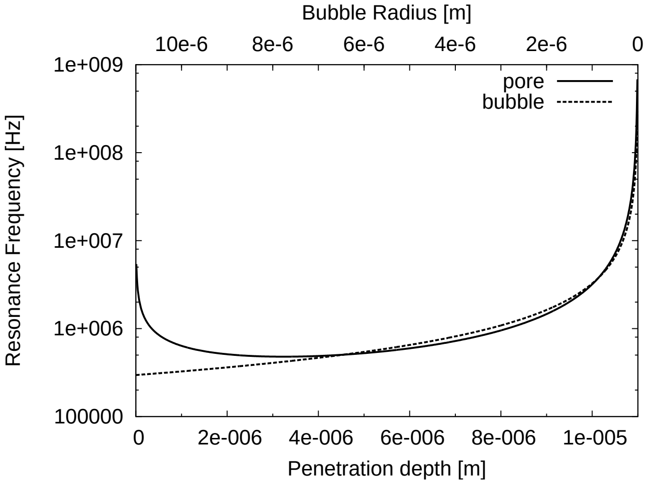

Figure 3.19: Comparison of the resonance frequency of a bubble and a pore. Bubbles with small radii have a resonance frequency similar to a pore filled with gas where liquid has displaced the gas partly. When only little water has penetrated the pore, the shape of the curve describing the resonance frequency of a pore differs from that of a bubble.

pore depth are now the influencing parameters and not the radius of the pore. This is plotted in **Figure 3.19**.

The scattering cross-sections (Equations (2.81) and (2.82)) still depend on the radius R of the pore. This changes when viscous losses are taken into account as described earlier. The difference between the scattering cross-section of a bubble and a pore of 5 µm is plotted in **Figure 3.20**.

The above calculations are valid only when there are no losses. They can be translated into a formal differential equation of the form as given in Equation (3.59):

$$m \cdot \ddot{\xi} + k \cdot \xi = 0 \tag{3.74}$$

with the mass $m = \pi \cdot R^2 \cdot \rho_l \cdot (H - h_0)$ and the spring constant $k = \frac{\kappa \cdot P_0 \cdot \pi R^2}{h_0} \cdot \left(\frac{H}{h_0}\right)^{\kappa}$. Equation (2.69) can be modified to accommodate a dissipative term $b \cdot \dot{\xi}$:

$$m \cdot \ddot{\xi} + b \cdot \dot{\xi} + k \cdot \xi = F_0 \cdot e^{i \cdot \omega \cdot t} \tag{3.75}$$

with the damping constant b. Under the assumption that all viscous losses occur in the liquid phase the Hagen-Poiseuille-Law for viscous loss in a tube can be applied to calculate the viscous loss. The dampening constant b becomes

$$b = 8 \cdot \pi \cdot \eta \cdot (H - h_0) \qquad (3.76).$$

The solution is still of the same form as without damping. For the steady state only the driving frequency is important and the solution is purely the

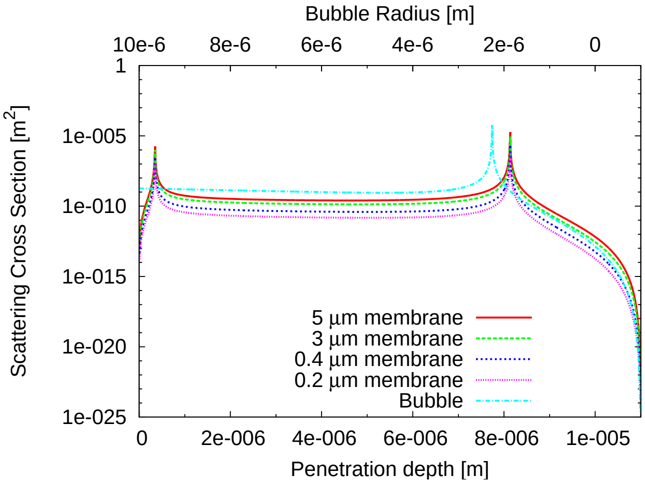

(a) 1 MHz

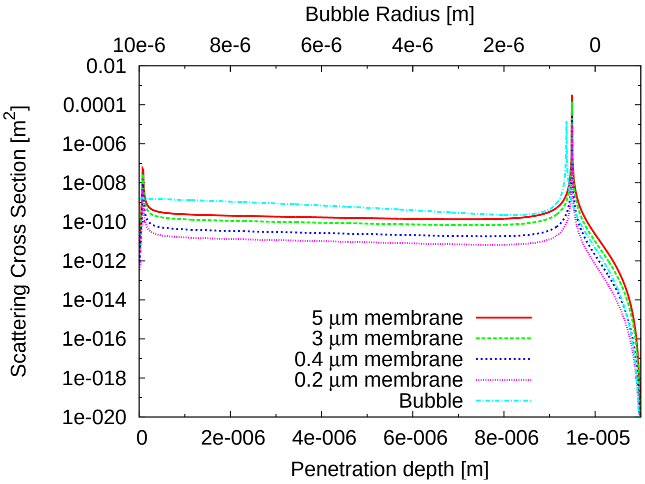

(b) 2 MHz

Figure 3.20: Comparison of the scattering cross-section of an oscillating bubble without dissipation with a pore filled with gas where the interface is oscillating. Equation (2.81), which is valid for a bubble, is infinite for one radius only. Equation (2.82) is valid for a pore and has two penetration depths where it becomes infinite.

particular part of Equation (2.70). Introducing $\beta_{tot} = b/(2 \cdot m)$ the result of the resonance frequency $\omega_{d,pore}$ in the damped system becomes

$$\omega_{d,pore} = \sqrt{\omega_0^2 - \beta_{tot}^2} \qquad (3.77).$$

The scattering cross-section can be calculated in the same way as in Equation (2.82). The result is:

$$\sigma_s = \frac{S_{pore}}{\left(\left(\frac{\omega_{d,pore}}{\omega}\right)^2 - 1\right)^2 + \left(\frac{2 \cdot \beta_{tot}}{\omega}\right)^2}, \qquad (3.78)$$

with the surface S_{pore} of the air in the pore and the angular frequency ω of the sound-field. The resulting graphs are plotted in **Figure 3.21**.

A membrane fixed to the sample-holder of the Mutec can be regarded as sealed on one side. The liquid penetration into the capillaries of the membrane uses two different processes, as described in Section 2.2. The first and faster process is the penetration into the capillary due to capillary suction. As a result of the increased pressure in the capillary, air is transferred across the phase boundary in accordance with Henry's law. The number of gas molecules in the gas volume decreases and the pressure drops. Consequently liquid penetrates into the capillary. This is the second process. In both cases the capillary suction is opposed by the force due to viscous friction and the pressure built up in the sealed capillary. Gravity is not important as the pores are horizontal. The hydrostatic pressure becomes unimportant as the immersion depth of the capillary into the liquid is low. Instead the counterpressure becomes important due to the compression of the gas as its volume is reduced by the penetrating liquid. The situation of a capillary in a membrane mounted onto the sample-holder in the *Mutec Penetration Dynamics Analyser* is shown in **Figure 3.22**.

The gas volume $V(t)$ as a function of the volume V_0 of a capillary with the radius R and the penetration depth $h'(t)$ in the prime coordinate system is

$$V(t) = V_0 - \pi \cdot R^2 \cdot h'(t) = \pi \cdot R^2 \cdot H - \pi \cdot R^2 \cdot h'(t) = \pi \cdot R^2 \cdot (H - h'(t)) \qquad (3.79)$$

hence:

$$V(t) = \pi \cdot R^2 \cdot h(t) \qquad (3.80).$$

The pressure change due to the decreased volume as the liquid replaces the gas can be described by Boyle's law. The pressure P of a gas at two different respective times (0 and t) depends on the gas temperature T and volume V at the according time:

$$\frac{P(0) \cdot V(0)}{T(0)} = \frac{P(t) \cdot V(t)}{T(t)}. \qquad (3.81)$$

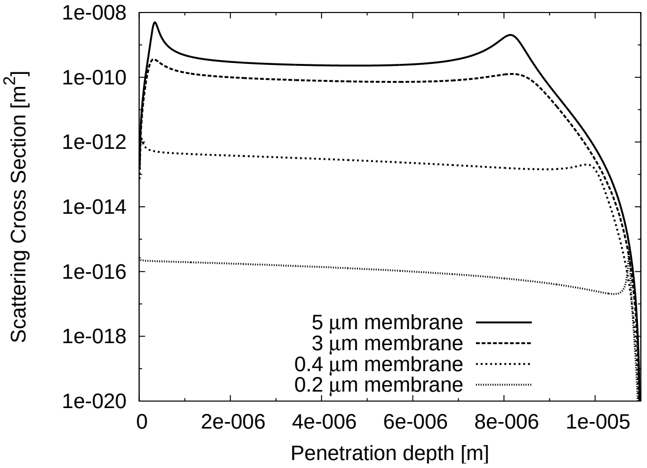

(a) 1 MHz

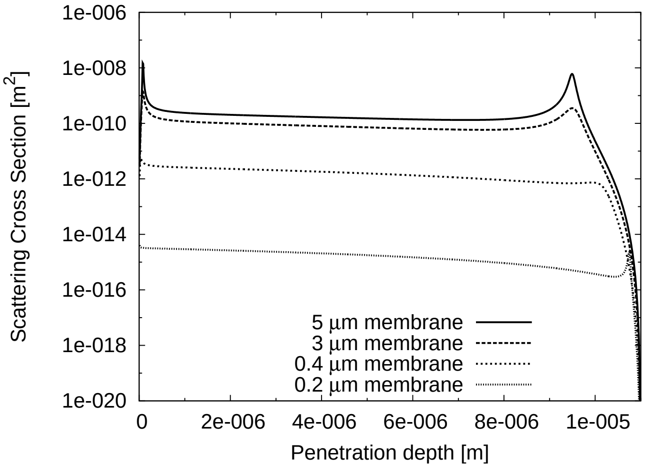

(b) 2 MHz

Figure 3.21: Evaluation of Equation (3.78) describing the scattering cross-section of a pore. Dissipation due to viscous friction is taken into account. Compared to Equation (2.82) the peaks of the function for the scattering cross-section are broader. It can also be observed that the peak on the right side of the graph at higher penetration depths is broader than the peak on the left.

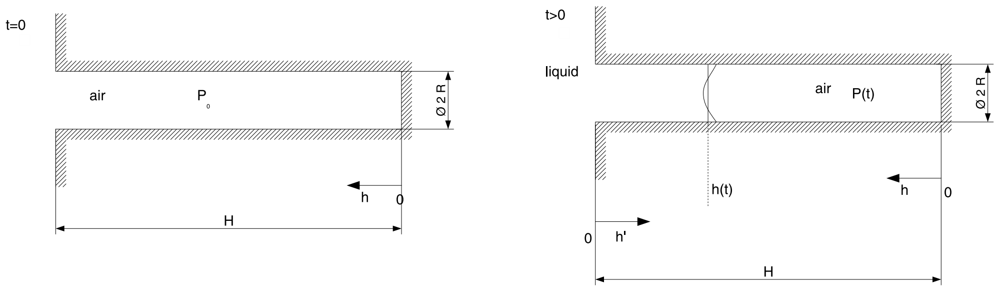

(a) Before the penetration takes place the capillary is filled with gas at the ambient pressure P_0. The volume occupied by the gas is $V_0 = \pi \cdot R^2 \cdot H$.

(b) The membrane is in contact with water at the time $t = 0$. After the time t penetration has taken place, which leads to gas being compressed and its volume being replaced by liquid. The compressed gas has the pressure $P(t)$ and the volume of the gas is now $V(t) = \pi \cdot R^2 \cdot h(t)$

Figure 3.22: Situation of a pore in the membrane when the membrane is mounted on the sample-holder. The capillary is sealed at one side. At the time $t = 0$ the membrane is brought into contact with water and after the time t some penetration has taken place. There are two coordinate systems h and h'. The h-system has its origin at the entrance of the capillary and describes the penetrated liquid, whereas the h'-system has its origin at the closed end of the capillary and describes the gas phase. The transformation between h and h' is $h' = H - h$.

Equations (3.81) and (3.80) give an expression for the pressure of an ideal gas in the capillary of a membrane due to the change in volume with regard to the penetration depth $h'(t)$ as introduced in Figure 3.22 (b):

$$P(t) = \frac{P_0 \cdot V_0 \cdot T_t}{(V_0 - \pi r^2 \cdot h'(t)) \cdot T_0} = \frac{H}{H - h'(t)} \cdot \frac{T(t)}{T_0} \cdot P_0. \tag{3.82}$$

The modified Lucas-Washburn-Equation (1.1) is

$$\frac{dh'}{dt} = \frac{\frac{2 \cdot \gamma \cdot \cos(\Theta)}{R} - \frac{P_0 \cdot H \cdot T(t)}{(H - h'(t)) \cdot T_0} + P_0 + P_h}{8 \cdot \eta \cdot h(t)} \cdot R^2 \tag{3.83}$$

with the hydrostatic pressure P_h at the entrance of the capillary. This equation can be rearranged to give an equation of the form

$$dt = \frac{A \cdot h'(t)}{-C \cdot h(t) + D} - \frac{B \cdot h'(t)^2}{-C \cdot h'(t) + D} \tag{3.84}$$

with

$$\begin{aligned} A &= 8 \cdot \eta \cdot T_0 \cdot H && (3.85) \\ B &= 8 \cdot \eta \cdot T_0 && (3.86) \end{aligned}$$

$$\begin{aligned} C &= 2 \cdot \gamma \cdot R \cdot T_0 \cdot \cos(\Theta) + P_0 \cdot R^2 \cdot T_0 + P_h \cdot R^2 \cdot T_0 & (3.87) \\ D &= \Big(2 \cdot \gamma \cdot R \cdot T_0 \cdot \cos(\Theta) + P_0 \cdot R^2 \cdot T_0 + & (3.88) \\ & \quad + P_h \cdot R^2 \cdot T_0 - P_o \cdot T(t) \cdot R^2\Big) \cdot H. \end{aligned}$$

Hence the solution can be obtained with the help of

$$\int A \cdot \frac{x}{-C \cdot x + D} = A \cdot \left(-\frac{x}{C} - \frac{D \cdot \ln(D - C \cdot x)}{C^2}\right) \quad (3.89)$$

and

$$-\int B \cdot \frac{x^2}{-C \cdot x + D} = -B \cdot \left(-\frac{D \cdot x}{C^2} - \frac{x^2}{2 \cdot C} - \frac{D^2 \cdot \ln(D - C \cdot x)}{C^3}\right) \quad (3.90).$$

The maximum penetration depth $h_{\max}$ due to the capillary suction can be calculated by applying equilibrium conditions to Equation (3.82). The equilibrium is characterized by $T(t) = T_0$ and $P(t) = P_0 + P_L$ obtaining

$$P_0 + P_L = \frac{H}{H - h_{\max}} \cdot P_0, \quad (3.91)$$

leading to

$$h_{\max} = \frac{P_L}{P_0 + P_L} \cdot H \quad (3.92).$$

An evaluation of Equation (3.92) is plotted in **Figure 3.23** as a function of the capillary radius. Inserting the pressure P_L for capillary suction Equation (3.92) becomes

$$h_{\max} = \frac{\frac{2 \cdot \gamma \cdot \cos\Theta}{R}}{P_0 + \frac{2 \cdot \gamma \cdot \cos\Theta}{R}} \cdot H \quad (3.93).$$

As the contact angle becomes smaller the maximum penetration depth becomes larger and is at its maximum at a contact angle of zero. This leads to an approximation for the maximum penetration depth of a liquid into a capillary:

$$h_{\max} = \frac{\frac{2 \cdot \gamma}{R}}{P_0 + \frac{2 \cdot \gamma}{R}} \cdot H \quad (3.94).$$

Equations (3.89) and (3.90) are evaluated with the start and boundary condition $h(t = 0) = 0$ and plotted in a dimensionless way in **Figure 3.24**. It is obvious that the penetration process is very quick and that the maximum penetration depth is reached quickly. If the contact angle becomes smaller, the order of magnitude of the penetration dynamics does not change. This is due to the fact that both the maximum penetration depth and the capillary suction decline.

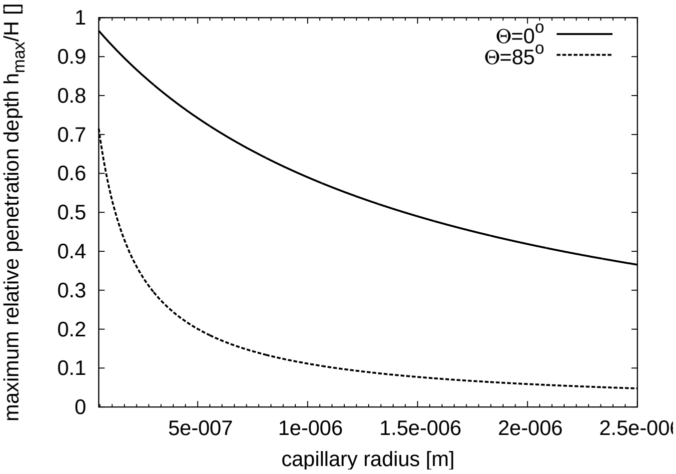

Figure 3.23: Plot of the maximum relative penetration depth h_{max}/H as a function of the capillary radius. Maximum penetration depth calculated with Equation (3.92) ($\Theta = 85$ °) and Equation (3.94) ($\Theta = 0$ °). A capillary with smaller radius and smaller contact angle leads to an increased penetration depth.

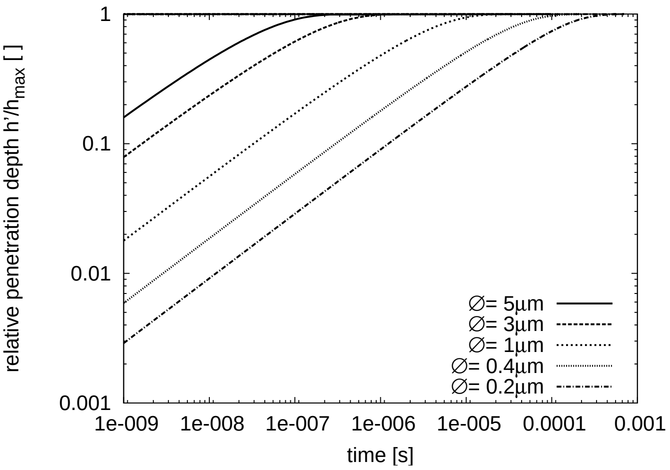

Figure 3.24: Logarithmic plot of the penetration dynamics. The relative penetration depth is calculated by dividing the penetration depth $h'(t)$ by h_{max}. A value of 1 means the penetration due to capillary suction is completed. This still leaves a volume of air remaining in the capillary. The length of the capillary is $H = 10$ µm, contact angle $\Theta = 85$ °, surface tension of the liquid $\gamma = 72 \cdot 10^{-}3$ N/m, ambient pressure $P_0 = 10^5$ Pa, hydrostatic pressure $P_h = 0$ Pa, and isothermal conditions $T_0 = T(t)$.

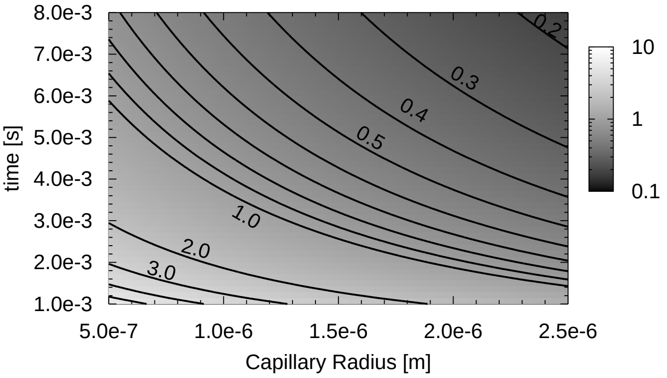

Figure 3.25: Evaluation of the dimensionless term (2.120) for nitrogen diffusing in water. The contour lines in the plot are lines of constant value for $\frac{x^2}{4 \cdot D \cdot t}$. The distance h for diffusion is approximated for a capillary in a membrane by Equation (3.94), which is a function of the capillary radius R. It can be seen that the dimensionless term is smaller than 1 for larger capillary radii and longer times. The first measurement of the Mutec is taken after 8 ms. Within this time-scale the concentration profile becomes quasi-stationary for almost all capillary radii evaluated here. The capillary length for the evaluation is 10 µm.

Due to the increased pressure at the gas-liquid interface gas will be dissolved in the liquid. The subsequent concentration gradient leads to diffusion of gas molecules through the capillary into the bulk of the liquid. The concentration profile which is developed can be described with Equation (2.117), and Equation (2.120) indicates if the process is quasi-stationary or not. Evaluating the dimensionless term

$$\frac{h^2}{4 \cdot D_i \cdot t} \tag{3.95}$$

for nitrogen in water and the maximum penetration depth according to Equation (3.94) gives **Figure 3.25**.

The evaluation of Equation (2.120) produces times at which a quasi-stationary concentration profile is developed. The first measurement value for a measurement with the Mutec is available after 8 ms. Within this time-scale all evaluated capillaries can be regarded as quasi-stationary.

The time-scale for the liquid penetration due to capillary suction can be obtained from Figure 3.24 where Equation (3.84) is evaluated for certain membranes.

The dynamic water penetration into cylindrical pores of a membrane and the scattering cross-section of the partly filled pores can now be calculated using Equations (2.140), (2.84) and (2.86). This set of equations describes the penetration of a liquid into a gas-filled, sealed pore under the following assumptions:

- The penetration due to the capillary suction as described by the modified Lucas-Washburn-Equation (3.84) is very quick and has taken place in a very short time-scale. This means the capillary suction has no influence on the dynamics.
- The capillary suction increases the pressure of the gas in the pore leading to a concentration difference at the gas-liquid interface. Due to this concentration difference diffusion takes place.
- The main mechanism of reducing the volume of the gas phase is due to diffusion.
- The dampening of the ultrasound is through scattering and viscous friction of the liquid slug in the pore.

The resulting graphs of the evaluation for water and different membranes are plotted in **Figure 3.26**.

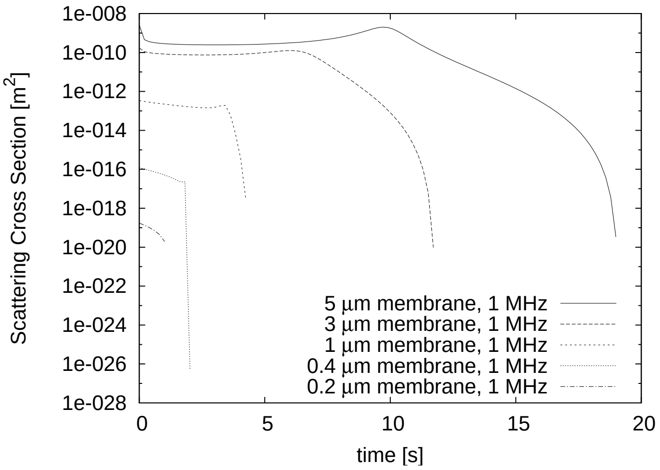

(a) 1 MHz

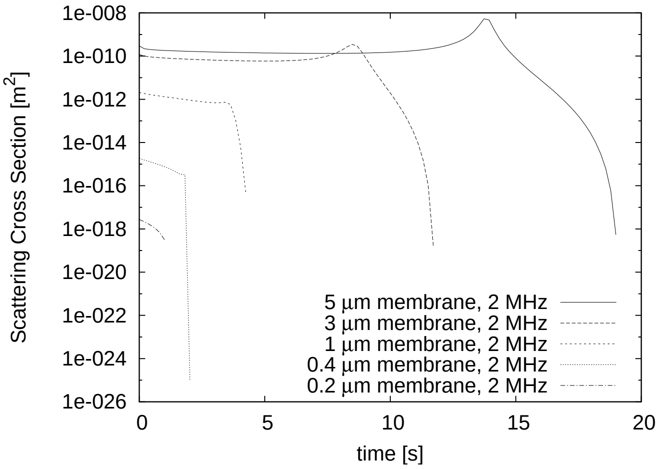

(b) 2 MHz

Figure 3.26: Scattering cross-section for a membrane with cylindrical pores. The membrane is in contact with water. At $t = 0$ the penetration into the membrane due to capillary suction stops and diffusion starts. The gas volume in the pore is replaced by liquid. This leads to a change in resonance frequency and scattering cross-section.

4 Validation of the model

The model for the *Mutec Penetration Dynamics Analyser* is verified by several experiments. The simplest set-up is the measurement chamber filled with liquids having different properties. Measurements of the ultrasonic attenuation give information about the model for the Sender and the Receiver. The validation of the model is undertaken with the help of solutions of manganese-sulfate.

The model for the steel insert is validated by measurements with ethanol-water mixtures. Geometric spread, transmission through the steel insert and diffraction are taken into account.

The model for the sample-holder is verified by measuring the attenuation without the sample-holder and comparing it to measurements with the sample-holder. In conjunction with the geometric and material properties of the sampleholder information about the model is obtained.

The dynamic of penetration is brought into the verification of the model by measuring the liquid penetration into cylindrical pores of a membrane.

4.1 Measurements with liquids

This section deals with attenuation measurements of different liquids in the Mutec. The device is calibrated with distilled and degassed water. The degassing is achieved by treatment of the water in an ultrasonic bath and is stopped once the water stops producing bubbles. Two set-ups for the *Mutec Penetration Dynamics Analyser* are possible for measurements with water. The first measurement set-up is the bare measurement chamber and the second is the measurement chamber using the steel insert. In order to verify the first set-up measurements solutions of manganese-sulfate are used. Manganese-sulfate is characterised by the fact that its acoustic properties, particularly the speed of sound and the attenuation, vary largely with the concentration.

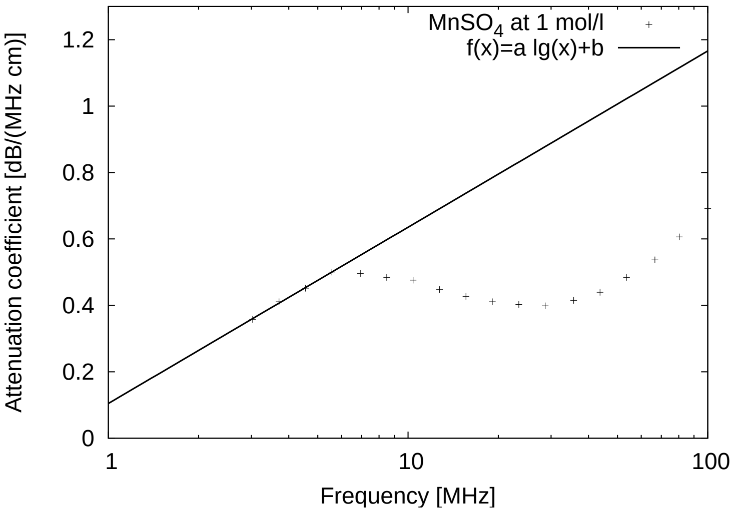

Figure 4.1: Attenuation coefficient for a solution of 1 mol/l manganese-sulfate. The data are measured at 100 MHz and are taken from Dunkhin and Goetz [9]. A linear interpolation of the data for frequencies below 6 MHz gives $f(x) = a \cdot \log(x) + b$ with $a = 0.2305 \pm 0.0078$ and $b = 0.1045 \pm 0.0111$.

4.1.1 Measurements with manganese-sulfate

The attenuation of manganese-sulfate is plotted in **Figure 4.1** for a frequency of up to 100 MHz. The unit of the attenuation coefficient is dB/cm/MHz. A linear interpolation of the attenuation coefficient for frequencies below 6 MHz gives:

$$f(x) = a \cdot \log(x) + b \tag{4.1}$$

where x is the frequency in MHz, $a = 0.2305 \pm 0.0078$ and $b = 0.1045 \pm 0.0111$. The values for the attenuation have to be converted in order to use them in the model:

$$\alpha_{\mathrm{MnSO_4}} = \frac{10^2}{8.8687} \cdot f \cdot \alpha \ \mathrm{Np/m}, \tag{4.2}$$

where α is the attenuation coefficient taken from the graph and f is the frequency of ultrasound in MHz. For a frequency of 2 MHz the attenuation coefficient according to Figure 4.1 and Equation (4.1) is $\alpha_{\mathrm{MnSO_4}} = 0.56$. In order to obtain the attenuation coefficient at the concentrations used in the measurements, a linear interpolation between the value for a 1 mol/l MnSO$_4$-solution and water is used. The attenuation value for water is $\alpha_{\mathrm{water}} = 0.001$ leading to an expression for the attenuation coefficient for solutions of manganese-sulfate of:

$$\alpha_{\mathrm{MnSO_4}}(c_{MnSO_4}) = (0.56 - 0.001) \cdot c_{MnSO_4} + 0.001 \qquad (4.3).$$

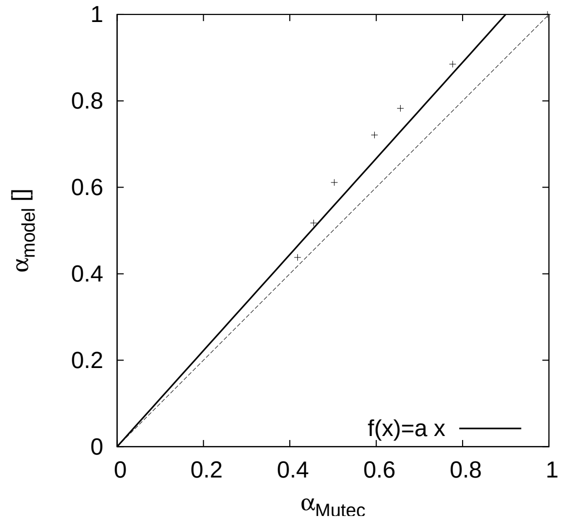

Figure 4.2: Comparison of measurements with the *Mutec Penetration Dynamics Analyser* and results obtained from the model. A linear regression $f(x) = a \cdot x$ of calculated against measured results gives $a = 1.111 \pm 0.035$. The ideal correlation between model and measurements is $a = 1$ which appears in the plot as the dotted line.

In order to verify Equation (3.30) describing the pseudo-attenuation coefficient as measured with the *Mutec Penetration Dynamics Analyser*, measurements with solutions of manganese-sulfate are evaluated. The device is calibrated using pure water in the measurement chamber. After the calibration solutions of manganese-sulfate are measured, ensuring that the initial pulse in the Sender remains of the same strength throughout the measurement series. The results of the measurements and the model are plotted in **Figure 4.2**. The calculation of the results obtained by the model is according to Equation (3.30).

4.1.2 Measurements with ethanol-water mixtures in the steel insert

The ethanol-water mixtures are degassed with the help of an ultrasonic bath. A range of different concentrations of ethanol-water mixtures is tested. When ethanol is mixed with water the physical properties of the mixtures change in a non-linear way with regard to the concentration as shown in **Figure 4.3(a)** and **Figure 4.3(b)**. The theoretic attenuation for the ethanol-water mixture is calculated using data for the density provided by Petong et al. [31] and the speed of sound provided by Parke and Birch [30]. The data are plotted in **Figure 4.3**. Viscosity and speed of sound pass through an extremum as the concentration increases, whilst the density

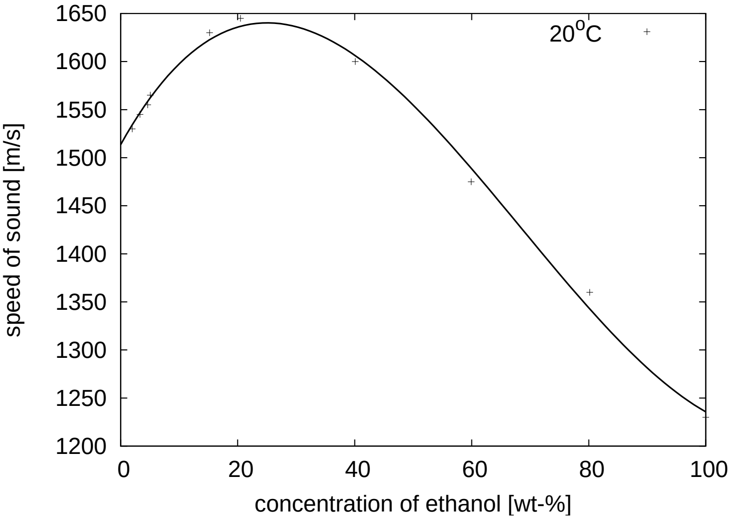

(a) Speed of sound of ethanol-water mixtures as a function of the concentration. Data taken from [30]

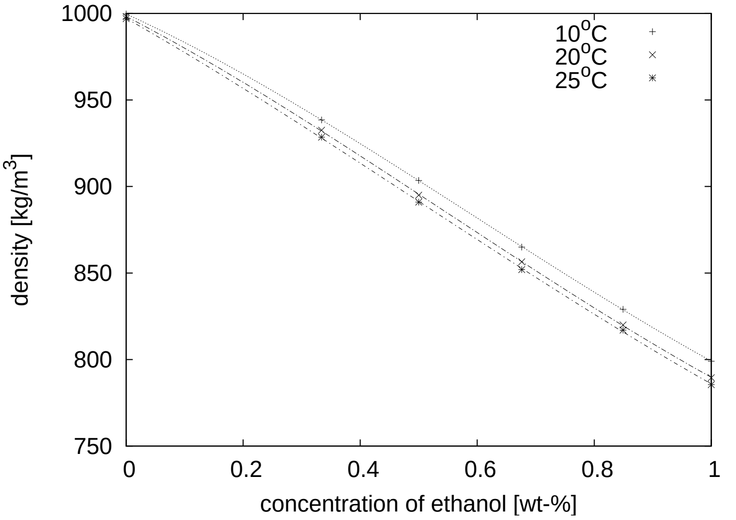

(b) Density of ethanol-water mixtures as a function of the concentration. Data taken from [31].

Figure 4.3: Plot of the speed of sound and density of ethanol-water mixtures of varying concentrations.

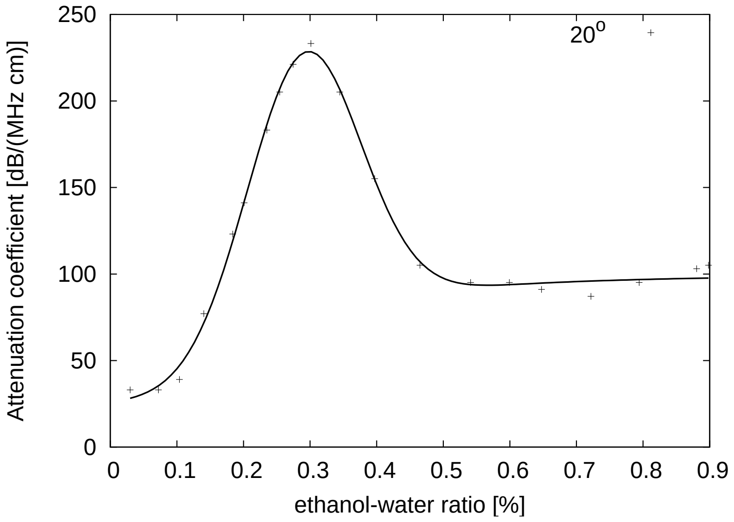

Figure 4.4: Attenuation data for ethanol-water mixtures, provided by Petong et al. [31]. The data points are copied from [31] and the curve is added.

declines. The attenuation of different ethanol-water mixtures can be found in D'Arrigo and Paparelli [7] or Petong et al. [31]. The frequency used to measure the attenuation in Petong et al. [31] is closer to that used in the *Mutec Penetration Dynamics Analyser* and hence these data are used. The attenuation data are plotted in **Figure 4.4**.

The evaluation of the different ethanol-water blends with the *Mutec Penetration Dynamics Analyser* result in a curve which varies around a constant value for the attenuation, depending on the concentration. For **Figure 4.5** these values are averaged and plotted. The standard deviation for each measurement is plotted as error bars.

The resulting graph for the pseudo-attenuation coefficient (Equation (3.57)) obtained by the model is plotted in **Figure 4.6**. The shape of the curves obtained is similar. The pseudo-attenuation coefficient is largest for water. It declines with increasing concentration of ethanol before it increases to pass through a plateau or local maximum and finally declines.

Figures 4.5 and 4.6 can be combined. Plotting the measured result against the predicted results gives **Figure 4.7**. A relation between model and measurement can be observed.

The differences can be explained with some of the earlier assumptions and limitations of the device. According to Figure 3.11 far-field conditions are not developed fully by the time the sound-field reaches the first window of the steel insert. This means that the pressure still varies locally. Generally the importance of the reflection of the liquid within the steel insert is important and has a major influence on the results.

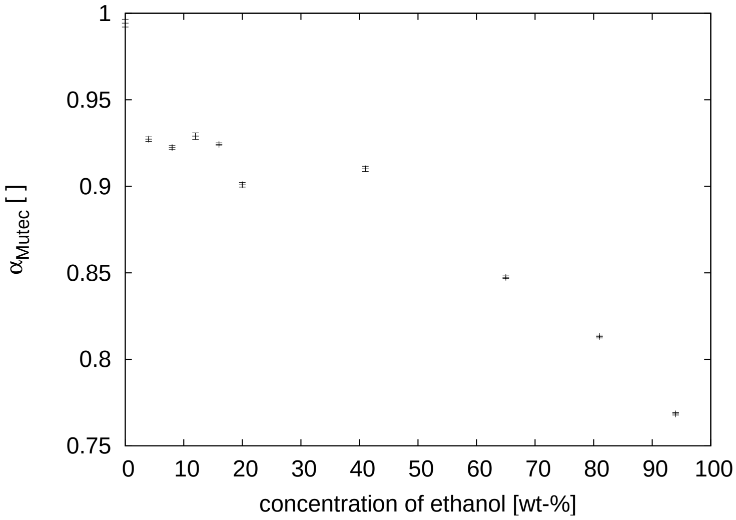

Figure 4.5: Measurements with water and ethanol mixed in different ratios. The value measured is the pseudo-attenuation coefficient as it is given by the Mutec. The pseudo-attenuation coefficient α_{Mutec} is a function of the settings of the Mutec during calibration and the settings of the device as well as the detected pressure during the measurement. The frequency of ultrasound is $f = 2$ MHz.

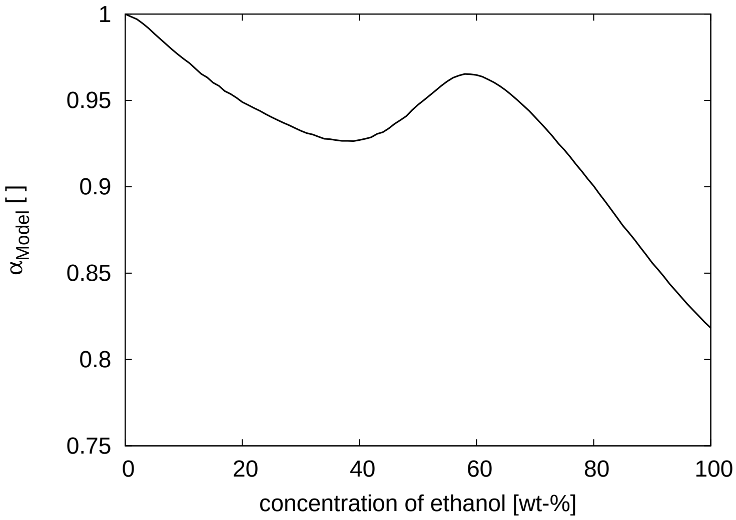

Figure 4.6: Evaluation of the pseudo-attenuation coefficient of the *Mutec Penetration Dynamics Analyser*. The evaluation uses Equations (3.58) and (3.57). The frequency of ultrasound is $f = 2$ MHz .

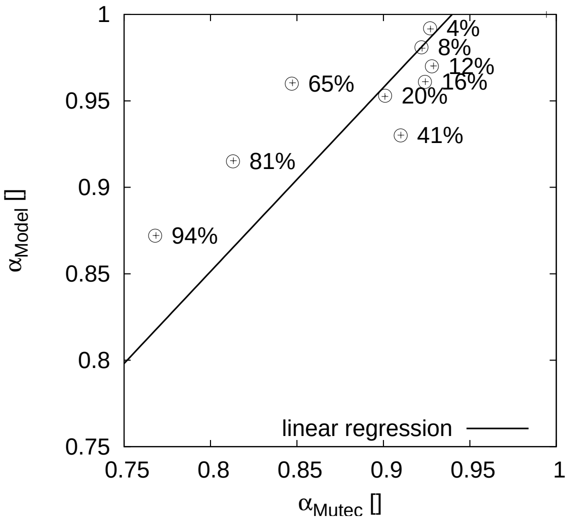

Figure 4.7: Comparison of measured data with results obtained from the model. The linear regression $f(x) = a \cdot x$ gives $a = 1.064 \pm 0.014$.

A linear regression $f(x) = a \cdot x$ for results obtained by the model against results measured with the *Mutec Penetration Dynamics Analyser* delivers $a = 1.064 \pm 0.014$. As the model is rather complex, the uncertainties increase. Nevertheless the correlation shows the right trend. As the material properties of ethanol-water mixtures are taken from different sources, their accuracy and coherency are difficult to assess, and consequently the influence on the obtained values is difficult to predict. The rather diffuse scattering of measurements and predicted values for lower concentrations of the ethanol-water mixtures can be explained by the influence of geometric spread, the transmission through the steel insert and the attenuation coefficient. The geometric spread is a function of the speed of sound in the medium and the transmission depends on the density as well as on the speed of sound. Attenuation and speed of sound of water-ethanol mixtures pass through a local extremum at concentrations between 20 wt-% and 30 wt-%. For larger concentrations the attenuation is constant, and only the speed of sound as well as the density decline, leading to the prediction of smaller values.

This means that the model overestimates the attenuation and underestimates the influence of the geometric spread.

4.2 Measurements with the sample-holder

Measurements with the sample-holder are carried out to validate Equation (3.36). This equation describes the pseudo-attenuation coefficient of the *Mutec Penetration Dynamics Analyser* when the sample-holder is used. Physical properties of the plate and the medium as well as the frequency of the ultrasound are needed to calculate the transmission. The physical properties of the different materials employed are listed in **Table 4.1**. Two sample-holders being supplied with the *Mutec Penetration Dynamics Analyser* are evaluated as well as a sheet of polycarbonate. The sample-holders are labelled 1.C1 and 1.C4. The polycarbonate is labelled PC-3mm. The sample-holder 1.C1 consists of polycarbonate and the sample-holder 1.C4 consists of polypropylene. The properties of the surrounding liquid are those of water with an acoustic impedance $Z_{\text{medium}} = 1.46 \cdot 10^6$ kg/m^2/s, the speed of sound $c_{\text{medium}} = 1470$ m/s and the density $\rho_{\text{medium}} = 996$ kg/m^3.

As shown in Figure 2.12 on page 25 a polycarbonate plate with a thickness of $2.12 \cdot 10^{-3}$ m gives a value for the transmission coefficient of 0.74 for a frequency of 1 MHz and 0.48 for a frequency of 2 MHz. To evaluate these results measurements with the *Mutec Penetration Dynamics Analyser* are carried out. The device is calibrated using water in the measurement chamber without the sample-holder. This means that the pseudo-attenuation coefficient α_{model} for a measurement with water and without the sample-holder gives a value of $\alpha_{\text{Mutec}} = 1$. The measurement with the *Mutec Penetration Dynamics Analyser* shows that the resulting pseudo-attenuation coefficient is $\alpha_{\text{Mutec}} = 0.998$. Then measurements are carried out using the sample-holder only. The resulting curves are shown in **Figure 4.8(a)**.

The value for the measured pseudo-attenuation coefficient is $\alpha_{\text{Mutec}} = 0.51 + / - 0.006$ for the 2 MHz ultrasound and it is $\alpha_{\text{Mutec}} = 0.86 + / - 0.005$ for the 1 MHz ultrasound. It can be seen that the curve measured with the *Mutec Penetration Dynamics Analyser* does not change with time. The variation in the curve is due to measurement inaccuracy.

Further measurements with an additional sample-holder as supplied with

	unit	1.C1	1.C4	PC-3mm
thickness	[10^{-3} m]	2.12	2.55	3.00
ρ_{plate}	[kg/m^3]	1190	900	1190
c_{plate}	[m/s]	2280	2792	2280
Z_{medium}	[10^6 kg/m^2/s]	2.71	2.51	2.71

Table 4.1: Physical properties of the sample-holders supplied with the *Mutec Penetration Dynamics Analyser*. Sample-holder 1.C1 consist of polycarbonate (PC) and sample-holder 1.C4 consists of polypropylene

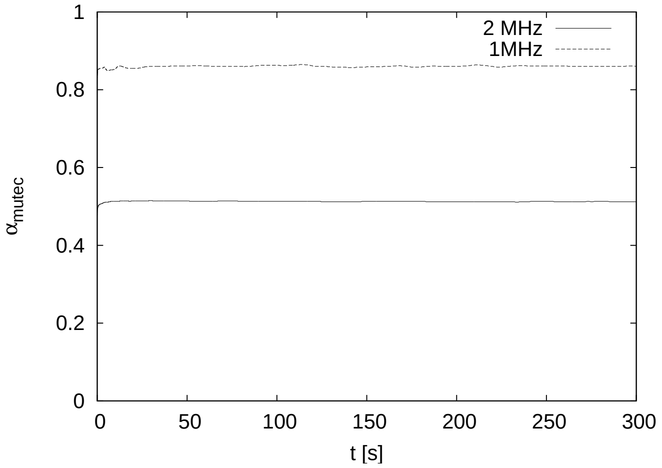

(a) Results of the measurements of the sample-holder of the *Mutec Penetration Dynamics Analyser* with a measurement frequency of 2 MHz and 1 MHz. It can be seen that the sample-holder reflects more ultrasonic intensity at 2 MHz.

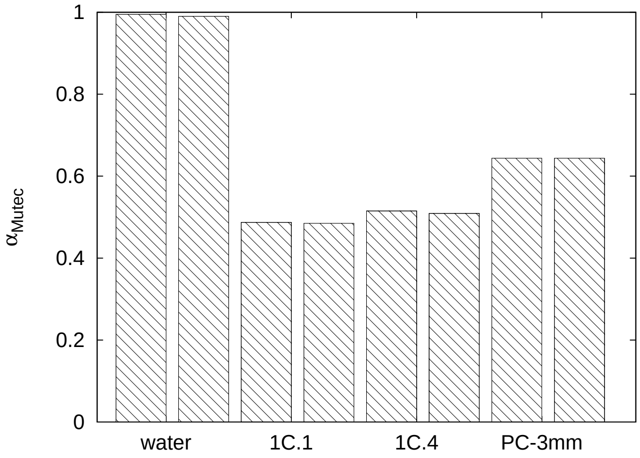

(b) Results of the measurements for two different sample-holders (1C.1 and 1C.4) and a plate made from polycarbonate. The polycarbonate plate has a thickness of 3 mm. The two sample-holders have a similar geometric size and are made from different materials. Sample-holder 1C.1 is made from polycarbonate and sample-holder 1C.4 is made from polypropylene.

Figure 4.8: Plot showing the accuracy and reproducibility of measurements with the sample-holder.

the *Mutec Penetration Dynamics Analyser* and a polycarbonate plate of 3 mm thickness are subjected to the same measurement procedure. The results are shown in **Figure 4.8(b)**. The variation of the results for the same sample-holder is due to the reproducibility of the measurement. Accuracy and reproducibility for this measurement set-up are good.

In order to compare results obtained by the model with measurements using the *Mutec Penetration Dynamics Analyser* α_{model} is plotted against α_{Mutec}. These results are shown for one sample-holder measured with different frequencies of ultrasound in **Figure 4.9(a)** and for measurements with one frequency but different materials in **Figure 4.9(b)**.

The results show a fairly good correlation. A linear regression $f(x) = a{\cdot}x$ for measurements with different frequencies gives a value of $a = 0.969 \pm 0.035$. This is very close to the ideal value of $a = 1$.

A similar result is obtained for the evaluation of different materials. The linear regression delivers $a = 1.044 \pm 0.034$ which is again very close to $a = 1$.

The factor influencing these results is to a large extent the accuracy of the determination of the thickness of the sample-holder. The variation in the transmission coefficient differs with the thickness of the plate, as can be seen in Figure 2.12. The material properties influence the result as well, but to a minor extent. As the material properties are taken from literature and are not verified by measurements, some uncertainty can arise here as well. Keeping this in mind, the results of the measurements fit the predicted results very well.

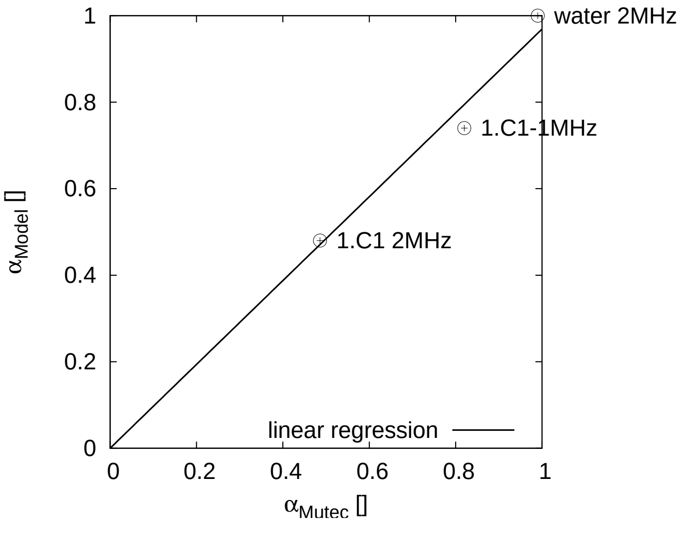

(a) Comparison of measurements with results obtained by the model. Results of measurements at 1 MHz and 2 MHz are plotted against predictions obtained by the model. The linear regression is of the form $f(x) = a \cdot x$ with $a = 0.969 \pm 0.035$.

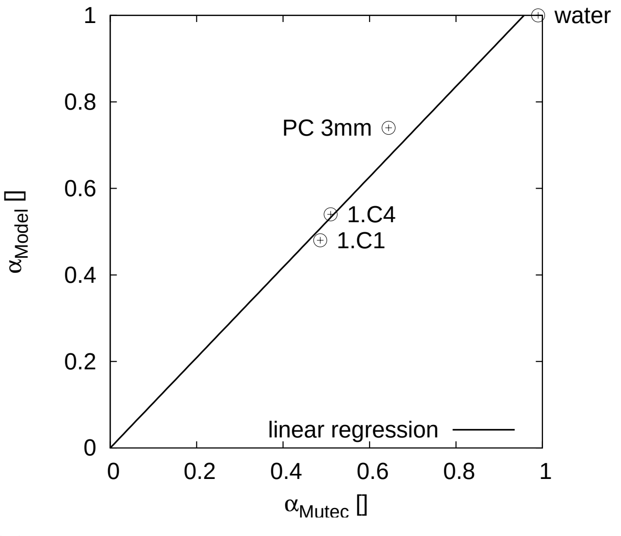

(b) Comparison of measurements with results obtained by the model. Results of measurements of different sheets of materials are plotted against predictions obtained by the model. The linear regression is of the form $f(x) = a \cdot x$ with $a = 1.044 \pm 0.034$.

Figure 4.9: Evaluation of measurement results with values predicted by the model for measurements with the sample-holder.

4.3 Measurements with membranes

4.3.1 Characterisation of membranes

To validate the model for the Mutec nucleopore membranes are used. Nucleopore membranes have a very close pore size distribution as can be seen in **Figure 4.10 (a)-(d)** All results for the evaluation are shown in **Table 4.2**.

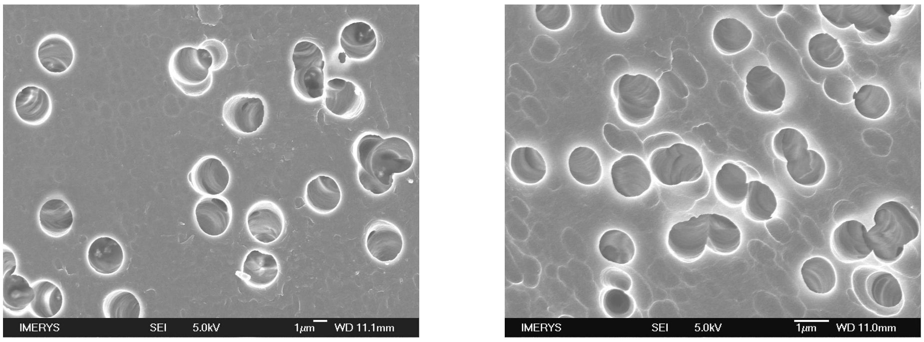

(a) Nominal pore diameter 3 µm

(b) Nominal pore diameter 1 µm

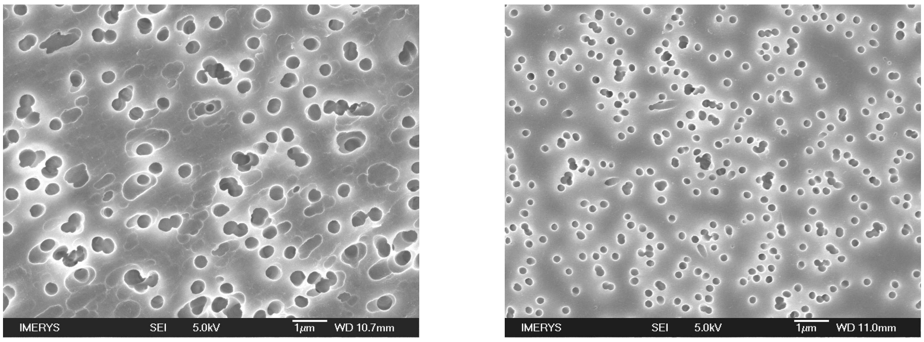

(c) Nominal pore diameter 0.4 µm

(d) Nominal pore diameter 0.2 µm

Figure 4.10: SEM pictures of the membranes used to evaluate the Mutec.

Four membranes with the nominal pore diameter of 0.2 µm, 0.4 µm, 1 µm and 3 µm are characterised. The results of measurements of the contact-angle of liquid drops on the surface of the membrane are given in **Table 4.3**. The liquids are water, 5%-ethanol and 10%-ethanol.

A special technique of embedding the membranes in Woods-metal and preparing cross-sections is applied to characterize the pores of the membrane. An example of a cross-section of an embedded membrane is given in Figure 3.17 on page 74. The surface of the pores in the membrane is smooth and the pores are straight. The centre line of the pores is usually different from the perpendicular of the surface of the membrane. This implies that the cross-section of a pore perpendicular to the path of the ultrasound varies across the surface of the membrane.

	nominal pore diameter of membrane			
	0.2 µm	0.4 µm	1 µm	3 µm
SEM pore diameter µm	0.23	0.35	1.03	2.49
SEM pore density 10^{12} 1/m^2	2.8	0.8	0.16	0.03

Table 4.2: The membranes used are evaluated with SEM techniques. The SEM pictures are shown for one resolution in Figure 4.10. For the SEM pore diameter only single holes are evaluated. This accounts for the slightly smaller pore diameters obtained by the SEM technique compared to the value given by the supplier. For the density all holes within a certain area are counted and divided by the area.

	nominal pore diameter of membrane			
ethanol concentration	0.2 µm	0.4 µm	1 µm	3 µm
0 %	87 °	75 °	85 °	80 °
5 %	71 °	62 °	76 °	64 °
10 %	65 °	63 °	63 °	62 °

Table 4.3: Results of the contact-angle measurements with different membranes and different water-ethanol mixtures The contact-angle of the 0.2 µm- and 1 µm-membrane is consistent. The contact-angle for the 3 µm- and 0.4 µm-membranes is decreasing for water and 5%-ethanol.

frequency of ultrasound	diameter of bubble 0.2 µm	1 µm	3 µm	4 µm
1 MHz	$1.11 \cdot 10^{-19}$	$1.82 \cdot 10^{-15}$	$2.04 \cdot 10^{-12}$	$1.83 \cdot 10^{-11}$
2 MHz	$1.79 \cdot 10^{-18}$	$3.39 \cdot 10^{-14}$	$8.65 \cdot 10^{-10}$	$4.46 \cdot 10^{-10}$

Table 4.4: Evaluation of the scattering cross-section ($[\,\mathrm{m}^2]$) due to resonance oscillation of the bubble. The resonance frequency is $f_r = \frac{3.26}{D/2}$ according to Equation (2.65) and is evaluated for air in water. With the resonance frequency the scattering cross-section according to Equation (2.81) can be calculated as a function of the frequency f.

frequency of ultrasound	diameter of sphere 0.2 µm	1 µm	3 µm	4 µm
1 MHz	$3.17 \cdot 10^{-27}$	$4.96 \cdot 10^{-23}$	$3.62 \cdot 10^{-20}$	$2.03 \cdot 10^{-19}$
2 MHz	$5.08 \cdot 10^{-26}$	$7.94 \cdot 10^{-22}$	$5.79 \cdot 10^{-19}$	$3.25 \cdot 10^{-18}$

Table 4.5: The scattering cross-section of a solid stationary sphere is calculated with the help of Equation (2.61). The resulting values are several magnitudes smaller than the results for the scattering cross-section of the bubble in resonance.

The scattering cross-section as a function of the particle size of different scatterers is evaluated and plotted in Figure 2.13 on page 29. The results for a spherical bubble scattering sound due to resonance scattering according to Equation (2.81), a spherical compressible sphere according to Equation (2.63), and a solid stationary sphere according to Equation (2.61) are compared. The physical properties of the bubble and the spheres are those of air, and the surrounding medium is water. It is obvious from this evaluation that the scattering due to resonance is the dominant mechanism for scattering.

A comparison of the results for the scattering cross-section obtained for air-bubbles in water and a solid sphere in water is listed in **Table 4.4** and **Table 4.5**. The diameters of the bubbles respectively the solid sphere are chosen to be equal to the different diameters of the pores in the membranes.

4.3.2 Measurements of membranes with the Mutec Penetration Dynamics Analyser

The *Mutec Penetration Dynamics Analyser* measures the change of ultrasonic intensity in relation to a calibration measurement. The measurements in this section are carried out after calibrating the device with the test-liquid and the sample-holder including the two-sided sticky tape. The attenuation value measured is therefore only an indication for the influence of the different membranes on the detected signal. Membranes with 3 µm, 1 µm, 0.4 µm and 0.2 µm pore-diameter are evaluated. The contact-angle measurements for the test-liquids on the membrane's surface result in values smaller than 90 °. This means that capillary suction occurs. The process of capillary suction described by the modified Lucas-Washburn-Equation (3.84) is too fast to be detected by the *Mutec Penetration Dynamics Analyser*. The liquid penetrates into the pores of the membrane and the pressure in the remaining gas volume is increased. This leads to gas molecules being transferred across the phase boundary and transported via diffusion into the bulk of the liquid. Consequently the gas volume will change and due to this the scattering cross-section of the gas in the pore will change as well. This is described by Equations (2.140), (2.84) and (2.86) and is plotted in Figure 3.26 on page 87. Larger scattering cross-sections will give smaller values for α_{Mutec} as less ultrasound is detected at the Receiver.

Results of measurements using 3 µm-, 1 µm-, 0.4 µm- and 0.2 µm-membranes with different test-liquids are shown in **Figure 4.11, Figure 4.12** and **Figure 4.13**. The test-liquids used are water, 5%- and 10%-ethanol-water blends.

A logarithmic scale is chosen for the plots to be able to evaluate small time-scales. In most of the cases the curve remains constant or slightly inclining before the slope becomes steeper, and eventually the value levels out to one. In all cases the curve for the 0.2 µm-membrane is constant. It can also be observed that the point where the slope of the curve increases occurs sooner for pores of smaller diameter. The change in the scattering cross-section of the 0.4 µm-membrane is closer to the change in the scattering cross-section of the 1 µm-membrane as it is for 1 µm-membrane compared to the 3 µm-membrane. All curves eventually level out at a value of one.

The results are now put into the context of the earlier calculations. Starting with the simplest curves obtained for the 0.2 µm-membrane. The diameter of the pores is obviously too small for scattering due to resonance. This can be seen in Figure 3.21 on page 81. Taking this scattering cross-section and putting it into relation to the diameter of the pore it becomes obvious that the scattering ability of the 0.2 µm-membrane is about 1600 times smaller compared to the 5 µm. In addition to this, the smaller diameter

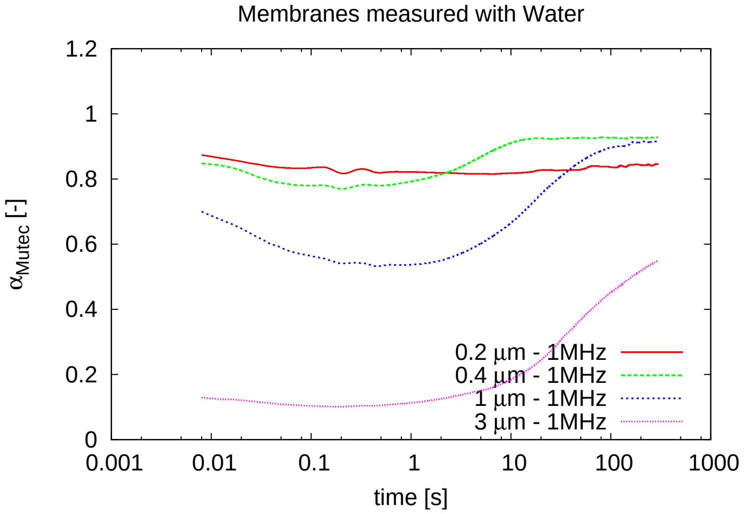

(a)

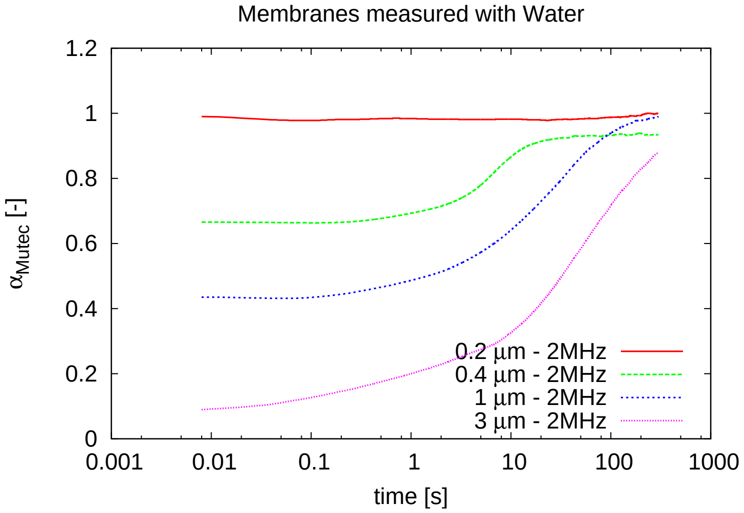

(b)

Figure 4.11: Measurements with water. The value measured is the pseudo-attenuation coefficient as it is given by the Mutec. The pseudo-attenuation coefficient α_{Mutec} is a function of the settings of the Mutec during calibration and the settings of the device as well as the detected pressure during the measurement.

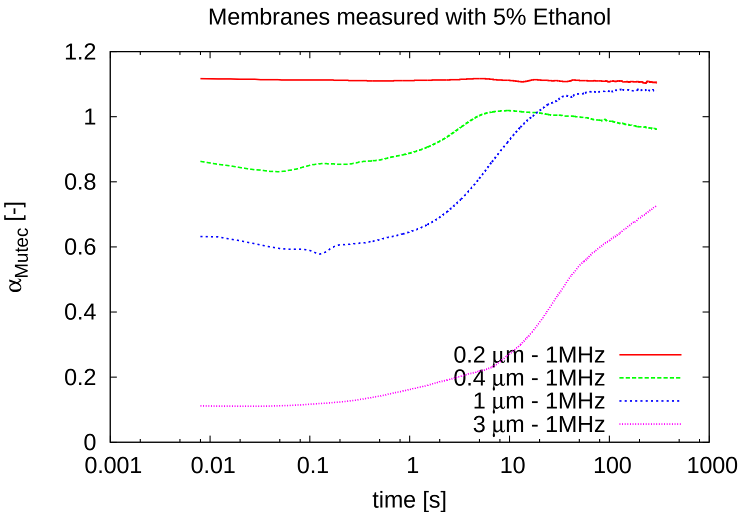

(a)

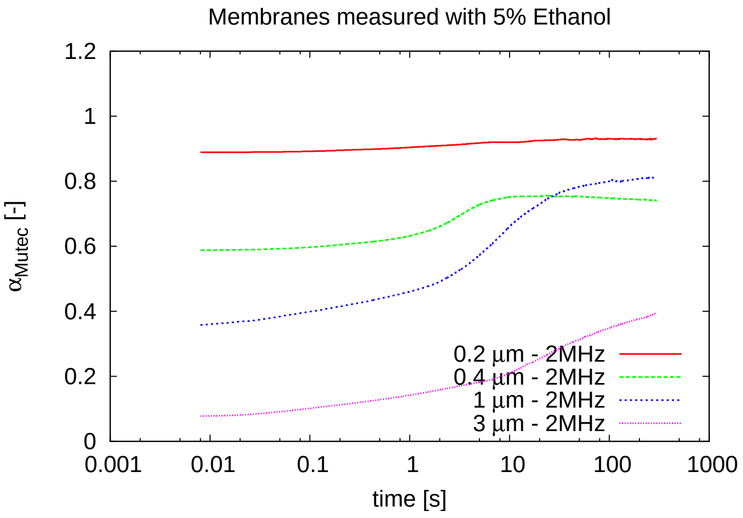

(b)

Figure 4.12: Measurements with 5 wt-% ethanol. The value measured is the pseudo-attenuation coefficient as it is given by the Mutec. The pseudo-attenuation coefficient α_{Mutec} is a function of the settings of the Mutec during calibration and the settings of the device as well as the detected pressure during the measurement.

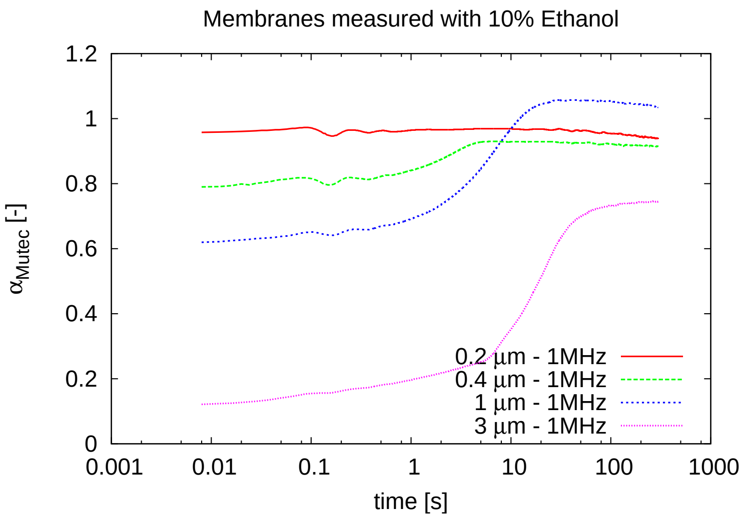

(a)

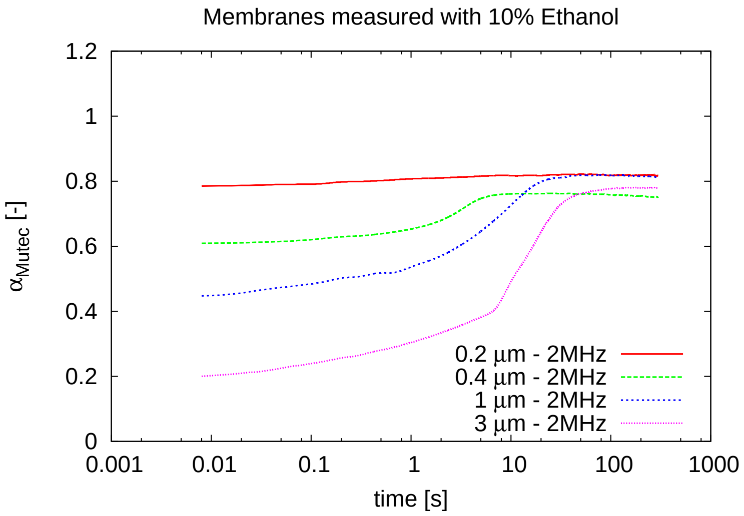

(b)

Figure 4.13: Measurements with 10 wt-% ethanol. The value measured is the pseudo-attenuation coefficient as it is given by the Mutec. The pseudo-attenuation coefficient α_{Mutec} is a function of the settings of the Mutec during calibration and the settings of the device as well as the detected pressure during the measurement.

leads to an increased pressure in the pore due to the curved surface. This leads to a larger imbalance of the air solved in the water and the partial pressure in the gas phase resulting in an increased flux of gas molecules into the liquid phase. Contrary to this the initial penetration depth of the liquid as given by the modified Lucas-Washburn-Equation (2.103) is smaller compared to the other membranes. This fact is outweighed by the small scattering cross-section and the increased diffusion. As a result the *Mutec Penetration Dynamics Analyser* can neither detect the pores nor the dynamic changes in the pores of the membrane.

The shape of the curves obtained by the measurement of the remaining membranes can again be explained with the help of Figure 3.21. A small α_{Mutec}-value means that only little ultrasonic intensity is detected at the receiver. A large value for the scattering cross-section means that the ability of the pore to scatter ultrasonic intensity is large. Hence if the scattering cross-section is large the α_{Mutec}-value will be low. The graph for the scattering cross-section can roughly divided into two areas. One area where the scattering cross-section remains on a more or less constant level especially for short times and a second area where the scattering cross-section declines. A simplified evaluation is shown in Figure 4.14(a).

A similar evaluation of the curves to determine the point where the slope changes is undertaken and exemplified in Figure 4.14(b) for the 3 µm-membrane. Two linear interpolations using only a part of the data of the graph are undertaken. The time displayed on the abscissa at the intersection of the two lines is taken.

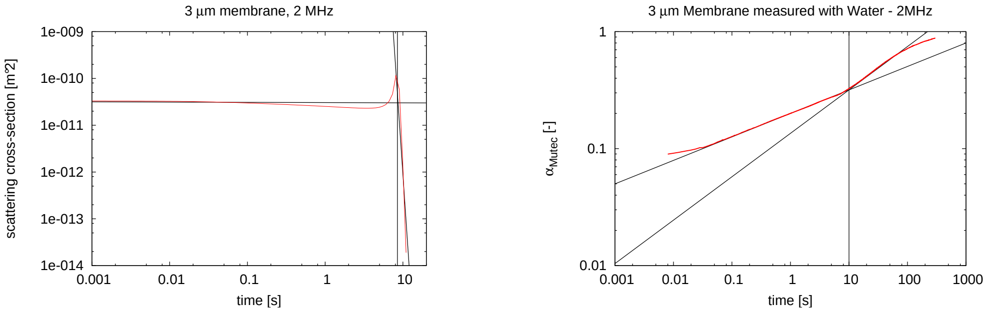

(a) Simplification of the scattering cross-section.

(b) Simplification of the α_{Mutec}-measurements.

Figure 4.14: Simple determination of the point where the slope of the scattering cross-section and the α_{Mutec}-value changes.

The results of the evaluation of the time when the slope of the scattering cross-section respective the α_{Mutec}-value changes is shown for the different membranes in Table 4.6. It can be seen that the model predicts these times fairly well. The larger the pore size becomes the larger is the transition

pore size	model	measurement
0.4 µm	2.0 s	2 s
1 µm	3.5 s	3 s
3 µm	9.0 s	8 s

Table 4.6: Comparison of the time when the slope of the scattering cross-section changes for the calculation of the model with the time when the α_{Mutec}-value of the measurement changes. Membranes with different pore sizes are evaluated.

region between the two slopes. This feature is found in the values measured as well as in the values calculated from the model. The broad transition region complicates the determination of the exact time for the change of the slope.

5 Future Prospects

The use of ultrasound to measure the dynamic penetration of liquids into pores is described in the previous sections. For materials with well defined properties and simple geometries the theory is able to predict measurement results. However, most materials used in industrial processes where interaction of porous materials with liquids is of particular interest are more complicated. Paper, for example, is a composition of different materials, i.e. fibres, fillers, starch, retention aid, forming a porous network with convex and concave surfaces having regions of varying surface energies. If only the sizes of the pores are taken into consideration, one would assume that an approximation for the results is a superposition of curves for the occurring pore-sizes.

Some measurements with coated and uncoated papers of different qualities are shown in **Figure 5.1**, **Figure 5.2**, **Figure 5.3** and **Figure 5.4**.

Obviously the shapes of the curves measured show that this assumption is not valid. For the curves decrease with increasing time. Although they level out to form a plateau, the value measured is by far smaller than the value for the membrane. A closer look shows that the values eventually rise but only after a long time. If the measurements are continued beyond the time of 100 s, it is possible that the curves level out at a constant value close to that of the sample-holder.

For the copy paper in Figures 5.3(a) and 5.3(b) there is no levelling out, instead the curves continuously decrease during the observed time-frame.

The hypothesis for the explanation of the curves in Figure 5.1, Figure 5.2 and Figure 5.3 is the assumption that after the initial contact with water, areas of enclosed air are generated due to capillary suction. These areas act as scattering centres reducing the attenuation coefficient. The porous structure of the paper is rather complex as fibres form a network of intersecting pores. Areas of convex and concave surfaces as well as areas of different wettability influence the capillary suction. In contrast to the pores of the membrane the network is not sealed. This leads to a potential opportunity for the air to escape from the paper structure. This may also lead to an increased time for the pressure build-up within the gas phase. If the pressure build-up is slower, the imbalance between the pressure of the gas and the concentration of the gas in the liquid and subsequently the diffusion

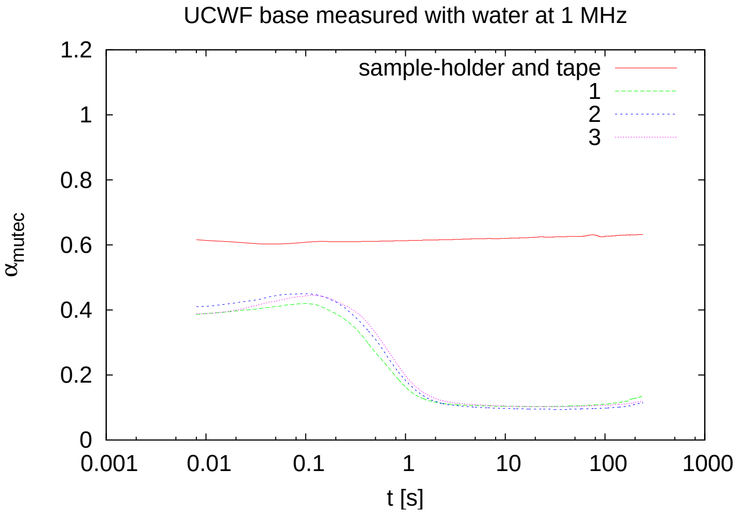

(a)

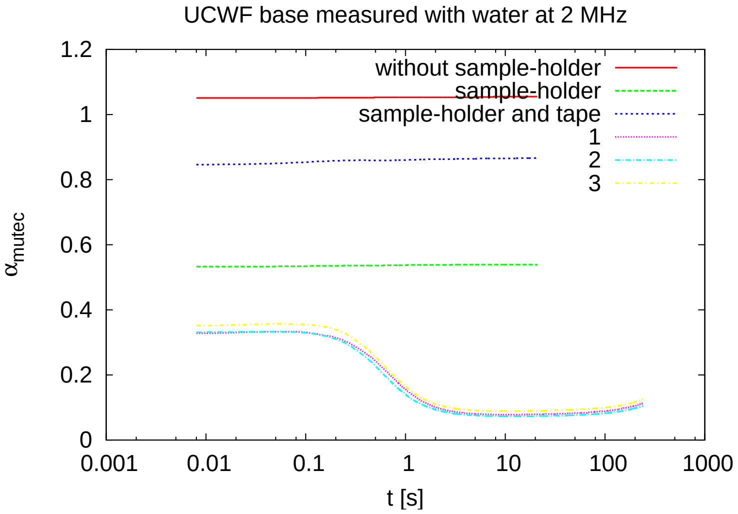

(b)

Figure 5.1: Measurements of the pseudo-attenuation coefficient of an uncoated wood-free paper in water.

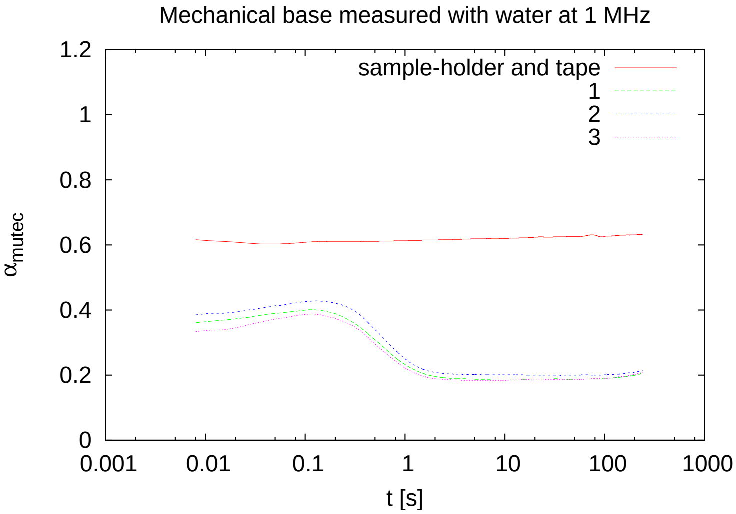

(a)

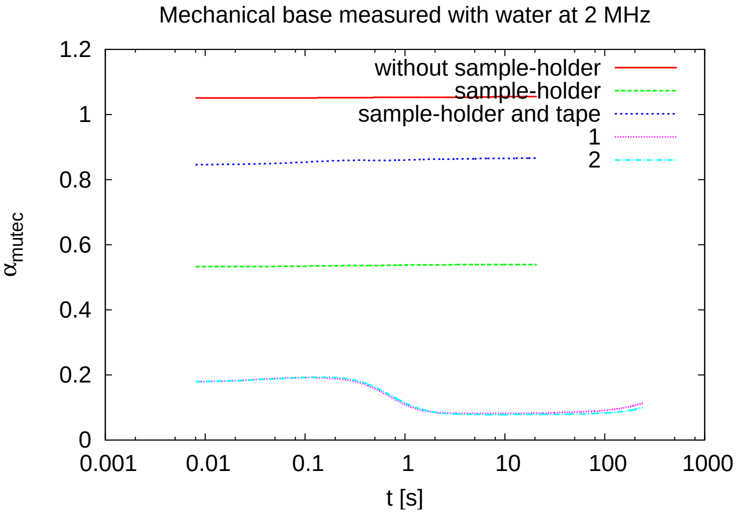

(b)

Figure 5.2: Measurements of the pseudo-attenuation coefficient of a mechanical base-paper in water.

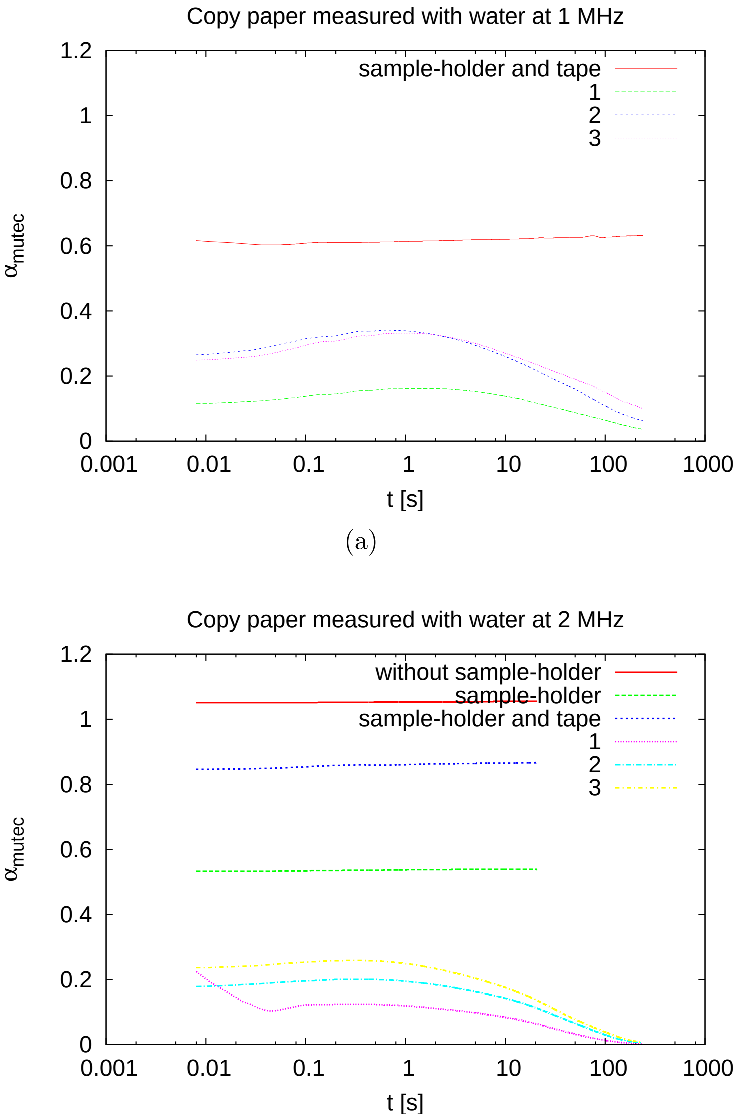

(a)

(b)

Figure 5.3: Measurements of the pseudo-attenuation coefficient of copy paper in water.

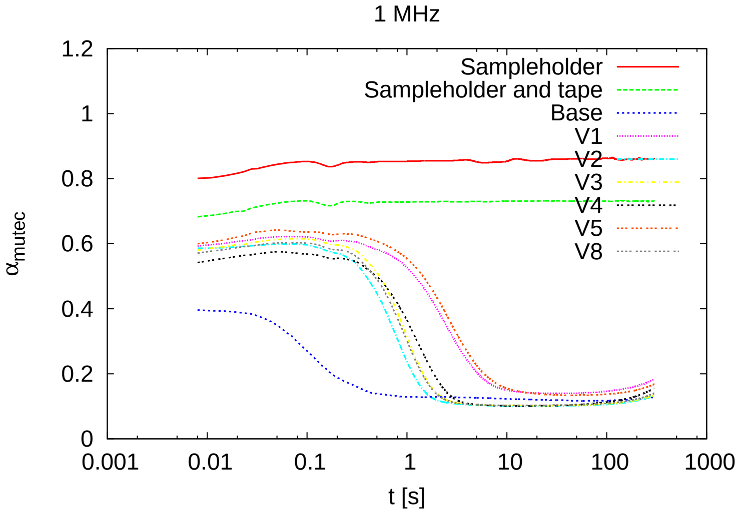

(a) 1 MHz

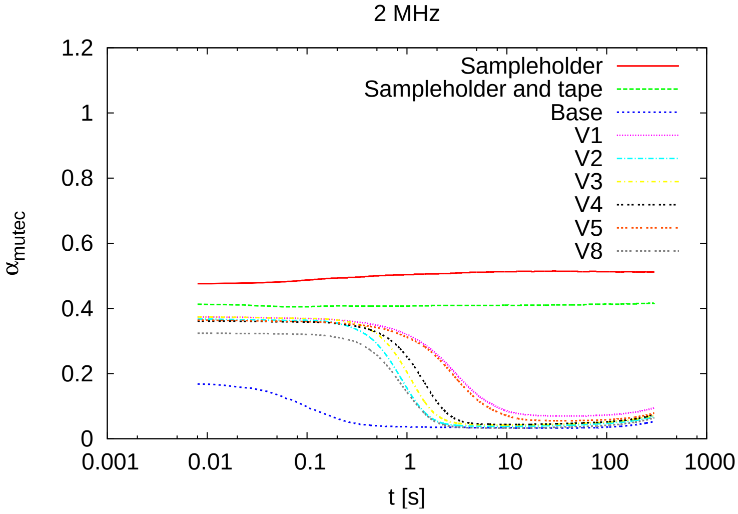

(b) 2 MHz

Figure 5.4: Measurements of different papers. The paper consists of the same base paper and is coated with different coating colour formulations using a high speed pilot coater. The pore structure of the coated paper is different due to differences in the pigments used in the coating colour. The main difference observed is the difference between base sheet and coated sheet. Within the set of coated papers mercury-porosimetry measurements show that V1 has the largest number of small pores.

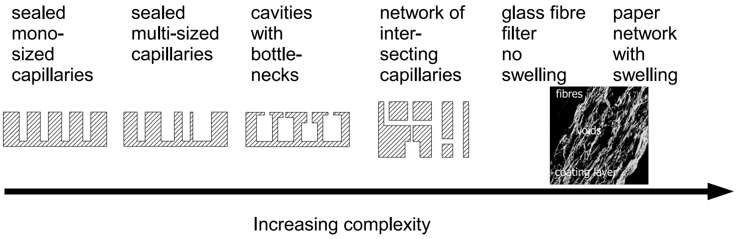

Figure 5.5: Paper is a complex structure and the interaction with aqueous liquids also leads to dynamic changes of this structure. For the validation of models it is necessary to undertake measurements with model substances. The complexity of model substrates can vary significantly.

change. In addition to this, processes of swelling fibres change the fibre network. New scattering centres occur and the size of the scattering centres changes, leading to a variation in the scattering cross-section of the paper sample.

Although for mono-sized capillaries the theory predicts the results measured, further efforts are necessary to describe the penetration into complex structures.

For the further research **Figure 5.5** might be a guide. In this thesis membranes with mono-sized pores are evaluated. The next step could be done by evaluating a mixture of pores, where the number of pores as well as their sizes are varied. A quite simple set-up for this procedure is shown in **Figure 5.6**. As the measurement conditions are radially symmetric the circular measurement area of the sample-holder could be divided into segments of various sizes, each segment having different pore sizes and different numbers of pores. The resulting measurement curves might be interpreted as a superimposition of the individual curves belonging to the membranes with the sizes of the segments being a weighting for the final curve. One could eventually try to draw conclusions from the resulting curve to the pore-size-distribution of the sample. One way to reduce the results shown in Figures 4.11, 4.12 and 4.13 could be by concentrating the curve at the starting level, the point where the curve starts rising as well as its slope and at its final level, and assessing how these values are influenced by the corresponding values of the curves for the respective membranes, and if curves for paper are measured, to judge the quality of paper.

Another step to gain more complexity could consist in trying to replace the cylindrical capillaries by bottle-necked cavities as shown in **Figure 5.7(a)**. This might be of interest as Figure 1.1 indicates that the cavities are of much larger extent compared to the pores of the surface leading to these cavities. Doing so the calculation of the dynamic penetration has to be modified so that methods used for cylindrical capillaries are adapted to this situation. This is possible for the theory but a validation is more difficult

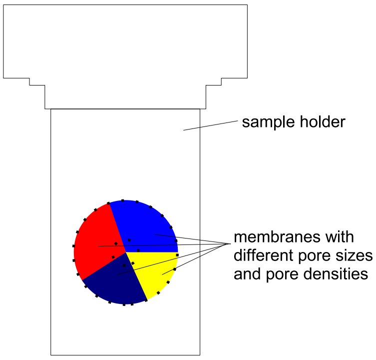

Figure 5.6: For the evaluation of different pore-size-distribution the sample-holder could be prepared with different membranes.

as model substrates have to be found. By etching the surface of a sample-holder cavities could be generated and covered by membranes as shown in **Figure 5.7(b)**.

Increasing the complexity of the model intersections of pores could be implemented but a suitable material for validation has still to be found.

Another approach could consist in reducing the complexity of paper as a substrate by using glass-fibre-filters in combination with appropriate liquids. In contrast to paper-water-interaction where swelling occurs, these filters have the advantage of avoiding dynamic changes of the structure during the penetration process.

Of course the complexity of papers can be varied from uncoated papers to single or multiple coated papers. The technique using Woods metal as e.g. used in Figure 3.17 on page 74 for membranes could be developed to obtain more information about the paper structure.

It has to be emphasised here again that better ways of calibrating the mea-

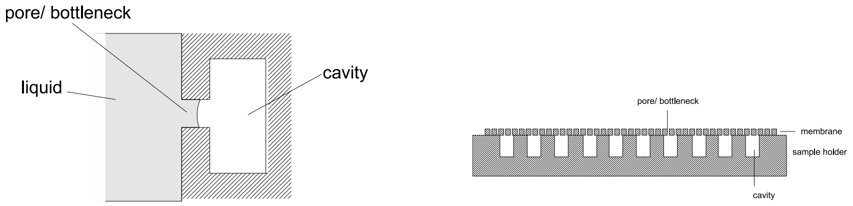

(a) Sketch of a cavity with a small bottleneck like entrance. The bottle-necked cavity can be describe in analogy to a sealed capillary.

(b) Cross-section of a specially prepared sample-holder for the evaluation of bottle-necked cavities.

Figure 5.7: For the evaluation bottle-necked cavities the model as well as the sample-holder need adaptation.

surement device as well as improving the way results are reported are an absolute necessity for a scientific use of this device (see Section 3.1).

Lately a modification of the measurement device has been presented (PDA C.02 Module PEA [14]). The Receiver is moved onto the sample-holder and it is split into an array of small Receivers which might allow to judge the homogeneity of the material measured with the device. Due to the position of the Receiver on the sample-holder it is more difficult to calculate the model. For the Receiver is now situated closer to the near-field-distance. Therefore it is located in a region of the sound-field where it is more difficult to calculate properties of the sound-field. It has to be verified whether the model developed in this thesis can be adjusted to the new measurement set-up.

In this thesis only solutions and pure liquids are used. In order to find a model for technical fluid containing particles it could be useful to extent the research to dispersions and suspensions. The particles in the dispersions and suspensions act as scattering centres. Model substances for this development could be medical ultra-sound contrast agents of well defined particles. The result could be a model for technical liquids as they are used for paper coating. This enables to evaluate results obtained by the measurement device when paper is measured using a coating colour as test-liquid.

To summarise further research should focus on

- the integration into the model of a pore-size-distribution, the pore shape, the interconnectivity of the pores and the change of the fibres during wetting,
- developing a model of the modified measurement device with a higher resolution of the Receiver,
- the adaptation of dispersions and suspensions into the model.

6 Summary

The dynamics of liquid penetration into porous networks is important for many processes during the production and printing of paper. One commercially available device to measure liquid penetration indirectly uses the change of ultrasonic attenuation when a specimen is brought into contact with liquid.

In order to interpret results obtained by this device the generation and detection of ultra-sound are modelled as functions of the Sender and the Receiver, their material properties, their diameters and the geometry of the measurement chamber. In addition, the use of a sample-holder and of a special steel insert for measurements are covered. The efforts are mainly focussed on the spread, attenuation, reflection and scattering of ultra-sound.

Further a model for the ultrasonic attenuation of pores partly filled with liquid and partly filled with gas is derived. The penetration dynamics into pores is then developed as a function of their size and shape, the material, and the solid-liquid interaction. Both aspects are combined to describe the time-dependent change in ultrasonic attenuation when liquid penetration takes place.

Results predicted by the model are validated by several measurements, including the validation of the measurement chamber with different solutions of manganese-sulfate, the sample-holder with different plastics, and the steel-insert using ethanol-water blends. A nucleopore membrane, characterized by fairly cylindrical pores of well defined sizes, is used to validate the penetration dynamics.

The measurements with liquids show a good correlation of measurements with the values predicted by the model. The correlation of the concentration of manganese-sulfate and its ultrasonic attenuation is confirmed by the model. The physical properties of ethanol-water blends vary largely with the concentration. This can also be seen in the measurement results.

The results with the sample-holder fit well and indicate a considerable influence of the sample-holder's thickness on the results.

In the measurements with the membranes it becomes obvious that the capillary suction, as described by the Lucas-Washburn- or Bosanquet-equation, is important for the initial penetration into the pores. However this process is too fast to be measured directly, as the device can record values only after an initial delay of 8 ms.

As a consequence of the capillary suction and due to the fact that the pores are sealed at one side, the pressure in the pores increases, which leads to an imbalance between the gas-pressure and the concentration of the gas dissolved in the liquid. Consequently, gas is transferred from the gas-phase into the liquid, and the gas volume is reduced. Hence the pores are filled with liquid.

Additional measurements with paper show that they can be interpreted on the basis of the model. But for a quantitative description there is still a lack of precise information about the paper structure, the distribution of convex and concave surfaces, and the local distribution of the wettability.

Bibliography

[1] ASTM d5455-93 standard test method for short term liquid sorption into paper (bristow technique). American Standard Test method, 2003.

[2] P. K. Baird and C. E. Irubesky. *Tech Assoc. Papers*, 13:274–277, 1930.

[3] R. Beltz. emco gmbh. URL `www.emco-leipzig.com`.

[4] Jack Blitz. *Ultrasonics: Methods and applications.* Butterworths Ltd, 1971.

[5] C. H. Bosanquet. On the flow of liquids into capillary tubes. *Philos. Mag. Ser.*, 6(45):525–531, 1923.

[6] J. Crank. *The mathematics of diffusion.* Oxford University Press, London, 1970.

[7] G. D'Arrigo and A. Paparelli. Sound propagation in water-ethanol mixtures at low temperatures. iI. dynamical properties. *J. Chem. Phys*, 12:7687–7697, 1998.

[8] N. de Jong, L. Hoff, K. Skotland, and N. Bom. Absorption and scatter of gas filled microspheres: theoretical considerations and some measurements. *Ultrasonics*, 30:95–103, 1992.

[9] Andrei S. Dunkhin and Philip J. Goetz. Influence of chemical composition on the acoustic properties of homogenous liquids. Newsletter, 03 2001. URL `http://www.dispersion.com/pages/newsletter/articles/Newsletter9.pdf`.

[10] Jan E. Elftonson and Göran Ström. Penetration of aqueous solutions into models for coating layers. Technical report, Institute for Surface Chemistry, Forest Production Section, BOX 5607, S-114586 Stockholm, Sweden, 1995.

[11] Dale Ensminger. *Ultrasonics.* Marcel Dekker Inc., New York, Basel, 1991.

[12] d. L. Folds. Experimental determination of ultrasonic wave velocities in plastics, elastomers, and synthetic foam as a function of temperature. *J. Acoust. Soc. Am.*, 56(4), 10 1974.

[13] Gerhard Gabriel. *Meßtechnische Erfassung der Wechselwirkungen zwischen Flüssigkeiten und Papieren mittels Ultraschall.* PhD thesis, Technische Universität Graz, Februar 1999.

[14] Emtec Electronic GmbH. Penetrations dynamik analysator emtec pda.c 02, module pea print evenness analyzer. internet, 11 2006. URL `http://www.emtec-papertest.com/deutsch/history.html`.

[15] A. Goldstein, D. R. Gandhi, and W. D. O'Brien JR. Diffraction effects in hydrophone measurements. *IEEE Transactions on Ultrasonics Ferroelectics and Frequency control*, 45(4):972–979, july 1998.

[16] G. Grüner. Personal communication - emtec electronics, 2002.

[17] G Grüner. e-mail communication - emtec electronics, 02 2003.

[18] Miklós Kanzamár. *Simulation der Trocknung gestrichener Papiere*. PhD thesis, TU Darmstadt, Darmstadt, 2004.

[19] Josef Krautkrämer and Herbert Krautkrämer. *Werkstoffprüfung mit Ultraschall*. Springer-Verlag, Berlin Heidelberg New York London Paris Tokyo, 5te edition, 1986.

[20] Heinrich Kuttruff. *Akustik*. S. Hirzel Verlag, 2004.

[21] T. G. Leighton. *The Acoustic Bubble*. Academic Press, London, 1994.

[22] Veniamin G. Levic. *Physicochemical Hydrodynamics*. Prentice Hall, London, 1962.

[23] Richard Lucas. Über das Zeitgesetz des kapillaren Aufstiegs von Flüssigkeiten. *Kolloid Z.*, 23:15–22, 1918.

[24] G.P. Matthews. Computer modelling of fluid permeation in porous coatings and paper - an overview. *Nordic Pulp and Paper Research Journal*, 2000.

[25] David Julian Mc Clements. Ultrasonic characterisation of emulsions and suspensions. *Advances in Colloid Interface Science*, 37:33–72, 1991.

[26] Douglas L. Miller. Experimental investigation of the response of gas filled micropores to ultrasound. *J. Acoust. Soc. Am.*, 71(2):471–476, 1982.

[27] Douglas L. Miller and Wesley L. Nyborg. Theoretical investigation of the response of gas-filled micropores and cavitation nuclei to ultrasound. *J. Acoust. Soc. Am..*, 73(5):1537–1544, 1983.

[28] M. Minnaert. On musical air bubbles and sounds of running water. *Philosophical Magazine*, 16:235–248, 1933.

[29] D. Ohndorf. e-mail communication - emtec electronic, 03 2003.

[30] S. A. Parke and G. G. Birch. Solution properties of ethanol in water. *Food Chemistry*, 67:241–246, 1999.

[31] P. Petong, R. Pottel, and U. Kaatze. Water-ethanol mixtures at different compositions and temperatures. A dielectric relaxation study. *J. Phys. Chem.*, 104:7420–7428, 2000.

[32] T. Pietikäinen. *Ultrasonic measurement of entrained air in papermaking furnish*. PhD thesis, University of Oulu, Department of Electrical Engineering, 1992.

[33] Janet S. Preston. *Influence of coating structure on the print gloss of coated paper surfaces*. PhD thesis, University of Bristol, November 2001.

[34] Janet S. Preston, Matias Daun, Chris Nutbeem, and Andrew Jones. Attaining print performance through pigment engineering. *Wochenblatt für Papierfabrikation*, 5:252–265, march 2000.

[35] Lothar Prof. Dr. Götsching and Casimir Dr. Katz, editors. *Papier-Lexikon*. Deutscher Betriebswirte-Verlag GmbH, 1999.

[36] John William Strutt Rayleigh. *Theory of Sound*. Macmillan, London, 1877.

[37] P. Salminen. Studies of water transport in paper during short contact times. Technical report, Laboratory of Paper Chemistry, Department of Chemical Engineering, Åbo Akademi, 1988.

[38] Emil J. Samuelsen, Per-Johan Houen, Øyvind Weiby Gregersen, Torbjørn Helle, and Carsten Raven. Three-dimensional imaging of paper by use of synchrotron x-ray microtomography. *Journal of Pulp and Paper Science*, 27 (2):50–53, 2001.

[39] Ida-Maria Sintorn, Stina Svensson, Maria Axelsson, and Gunilla Borgefors. Segmentation of individual pores in 3d paper images. *Nordic Pulp and Paper Research Journal*, 20(3), 2005.

[40] Vladimir. A. Sutilov. *Physik des Ultraschalls*. Springer Verlag, 1984.

[41] Edward W Washburn. The dynamics of capillary flow. *The Physical Review*, 17:273–283, 1921.

[42] Emmerich Wilhelm, Rubin Battino, and Robert J. Wilcock. Low-pressure solubility of gases in water. *Chemical Reviews*, 77:219–262, 1977.

List of Figures

List of Tables

A Mathematical derivations

A.1 Derivation of the pressure along the centre line

Start point is the Rayleigh formula, Equation (2.15)

$$p(d,t) = \frac{i \cdot \omega \cdot \rho}{2 \cdot \pi} \cdot e^{\frac{i \cdot \omega \cdot t}{2 \cdot \pi}} \int\limits_S v_{max,0} \cdot \frac{e^{-i \cdot k \cdot d}}{d} \qquad \text{(A.1).}$$

The distance d between an observer (index o) and a point on the Sender (index s)

$$d = \sqrt{r_o^2 + r_s^2 + z_o^2 - 2 \cdot z_o \cdot z_s + z_s^2 - 2 \cdot r_o \cdot r_s \cdot \cos\left(\varphi_o - \varphi_s\right)} \qquad \text{(A.2)}$$

can be reduced for an observer on the centre line, as the radius of the observer r_o is then always zero. If the Sender is at $z_s = 0$, the result for the distance d is

$$d = \sqrt{r_s^2 + z_o^2} \qquad \text{(A.3).}$$

The use of cylindrical coordinates for the Rayleigh formula requires the inclusion of the jacobian determinant. The wave number k can be replaced by $k = 2 \cdot \pi / \lambda$ with the wavelength $\lambda = c/f$, a function of the velocity of sound, and the frequency $f = \omega/(2 \cdot \pi)$. The integral over the area S can then be written as:

$$p(z_o,t) = \frac{i \cdot \omega \cdot \rho}{2 \cdot \pi} \cdot e^{\frac{i \cdot \omega \cdot t}{2 \cdot \pi}} \int\limits_0^R \int\limits_0^{2\pi} r_s \cdot v_{max,0} \cdot \frac{e^{-i \cdot k \cdot \sqrt{r_s^2 + z_o^2}}}{\sqrt{r_s^2 + z_o^2}} \, d\,\varphi_s \, d\,r_s \qquad \text{(A.4).}$$

Taking just the real part gives:

$$Re\left(p(z_o)\right) = \int\limits_0^R \int\limits_0^{2\pi} - \frac{r s \, v \, \rho \, \omega \, \sin\left(\frac{\omega}{2}\left(\frac{t}{\pi} - \frac{2\sqrt{r_s^2 + z_o^2}}{c}\right)\right)}{2\,\pi\,\sqrt{r_s^2 + z_o^2}} \, d\,\varphi_s \, d\,r_s \qquad \text{(A.5).}$$

The pressure is now independent of φ_s and integration gives

$$p(z_o,t) = c \cdot v \cdot \rho \cdot \left(\cos\left(\frac{t\,\omega}{2\,\pi} - \frac{\omega\,\sqrt{z_o^2}}{c}\right) - \cos\left(\frac{t\,\omega}{2\,\pi} - \frac{\omega\,\sqrt{\frac{D^2}{4} + z_o^2}}{c}\right)\right) \qquad \text{(A.6)}$$

This is almost Equation (2.16), except for the factor 2 which arises from the fact that the source radiates only into one half room. This equation is still dependent on the time t. In order to find the maximum pressure which may occur at any time, the envelope function of Equation (2.16) has to be determined with regard to the time t, as shown in the next section.

A.2 Derivation of the envelope function

$$p(z_o,t) = v\cdot c\cdot\rho\cdot\left(\cos\left[\frac{t\cdot\omega}{2\cdot\pi} - \frac{\sqrt{z_o^2}\cdot\omega}{c}\right] - \cos\left[\frac{t\cdot\omega}{2\cdot\pi} - \frac{\sqrt{\frac{D^2}{4}+z_o^2}\cdot\omega}{c}\right]\right) \tag{A.7}$$

The maxima and minima with regard to the time t needs to be determined, hence the derivation is calculated,

$$\frac{\partial p(z_o,t)}{\partial t} = \frac{v\cdot c\cdot\rho\cdot\omega}{2\cdot\pi}\cdot\left(\sin\left[\frac{1}{2}\left(\frac{t\cdot\omega}{\pi} - \frac{\sqrt{\frac{D^2}{4}+z_o^2}\cdot\omega}{c}\right)\right] - \sin\left[\frac{1}{2}\left(\frac{t\cdot\omega}{\pi} - \frac{\sqrt{z_o^2}\cdot\omega}{c}\right)\right]\right) \tag{A.8}$$

set to 0,

$$\frac{\partial p(z_o,t)}{\partial t} = 0 \tag{A.9}$$

divided by $\frac{v\cdot c\cdot\rho\cdot\omega}{2\cdot\pi} > 0$,

$$\sin\left[\frac{1}{2}\left(\frac{t\cdot\omega}{\pi} - \frac{\sqrt{\frac{D^2}{4}+z_o^2}\cdot\omega}{c}\right)\right] = \sin\left[\frac{1}{2}\left(\frac{t\cdot\omega}{\pi} - \frac{\sqrt{z_o^2}\cdot\omega}{c}\right)\right] \tag{A.10}$$

simplified using trigonometric functions,

$$\cos(x\pm y) = \sin(x)\cos(y) \pm \cos(x)\sin(y) \tag{A.11}$$

to get

$$\sin\left[\frac{t\cdot\omega}{2\cdot\pi}\right]\cdot\cos\left[\frac{\sqrt{\frac{D^2}{4}+z_o^2}\cdot\omega}{2\cdot c}\right] - \cos\left[\frac{t\cdot\omega}{2\cdot\pi}\right]\cdot\sin\left[\frac{\sqrt{\frac{D^2}{4}+z_o^2}\cdot\omega}{2\cdot c}\right] = \tag{A.12}$$

$$\sin\left[\frac{t\cdot\omega}{2\cdot\pi}\right]\cdot\cos\left[\frac{\sqrt{z_o^2}\cdot\omega}{2\cdot c}\right] - \cos\left[\frac{t\cdot\omega}{2\cdot\pi}\right]\cdot\sin\left[\frac{\sqrt{z_o^2}\cdot\omega}{2\cdot c}\right]. \tag{A.13}$$

The Equation is rearranged,

$$\frac{\sin\left[\frac{t\cdot\omega}{2\cdot\pi}\right]}{\cos\left[\frac{t\cdot\omega}{2\cdot\pi}\right]} = \frac{\sin\left[\frac{\sqrt{z_o^2}\cdot\omega}{2\cdot c}\right] - \sin\left[\frac{\sqrt{\frac{D^2}{4}+z_o^2}\cdot\omega}{2\cdot c}\right]}{\cos\left[\frac{\sqrt{z_o^2}\cdot\omega}{2\cdot c}\right] - \cos\left[\frac{\sqrt{\frac{D^2}{4}+z_o^2}\cdot\omega}{2\cdot c}\right]} \tag{A.14}$$

simplified using more trigonometric functions and rearranged

$$\tan\left[\frac{t\cdot\omega}{2\cdot\pi}\right] = -\cot\left[\frac{\omega\cdot(2\cdot\sqrt{z_o^2}+\sqrt{\frac{D^2}{+}4\cdot z_o^2})}{4\cdot c}\right] \tag{A.15}$$

$$\tan\left[\frac{t\cdot\omega}{2\cdot\pi}\right] + \cot\left[\frac{\omega\cdot(2\cdot\sqrt{z_o^2}+\sqrt{\frac{D^2}{+}4\cdot z_o^2})}{4\cdot c}\right] = 0 \qquad \text{(A.16).}$$

Expanding gives

$$\frac{\cos\left[\frac{\sqrt{z_o^2}\cdot\omega}{2\cdot c}\right]\cdot\cos\left[\frac{\sqrt{D^2+4\cdot z_o^2}\cdot\omega}{2\cdot c}\right]-\sin\left[\frac{\sqrt{z_o^2}\cdot\omega}{2\cdot c}\right]\cdot\sin\left[\frac{\sqrt{D^2+4\cdot z_o^2}\cdot\omega}{2\cdot c}\right]+}{}\ldots \tag{A.17}$$

$$\ldots\frac{\sin\left[\frac{\sqrt{z_o^2}\cdot\omega}{2\cdot c}\right]\cdot\cos\left[\frac{\sqrt{D^2+4\cdot z_o^2}\cdot\omega\omega}{2\cdot c}\right]\cdot\tan\left[\frac{t\cdot\omega}{2\cdot\pi}\right]+}{\cos\left[\frac{\sqrt{D^2+4\cdot z_o^2}\cdot\omega}{2\cdot c}\right]\cdot\sin\left[\frac{\sqrt{z_o^2}\cdot\omega}{2\cdot c}\right]+\sin\left[\frac{\sqrt{D^2+4\cdot z_o^2}\cdot\omega}{2\cdot c}\right]\cdot\cos\left[\frac{\sqrt{z_o^2}\cdot\omega}{2\cdot c}\right]}\ldots \tag{A.18}$$

$$\frac{\cos\left[\frac{\sqrt{z_o^2}\cdot\omega}{2\cdot c}\right]\cdot\sin\left[\frac{\sqrt{D^2+4\cdot z_o^2}\cdot\omega}{2\cdot c}\right]\cdot\tan\left[\frac{t\cdot\omega}{2\cdot\pi}\right]}{} = 0 \tag{A.19}$$

Multiplying by the denominator gives

$$\cos\left[\frac{(-2\cdot c\cdot t+\pi(2\cdot z_o+\sqrt{D^2+4\cdot z_o^2}))\cdot\omega}{4\cdot c\cdot\pi}\right]\cdot\sec\left[\frac{\sqrt{D^2+4\cdot z_o^2}\cdot\omega}{2\cdot\pi}\right] = 0 \tag{A.20}$$

If

$$\sec\left[\frac{\sqrt{D^2+4\cdot z_o^2}\cdot\omega}{2\cdot\pi}\right] \neq 0 \tag{A.21}$$

the only solution to this equation is

$$\cos\left[\frac{(-2\cdot c\cdot t+\pi(2\cdot z_o+\sqrt{D^2+4\cdot z_o^2}))\cdot\omega}{4\cdot c\cdot\pi}\right] = 0 \qquad \text{(A.22).}$$

This can be achieved by

$$\frac{(-2\cdot c\cdot t+\pi(2\cdot z_o+\sqrt{D^2+4\cdot z_o^2}))\cdot\omega}{4\cdot c\cdot\pi} = n\cdot\pi+\frac{\pi}{2} \tag{A.23}$$

with n being a whole number. With these assumptions and $n = 0$ an expression for t can be obtained

$$t = -\frac{2\cdot\pi\left(\frac{\pi}{2}-\frac{(2\sqrt{z_o^2}+\sqrt{D^2+4z_o^2})\cdot\omega}{4\cdot c}\right)}{\omega} \tag{A.24}$$

The expression for t can be inserted into Equation (2.16) to give Equation (2.17).

$$|p(z_o)| = \left| \cdot \rho \cdot c \cdot v_{max} \cdot \sin\left(\frac{\pi}{\lambda} \left[\sqrt{\left(\frac{D}{2}\right)^2 + z_o^2} - z_o \right] \right) \right| \tag{A.25}$$

A.3 Derivation of the pressure at an arbitrary position

The method of calculating the pressure at an arbitrary position is essentially the same as on the center line. From Equations (2.15) and (3.23) follows by using only the real part of Equation (2.15)

$$p(\vec{r}_s, \vec{r}_s, t) = -\frac{r_s\, v\, \rho\, \omega}{2\,\pi} \int\limits_0^R \int\limits_0^{2\pi} \frac{\sin\left(\frac{\omega}{2}\left(\frac{t}{\pi} - \frac{2\sqrt{r_o^2+r_s^2+z_o^2-2\,z_o\,z_s+z_s^2-2\,r_o\,r_s\,\cos(\varphi_o-\varphi_s)}}{c}\right)\right)}{\sqrt{r_o^2+r_s^2+z_o^2-2\,z_o\,z_s+z_s^2-2\,r_o\,r_s\,\cos(\varphi_o-\varphi_s)}}\, d\,\varphi_s\, d\,r_s \tag{A.26}$$

To eliminate the time dependency and to find the maximum pressure for a location the derivative with respect to t has to be calculated

$$\frac{d\,p(\vec{r}_s, \vec{r}_s, t)}{d\,t} = -\frac{r_s\, v\, \rho\, \omega^2}{4\,\pi^2} \int\limits_0^R \int\limits_0^{2\pi} \frac{\cos\left(\frac{\omega}{2}\left(\frac{t}{\pi} - \frac{2\sqrt{r_o^2+r_s^2+z_o^2-2\,z_o\,z_s+z_s^2-2\,r_o\,r_s\,\cos(\varphi_o-\varphi_s)}}{c}\right)\right)}{\sqrt{r_o^2+r_s^2+z_o^2-2\,z_o\,z_s+z_s^2-2\,r_o\,r_s\,\cos(\varphi_o-\varphi_s)}}\, d\,\varphi_s\, d\,r_s \tag{A.27}$$

and has to be zero, which is achieved by having the integral of the cosine zero which leads to

$$\int\limits_0^R \int\limits_0^{2\pi} \cos\left(\frac{\omega}{2}\left(\frac{t}{\pi} - \frac{2\sqrt{r_o^2+r_s^2+z_o^2-2\,z_o\,z_s+z_s^2-2\,r_o\,r_s\,\cos(\varphi_o-\varphi_s)}}{c}\right)\right) d\,\varphi_s\, d\,r_s = 0 \tag{A.28}$$

Using trigonometric functions the cosine of this equation can be separated into a time-dependent part and a position-dependent part.

$$\begin{aligned} &\cos\left(\frac{t\,\omega}{2\,\pi}\right) \cdot \cos\left(\frac{\omega\sqrt{r_o^2+r_s^2+z_o^2-2\,z_o\,z_s+z_s^2-2\,r_o\,r_s\,\cos(\varphi_o-\varphi_s)}}{c}\right) \\ &+\sin\left(\frac{t\,\omega}{2\,\pi}\right) \cdot \sin\left(\frac{\omega\sqrt{r_o^2+r_s^2+z_o^2-2\,z_o\,z_s+z_s^2-2\,r_o\,r_s\,\cos(\varphi_o-\varphi_s)}}{c}\right) \end{aligned} \tag{A.29}$$

and

$$\tan\left(\frac{t\,\omega}{2\,\pi}\right)=\frac{\int\limits_0^R\int\limits_0^{2\pi}\frac{\cos\left(\frac{\omega\,\sqrt{r_o^2+r_s^2+z_o^2-2\,z_o\,z_s+z_s^2-2\,r_o\,r_s\,\cos(\varphi_o-\varphi_s)}}{c}\right)}{\sqrt{r_o^2+r_s^2+z_o^2-2\,z_o\,z_s+z_s^2-2\,r_o\,r_s\,\cos(\varphi_o-\varphi_s)}}\,d\,\varphi_s\,d\,r_s}{\int\limits_0^R\int\limits_0^{2\pi}\frac{\sin\left(\frac{\omega\,\sqrt{r_o^2+r_s^2+z_o^2-2\,z_o\,z_s+z_s^2-2\,r_o\,r_s\,\cos(\varphi_o-\varphi_s)}}{c}\right)}{\sqrt{r_o^2+r_s^2+z_o^2-2\,z_o\,z_s+z_s^2-2\,r_o\,r_s\,\cos(\varphi_o-\varphi_s)}}\,d\,\varphi_s\,d\,r_s} \tag{A.30}$$

Applying the inverse tangent this gives Equation (A.31):

$$t_{max}=-\frac{2\,\pi}{\omega}\cdot\arctan\left(\frac{\int\limits_0^{D/2}\int\limits_0^{2\pi}\frac{r_s\cos\left(\frac{\omega\cdot\sqrt{r_o^2+r_s^2+z_o^2-2\cdot z_o\cdot z_s+z_s^2-2\cdot r_o\cdot r_s\cdot\cos\left(\varphi_o-\varphi_s\right)}}{c}\right)}{\sqrt{r_o^2+r_s^2+z_o^2-2\cdot z_o\cdot z_s+z_s^2-2\cdot r_o\cdot r_s\cdot\cos\left(\varphi_o-\varphi_s\right)}}\,d\varphi_s\,dr_s}{\int\limits_0^{D/2}\int\limits_0^{2\pi}\frac{r_s\sin\left(\frac{\omega\cdot\sqrt{r_o^2+r_s^2+z_o^2-2\cdot z_o\cdot z_s+z_s^2-2\cdot r_o\cdot r_s\cdot\cos\left(\varphi_o-\varphi_s\right)}}{c}\right)}{\sqrt{r_o^2+r_s^2+z_o^2-2\cdot z_o\cdot z_s+z_s^2-2\cdot r_o\cdot r_s\cdot\cos\left(\varphi_o-\varphi_s\right)}}\,d\varphi_s\,dr_s}\right) \quad \text{(A.31).}$$

A.4 Limit of the Bosanquet-Equation

In this section the limit of Equation (2.111) for $t \to 0$ is derived. Equation (2.111) is:

$$\dot{h}(t)=\frac{A-A\cdot e^{-\frac{t}{B}}}{\sqrt{2}\sqrt{-A\cdot B+A\cdot B\cdot e^{-\frac{t}{B}}+A\cdot t}} \quad \text{(A.32).}$$

For $t \to 0$ both nominator and denominator are zero. An approximation for the natural exponential function e^x is obtained by a Taylor-Series expansion, stopping after the 2nd order term:

$$e^x=\sum_{i=0}^{\infty}\left(\frac{x^i}{i!}\right)\approx 1+x+\frac{x^2}{2} \quad \text{(A.33).}$$

This is inserted into Equation (2.111) to give

$$\begin{aligned}
\dot{h}(t) &\approx \sqrt{\frac{A}{2\cdot B}}\cdot\frac{\frac{t}{B}-\frac{t^2}{2\cdot B}}{\sqrt{\frac{t^2}{2\cdot B^2}-\frac{t}{B}+\frac{t}{B}}} && \text{(A.34)}\\
&= \sqrt{\frac{A}{2\cdot B}}\cdot\sqrt{2}\left(1-\frac{t}{2\cdot B}\right) && \text{(A.35)}\\
&= \sqrt{\frac{A}{B}} && \text{(A.36)}
\end{aligned}$$

A.5 Integration Boundaries

In this section of the appendix the integration boundaries are given for the evaluation of the integration of Equation (3.26) which is only valid for $t > 0$ and $d < c \cdot t$. The integration boundaries take this condition into account.

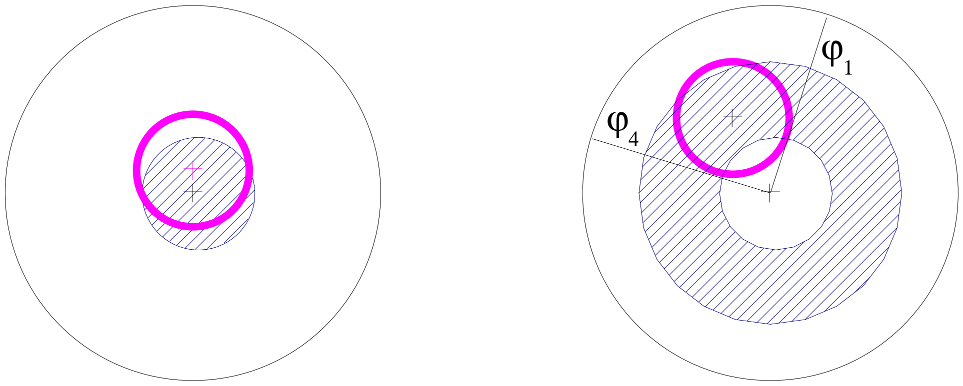

(a)
$$\int_0^{2\pi}\int_0^{c}\int_0^{2\pi}\int_{r_1}^{r_2} f(r_s,\varphi_s,r_o,\varphi_o)\,dr_s\,d\varphi_s\,dr_o\,d\varphi_o$$

(b)
$$\int_0^{2\pi}\int_c^{R r_c}\int_{\varphi_1}^{\varphi_4}\int_{r_1}^{r_2} f(r_s,\varphi_s,r_o,\varphi_o)\,dr_s\,d\varphi_s\,dr_o\,d\varphi_o$$

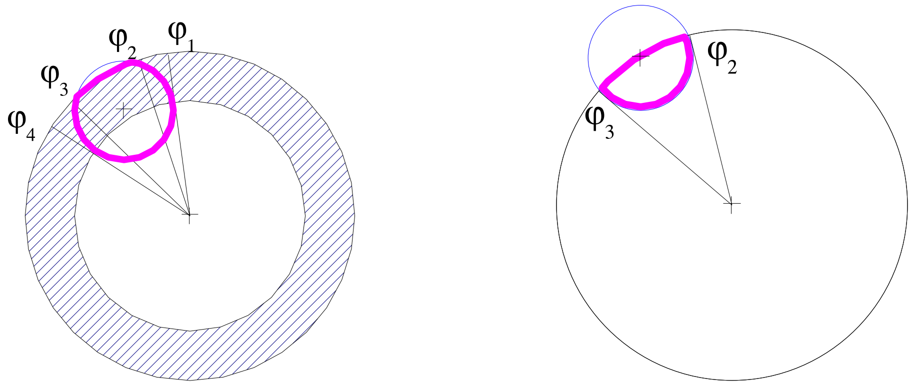

(c)
$$\int_0^{2\pi}\int_{R-r_c}^{R}\int_{\varphi_1}^{\varphi_2}\int_{r_1}^{r_2} f(r_s,\varphi_s,r_o,\varphi_o)\,dr_s\,d\varphi_s\,dr_o\,d\varphi_o$$
$$\int_0^{2\pi}\int_{R-r_c}^{R}\int_{\varphi_2}^{\varphi_3}\int_{r_1}^{R} f(r_s,\varphi_s,r_o,\varphi_o)\,dr_s\,d\varphi_s\,dr_o\,d\varphi_o$$
$$\int_0^{2\pi}\int_{R-r_c}^{R}\int_{\varphi_3}^{\varphi_4}\int_{r_1}^{r_2} f(r_s,\varphi_s,r_o,\varphi_o)\,dr_s\,d\varphi_s\,dr_o\,d\varphi_o$$

(d) This is a special case of (c)

Figure A.1: $0 < r_c < R/2$
Sketch of the boundaries of integration in magenta. The hatched area is a function of time and shows the region for the center point of an observer for whom the integration boundaries are valid. The radius of the transducer is R, $r_c = \sqrt{c \cdot t - (z_o - z_s)^2}$ is a function of the time t, speed of sound in the medium c, the distance $(z_o - z_s)$, and describes the radius of an area which can interfere at the point of observation.
$r_1 = r_o \cos(\varphi_s - \varphi_o) - \sqrt{r_c^2 - r_o^2 + r_o^2 \cos^2(\varphi_s - \varphi_o)}$
$r_2 = r_o \cos(\varphi_s - \varphi_o) + \sqrt{r_c^2 - r_o^2 + r_o^2 \cos^2(\varphi_s - \varphi_o)}$
$\varphi_1 = \varphi_o - \arccos(\sqrt{r_o^2 - r_c^2}/r_o)$
$\varphi_2 = \varphi_o - \arccos(\sqrt{R^2 + r_o^2 - r_c^2}/(2\,R\,r_o))$
$\varphi_3 = \varphi_o + \arccos(\sqrt{R^2 + r_o^2 - r_c^2}/(2\,R\,r_o))$
$\varphi_4 = \varphi_o + \arccos(\sqrt{r_o^2 - r_c^2}/r_o)$

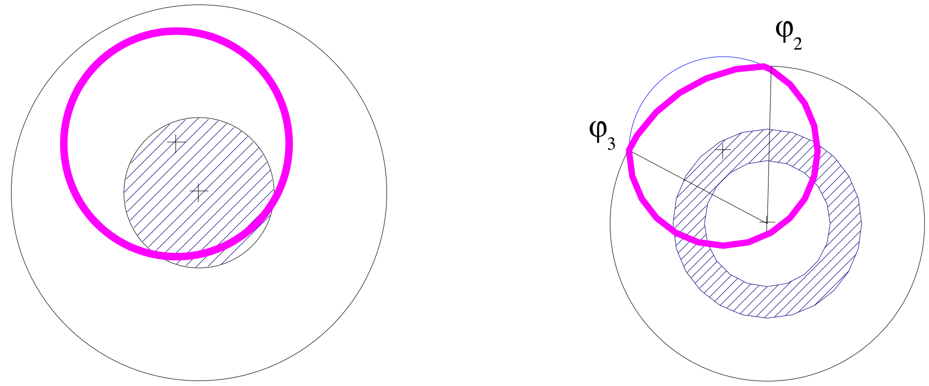

(a)
$$\int_0^{2\pi}\int_0^{R-r_c}\int_0^{2\pi}\int_{r_1}^{r_2} f(r_s,\varphi_s,r_o,\varphi_o)\,dr_s\,d\varphi_s\,dr_o\,d\varphi_o$$

(b)
$$\int_0^{2\pi}\int_{R-r_c}^{r_c}\int_0^{\varphi_2}\int_{r_1}^{r_2} f(r_s,\varphi_s,r_o,\varphi_o)\,dr_s\,d\varphi_s\,dr_o\,d\varphi_o$$
$$\int_0^{2\pi}\int_{R-r_c}^{r_c}\int_{\varphi_2}^{\varphi_3}\int_{r_1}^{R} f(r_s,\varphi_s,r_o,\varphi_o)\,dr_s\,d\varphi_s\,dr_o\,d\varphi_o$$
$$\int_0^{2\pi}\int_{R-r_c}^{r_c}\int_{\varphi_3}^{2\pi}\int_{r_1}^{r_2} f(r_s,\varphi_s,r_o,\varphi_o)\,dr_s\,d\varphi_s\,dr_o\,d\varphi_o$$

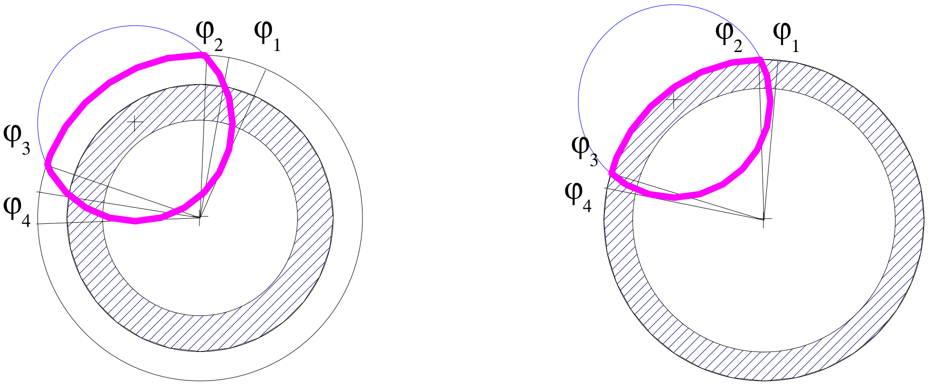

(c)
$$\int_0^{2\pi}\int_{r_c}^{R}\int_{\varphi_1}^{\varphi_2}\int_{r_1}^{r_2} f(r_s,\varphi_s,r_o,\varphi_o)\,dr_s\,d\varphi_s\,dr_o\,d\varphi_o$$
$$\int_0^{2\pi}\int_{r_c}^{R}\int_{\varphi_2}^{\varphi_3}\int_{r_1}^{R} f(r_s,\varphi_s,r_o,\varphi_o)\,dr_s\,d\varphi_s\,dr_o\,d\varphi_o$$
$$\int_0^{2\pi}\int_{r_c}^{R}\int_{\varphi_3}^{\varphi_4}\int_{r_1}^{r_2} f(r_s,\varphi_s,r_o,\varphi_o)\,dr_s\,d\varphi_s\,dr_o\,d\varphi_o$$

(d) Caption

Figure A.2: $R/2 < r_c < R$
Sketch of the boundaries of integration in magenta. The hatched area is a function of time and shows the region for the center point of an observer for whom the integration boundaries are valid. The radius of the transducer is R, $r_c = \sqrt{c \cdot t - (z_o - z_s)^2}$ is a function of the time t, speed of sound in the medium c, the distance $(z_o - z_s)$, and describes the radius of an area which can interfere at the point of observation.
$r_1 = r_o \cos(\varphi_s - \varphi_o) - \sqrt{r_c^2 - r_o^2 + r_o^2 \cos^2(\varphi_s - \varphi_o)}$
$r_2 = r_o \cos(\varphi_s - \varphi_o) + \sqrt{r_c^2 - r_o^2 + r_o^2 \cos^2(\varphi_s - \varphi_o)}$
$\varphi_1 = \varphi_o - \arccos(\sqrt{r_o^2 - r_c^2}/r_o)$
$\varphi_2 = \varphi_o - \arccos(\sqrt{R^2 + r_o^2 - r_c^2}/(2\,R\,r_o))$
$\varphi_3 = \varphi_o + \arccos(\sqrt{R^2 + r_o^2 - r_c^2}/(2\,R\,r_o))$
$\varphi_4 = \varphi_o + \arccos(\sqrt{r_o^2 - r_c^2}/r_o)$

(a)
$$\int_0^{2\pi}\int_0^{c-R}\int_0^{2\pi}\int_0^{R} f(r_s,\varphi_s,r_o,\varphi_o)\,dr_s\,d\varphi_s\,dr_o\,d\varphi_o$$

(b)
$$\int_0^{2\pi}\int_{c-R}^{R}\int_{\varphi_1}^{\varphi_4}\int_{r_1}^{R} f(r_s,\varphi_s,r_o,\varphi_o)\,dr_s\,d\varphi_s\,dr_o\,d\varphi_o$$

Figure A.3: $R < r_c < 2R$
Sketch of the boundaries of integration in magenta. The hatched area is a function of time and shows the region for the center point of an observer for whom the integration boundaries are valid. The radius of the transducer is R, $r_c = \sqrt{c \cdot t - (z_o - z_s)^2}$ is a function of the time t, speed of sound in the medium c, the distance $(z_o - z_s)$, and describes the radius of an area which can interfere at the point of observation.
$r_1 = r_o \cos(\varphi_s - \varphi_o) - \sqrt{r_c^2 - r_o^2 + r_o^2 \cos^2(\varphi_s - \varphi_o)}$
$r_2 = r_o \cos(\varphi_s - \varphi_o) + \sqrt{r_c^2 - r_o^2 + r_o^2 \cos^2(\varphi_s - \varphi_o)}$
$\varphi_1 = \varphi_o - \arccos(\sqrt{r_o^2 - r_c^2}/r_o)$
$\varphi_2 = \varphi_o - \arccos(\sqrt{R^2 + r_o^2 - r_c^2}/(2\,R\,r_o))$
$\varphi_3 = \varphi_o + \arccos(\sqrt{R^2 + r_o^2 - r_c^2}/(2\,R\,r_o))$
$\varphi_4 = \varphi_o + \arccos(\sqrt{r_o^2 - r_c^2}/r_o)$

A.6 Validation of the numeric calculation with the example of the pressure on the centre line

At large enough distances interference is not an issue as the Sender behaves like a point source. The calculation of the acoustic field according to Equation (3.26) can be simplified by using

$$p(d) = \frac{i \cdot \omega \cdot \rho}{2 \cdot \pi} \cdot R^{\frac{\omega \cdot t}{2 \cdot \pi}} \cdot e^{\frac{i \cdot \omega \cdot t}{2 \cdot \pi}} \cdot \int_s \frac{R^{-\frac{\omega \cdot d}{2\pi \cdot c}}}{d} \, ds \tag{A.37}$$

This removes an oscillating integrand from the equation, speeding up the time for the calculation significantly.

The calculation of the sound-pressure on the centre line perpendicular to the surface is used to verify the numeric calculations. Equation (2.15) has been evaluated numerically and plotted, as well as its analytical solution given in Equation (2.17) . The results are plotted in Figure A.4

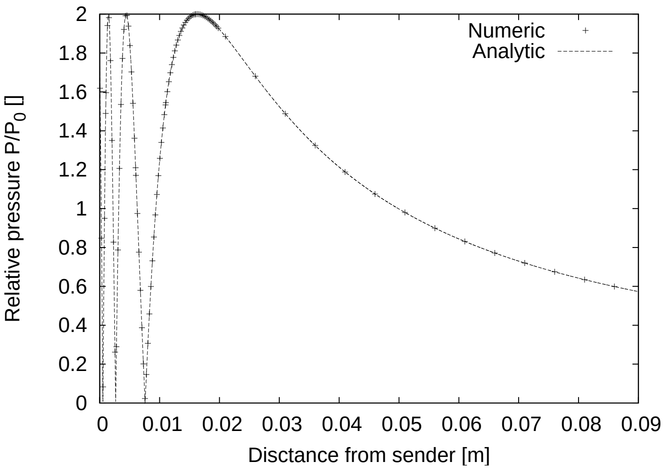

Figure A.4: Comparison of the evaluation of the pressure on the centre line using an analytic and a numeric method. The two solutions are almost identical. The numeric calculations can be used to approximate the analytic solution. The values for the calculation of this graph are the Sender diameter $D = 0.01$ m, the density $\rho = 1000$ kg/m^3 of the medium through which the sound propagates, the frequency of ultrasound $f = 1$ MHz and the speed of sound $c = 1500$ m/s in the medium.

A.7 Transmission coefficient of a plate subject to different media on each side

In this section the transmission coefficient for plate which separates two liquids is derived. The two liquids may have different physical properties. The ultrasonic wave is generated somewhere in medium 1 and propagates towards the surface of the plate. The angle between the direction of propagation and the perpendicular of the surface of the plate is θ_1. The liquid has the density ρ_1. The speed of sound within medium 1 is c_1. The ultrasonic wave has an angular frequency ω and a wave number k_1. The part of the wave number in the direction of the perpendicular of the surface of the plate is $k_{1,x} = k_1 \cdot \cos(\theta_1)$. A part of the wave ϕ_1 is reflected and is called ϕ_1'. The transmitted part is ϕ_2. Any shear waves generated at the interface are neglected. The wave ϕ_2 has an angle θ_2 with the perpendicular of the surface of the plate. The density of the plate is ρ_2 and the speed of sound in the plate is c_2. The wave number of ϕ_2 is k_2 and again the part in the direction of the perpendicular of the surface of the plate is $k_{2,x} = k_2 \cdot \cos(\theta_2)$. At the second surface the wave ϕ_2 is partly reflected and partly transmitted. The reflected part is called ϕ_2'. The transmitted part is called ϕ_3. The transmitted wave forms an angle θ_3 with the perpendicular of the surface of the plate. Its wave number is k_3 and the part of the wave number in the direction of the perpendicular of the surface of the plate is $k_{3,x} = k_3 \cdot \cos(\theta_3)$. The aim is to determine the Reflection coefficient of the plate:

$$R_{\text{Plate}} = \text{Real}\left(\frac{\phi_1'(0)}{\phi_1(0)}\right) \tag{A.38}$$

A Sketch of the situation at the plate is shown in Figure A.5.

The wave equations in cartesian coordinates (x, y) are

$$\begin{aligned}
\phi_1 &= \phi_{1,\,\max} \cdot \exp\{\imath[\omega \cdot t - k_1 \cdot (x \cdot \cos(\theta_1) + y \cdot \sin(\theta_1))]\} && \text{(A.39)}\\
\phi_1' &= \phi_{1,\,\max}' \cdot \exp\{\imath[\omega \cdot t + k_1 \cdot (x \cdot \cos(\theta_1) - y \cdot \sin(\theta_1))]\} && \text{(A.40)}\\
\phi_2 &= \phi_{2,\,\max} \cdot \exp\{\imath[\omega \cdot t - k_2 \cdot (x \cdot \cos(\theta_1) + y \cdot \sin(\theta_2))]\} && \text{(A.41)}\\
\phi_2' &= \phi_{2,\,\max}' \cdot \exp\{\imath[\omega \cdot t + k_2 \cdot (x \cdot \cos(\theta_1) - y \cdot \sin(\theta_2))]\} && \text{(A.42)}\\
\phi_3 &= \phi_{3,\,\max} \cdot \exp\{\imath[\omega \cdot t - k_3 \cdot (x \cdot \cos(\theta_3) + y \cdot \sin(\theta_3))]\} && \text{(A.43)}
\end{aligned}$$

In order to calculate the transmission coefficient of the plate a pressure and velocity balance at the two surfaces is evaluated. For this evaluation cartesian coordinates are chosen. The variable x is in the direction of the perpendicular of the surface of the plate. The pressure balance and velocity balance are formulated for the x-component of the forces only. The balance

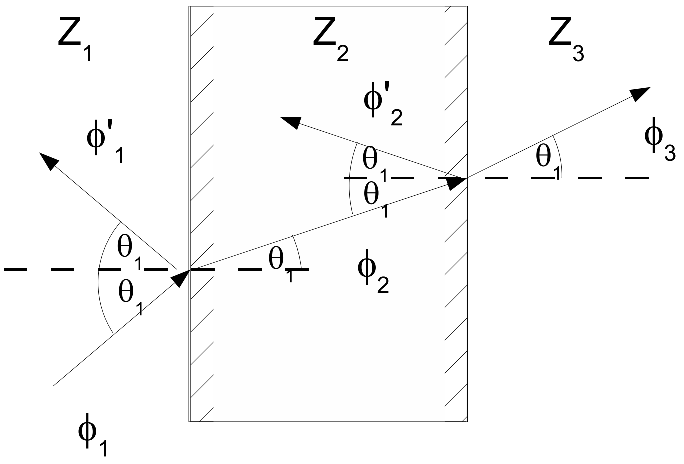

Figure A.5: Sketch of a plate with an incoming wave ϕ_1 which is reflected to ϕ_1' and transmitted to ϕ_2. The transmitted wave is reflected to ϕ_2' and transmitted to ϕ_3. The plate has a thickness of d and an acoustic impedance of Z_2. One side of the plate is in contact with a liquid 1 with the acoustic impedance Z_1 the other side is in contact with a liquid 2 with the acoustic impedance Z_3.

for $x = 0$ is then

$$\rho_1 \cdot (\phi_1 + \phi_1') = \rho_2 \cdot (\phi_2 + \phi_2') \tag{A.44}$$

$$k_{1,x} \cdot (\phi_1 - \phi_1') = k_{2,x} \cdot (\phi_2 - \phi_2') \tag{A.45}$$

and for $x = d$ is

$$\rho_2 \cdot (\phi_2 + \phi_2') = \rho_3 \cdot \phi_3 \tag{A.46}$$

$$k_{2,x} \cdot (\phi_2 - \phi_2') = k_{3,x} \cdot \phi_3 \tag{A.47}$$

Rewriting Equations (A.39), (A.40), (A.41), (A.42) and (A.43) for $x = 0$ gives

$$\phi_1(0) = \phi_{1,\,\mathrm{max}} \cdot \exp\{\imath[\omega \cdot t - k_1 \cdot (y \cdot \sin(\theta_1)]\} \tag{A.48}$$

$$\phi_1'(0) = \phi_{1,\,\mathrm{max}}' \cdot \exp\{\imath[\omega \cdot t - k_1 \cdot (y \cdot \sin(\theta_1)]\} \tag{A.49}$$

$$\phi_2(0) = \phi_{2,\,\mathrm{max}} \cdot \exp\{\imath[\omega \cdot t - k_2 \cdot (y \cdot \sin(\theta_2)]\} \tag{A.50}$$

$$\phi_2'(0) = \phi_{2,\,\mathrm{max}}' \cdot \exp\{\imath[\omega \cdot t - k_2 \cdot (y \cdot \sin(\theta_2)]\} \tag{A.51}$$

Inserting Equations (A.48), (A.49), (A.50) and (A.51) into Equations (A.44) and (A.45) gives

$$\begin{aligned} \rho_1 \cdot (\phi_{1,\,\mathrm{max}} + \phi_{1,\,\mathrm{max}}') \cdot \exp\{\imath[\omega \cdot t - k_1 \cdot (y \cdot \sin(\theta_1)]\} &= \\ \rho_2 \cdot (\phi_{2,\,\mathrm{max}} + \phi_{2,\,\mathrm{max}}') \cdot \exp\{\imath[\omega \cdot t - k_2 \cdot (y \cdot \sin(\theta_2)]\}, & \end{aligned} \tag{A.52}$$

$$\begin{aligned} k_{1,x} \cdot (\phi_{1,\,\mathrm{max}} + \phi_{1,\,\mathrm{max}}') \cdot \exp\{\imath[\omega \cdot t - k_1 \cdot (y \cdot \sin(\theta_1)]\} &= \\ k_{2,x} \cdot (\phi_{2,\,\mathrm{max}} + \phi_{2,\,\mathrm{max}}') \cdot \exp\{\imath[\omega \cdot t - k_2 \cdot (y \cdot \sin(\theta_2)]\} & \end{aligned} \quad (\mathrm{A.53}).$$

The wave equations at the second interface at $x = d$ are:

$$\begin{aligned} \phi_2(d) &= \phi_{2,\,\max} \cdot \exp\{\imath[\omega \cdot t - k_2 \cdot (d \cdot \cos(\theta_2) + y \cdot \sin(\theta_2)]\}, && \text{(A.54)} \\ \phi_2'(d) &= \phi_{2,\,\max}' \cdot \exp\{\imath[\omega \cdot t + k_2 \cdot (d \cdot \cos(\theta_2) - y \cdot \sin(\theta_2)]\}, && \text{(A.55)} \\ \phi_3(d) &= \phi_{3,\,\max} \cdot \exp\{\imath[\omega \cdot t - k_3 \cdot (d \cdot \cos(\theta_3) + y \cdot \sin(\theta_3)]\} && \text{(A.56).} \end{aligned}$$

Equations (A.54) and (A.55) can be simplified:

$$\begin{aligned} \phi_2(d) &= \phi_2(0) \cdot \exp\{-k_2 \cdot d \cdot \cos(\theta_2)\}, && \text{(A.57)} \\ \phi_2'(d) &= \phi_2'(0) \cdot \exp\{k_2 \cdot d \cdot \cos(\theta_2)\} && \text{(A.58).} \end{aligned}$$

Equations (A.54), (A.55) and (A.56) are then:

$$\begin{aligned} \rho_2 \cdot (\phi_2(d) + \phi_2'(d)) &= \rho_3 \cdot \phi_3(d), && \text{(A.59)} \\ k_{2,x} \cdot (\phi_2(d) - \phi_2'(d)) &= k_{3,x} \cdot \phi_3(d) && \text{(A.60).} \end{aligned}$$

Adding Equation (A.59) to Equation (A.60) gives an expression for ϕ_2:

$$\phi_2(d) = \frac{1}{2} \cdot \left(\frac{\rho_3}{\rho_2} + \frac{k_{x,3}}{k_{x,2}}\right) \cdot \phi_3(d) \qquad \text{(A.61).}$$

Subtracting Equation (A.59) from Equation (A.60) gives an expression for ϕ_2':

$$\phi_2'(d) = \frac{1}{2} \cdot \left(\frac{\rho_3}{\rho_2} - \frac{k_{x,3}}{k_{x,2}}\right) \cdot \phi_3(d) \qquad \text{(A.62).}$$

Performing the same steps for Equations (A.52) and (A.53) gives:

$$\begin{aligned} 2 \cdot \phi_1(0) &= \frac{\rho_2}{\rho_1} \cdot (\phi_2(0) + \phi'(0)) + \frac{k_{x,2}}{k_{x,1}} \cdot (\phi_2(0) + \phi'(0)) && \text{(A.63)} \\ 2 \cdot \phi_1'(0) &= \frac{\rho_2}{\rho_1} \cdot (\phi_2(0) + \phi'(0)) - \frac{k_{x,2}}{k_{x,1}} \cdot (\phi_2(0) + \phi'(0)) && \text{(A.64)} \end{aligned}$$

Inserting Equations (A.61) and (A.62) into Equations (A.63) and (A.64) gives:

$$\begin{aligned} 2 \cdot \phi_1(0) &= \frac{\rho_2}{\rho_1} \cdot \left(\frac{\frac{1}{2} \cdot \left(\frac{\rho_3}{\rho_2} + \frac{k_{x,3}}{k_{x,2}}\right) \cdot \phi_3(d)}{\exp\{-\imath \cdot k_2 \cdot d \cdot \cos(\theta_2)\}} + \frac{\frac{1}{2} \cdot \left(\frac{\rho_3}{\rho_2} - \frac{k_{x,3}}{k_{x,2}}\right) \cdot \phi_3(d)}{\exp\{\imath k_2 \cdot d \cdot \cos(\theta_2)\}} \right) + \\ & \quad \frac{k_{x,2}}{k_{x,1}} \cdot \left(\frac{\frac{1}{2} \cdot \left(\frac{\rho_3}{\rho_2} + \frac{k_{x,3}}{k_{x,2}}\right) \cdot \phi_3(d)}{\exp\{-\imath \cdot k_2 \cdot d \cdot \cos(\theta_2)\}} - \frac{\frac{1}{2} \cdot \left(\frac{\rho_3}{\rho_2} - \frac{k_{x,3}}{k_{x,2}}\right) \cdot \phi_3(d)}{\exp\{\imath \cdot k_2 \cdot d \cdot \cos(\theta_2)\}} \right) \\ & && \text{(A.65)} \end{aligned}$$

and

$$\begin{aligned} 2 \cdot \phi_1'(0) &= \frac{\rho_2}{\rho_1} \cdot \left(\frac{\frac{1}{2} \cdot \left(\frac{\rho_3}{\rho_2} + \frac{k_{x,3}}{k_{x,2}}\right) \cdot \phi_3(d)}{\exp\{-\imath \cdot k_2 \cdot d \cdot \cos(\theta_2)\}} + \frac{\frac{1}{2} \cdot \left(\frac{\rho_3}{\rho_2} - \frac{k_{x,3}}{k_{x,2}}\right) \cdot \phi_3(d)}{\exp\{\imath k_2 \cdot d \cdot \cos(\theta_2)\}} \right) - \\ & \quad \frac{k_{x,2}}{k_{x,1}} \cdot \left(\frac{\frac{1}{2} \cdot \left(\frac{\rho_3}{\rho_2} + \frac{k_{x,3}}{k_{x,2}}\right) \cdot \phi_3(d)}{\exp\{-\imath \cdot k_2 \cdot d \cdot \cos(\theta_2)\}} - \frac{\frac{1}{2} \cdot \left(\frac{\rho_3}{\rho_2} - \frac{k_{x,3}}{k_{x,2}}\right) \cdot \phi_3(d)}{\exp\{\imath \cdot k_2 \cdot d \cdot \cos(\theta_2)\}} \right) \\ & && \text{(A.66)} \end{aligned}$$

The reflection $R_{\text{Plate}} = \frac{\phi_1'(0)}{\phi_1(0)}$ coefficient is then:

$$R_{\text{Plate}} = \text{Real}\left(\frac{\exp\left\{2 \cdot \imath \cdot k_2 \cdot d \cdot \cos\left(\theta_2\right)\right\} \cdot A + B}{\exp\left\{2 \cdot \imath \cdot k_2 \cdot d \cdot \cos\left(\theta_2\right)\right\} \cdot C + D}\right) \tag{A.67}$$

with

$$\begin{aligned}
A &= \left(\frac{\rho_3}{\rho_2} + \frac{k_{3,x}}{k_{2,x}}\right) \cdot \left(\frac{\rho_2}{\rho_1} - \frac{k_{2,x}}{k_{1,x}}\right), && \text{(A.68)} \\
B &= \left(\frac{\rho_3}{\rho_2} - \frac{k_{3,x}}{k_{2,x}}\right) \cdot \left(\frac{\rho_2}{\rho_1} + \frac{k_{2,x}}{k_{1,x}}\right), && \text{(A.69)} \\
C &= \left(\frac{\rho_3}{\rho_2} + \frac{k_{3,x}}{k_{2,x}}\right) \cdot \left(\frac{\rho_2}{\rho_1} + \frac{k_{2,x}}{k_{1,x}}\right), && \text{(A.70)} \\
D &= \left(\frac{\rho_3}{\rho_2} - \frac{k_{3,x}}{k_{2,x}}\right) \cdot \left(\frac{\rho_2}{\rho_1} - \frac{k_{3,x}}{k_{1,x}}\right) && \text{(A.71).}
\end{aligned}$$